INVESTIGATIONS OF MISSISSIPPI VALLEY-TYPE MINERALIZING FLUIDS VIA ANALYTICAL GEOCHEMISTRY, NUMERICAL MODELING, AND EXPERIMENTAL GEOCHEMISTRY

A Dissertation

presented to

the Faculty of the Graduate School

at the University of Missouri-Columbia

In Partial Fulfillment

of the Requirements for the Degree

Doctor of Philosophy

by

SARAH ELISABETH SMITH

Dr. Martin Appold, Dissertation Supervisor

MAY 2021

The undersigned, appointed by the dean of the Graduate School, have examined the dissertation entitled

INVESTIGATIONS OF SEDIMENT-HOSTED BASE METAL DEPOSIT MINERALIZING FLUIDS VIA ANALYTICAL GEOCHEMISTRY, NUMERICAL MODELING, AND EXPERIMENTAL GEOCHEMIRSTRY

presented by Sarah Smith,

a candidate for the degree of doctor of philosophy,

and hereby certify that, in their opinion, it is worthy of acceptance.

_____

Professor Martin Appold

_____

Professor Hector Lamadrid

_____

Professor James Schiffbauer

_____

Professor Wesley Bernskoetter

Dedication

This dissertation is dedicated to my family. I would like to thank my incredibly tolerant and supportive husband as well as my slightly less tolerant, long-suffering children. Without their patience, tolerance, and moral support I would not have been able to complete this degree.

Acknowledgements

Table of Contents

List of Figures

List of Tables

Abstract

Mississippi Valley-type (MVT) deposits represent enrichments of base metals and other elements up to 1000's of times greater than their average concentrations in the Earth's crust. These enrichments most commonly consist of Zn and Pb as the minerals sphalerite and galena, but Ba and F, as the minerals barite and fluorite, can be abundant and even predominate over Zn and Pb in some deposits. Key to understanding how MVT deposits become enriched in the above elements is knowledge of the concentrations of these elements in the mineralizing fluids and how the fluids interact with host rocks. This dissertation consists of three studies that address this knowledge gap.

The first was a case study of the Hansonburg, New Mexico MVT district, in which barite and fluorite are the principal ore minerals. The aim of the study was to test the hypothesis that anomalously F-rich fluids formed fluorite-rich MVT deposits by analyzing the composition of fluid inclusions in ore stage minerals. The study showed that the Hansonburg mineralizing fluids were very F-rich, with F concentrations of 100's to 1000's of ppm. The fluids would have been very acidic, which would have suppressed metal sulfide mineral precipitation.

The second was a numerical reactive transport modeling study of the Illinois-Kentucky district, a fluorite dominant atypical MVT district. The aim of the study was to assess the importance of F-rich ore fluids in producing the features of the deposits observed in the field. These models showed that silica-armoring of conduits along which the F-rich fluids ascended was critical for allowing the fluids to retain their F-rich, acidic profile until the fluids entered the limestone host rocks. Further, the models showed that high ore fluid F concentrations of 100's to 1000's of ppm were necessary to form the

spatial distributions of fluorite mineralization and limestone host rock dissolution observed in the field, and to form the fluorite mineralization within a geologically reasonable time period.

The final experimental geochemistry study was undertaken with the goal of producing a tool for determining aqueous Zn concentrations from solid solution Zn concentrations in dolomite using element partitioning theory. Dolomite easily incorporates Zn into its crystal lattice and is a common ore-stage mineral in MVT deposits, thus it has a high potential for this purpose. However, experimental distribution coefficients (D) for the partitioning of Zn between dolomite and aqueous solution are unknown. A series of dolomite precipitation experiments was performed at temperatures between 125 and 200° C, 10 MPa pressure, and aqueous Zn concentrations from about 10 to 1000 ppm for periods of time ranging from 10 to 80 days. The D values calculated from these experiments have applications in hydrothermal ore formation, sedimentary diagenesis, and low-grade metamorphism.

Chapter 1: Introduction

Mississippi Valley-type (MVT) deposits are epigenetic, carbonate-hosted base metal deposits that typically have mineral assemblages consisting of sphalerite + galena + iron sulfide minerals + carbonate minerals ± barite ± fluorite (Misra, 2000; Leach et al., 2005, 2010; Paradis et al., 2007). Typical MVT mineral deposits are sulfide mineral dominant with either sphalerite or galena as the primary ore mineral and collectively account for as much as 20% of the world's Zn and Pb resources (Kesler and Simon, 2015).   In contrast, atypical MVT deposits may be fluorite or barite dominant, and can serve as important sources of these commodities. Over a century of extensive research has been performed on MVT deposits with the goal of ascertaining how these deposits formed. Major progress has been made in characterizing mineral assemblages and paragenetic sequences, identifying geologic features that localized mineralization, determining the flow rates, pathways, and driving mechanisms of mineralizing fluids, the ages of deposits, the source of metals, the temperature and composition of mineralizing fluids, and the tectonic context of deposit formation. Despite this progress, fundamental questions about the formation of both typical and atypical MVT deposits remain. Of particular importance are uncertainties about the concentrations of most of the principal ore constituents (Zn, Pb, Cu, Fe, F, and S) in MVT fluids, as well as pH and redox potential.

Many previous studies have attempted to characterize MVT fluids (e.g. Hall and Friedman, 1963; Roedder, 1968; Roedder, 1977; Richardson and Pinckney, 1984; Gratz and Misra, 1987; Haynes and Kesler, 1987; Crocetti and Holland, 1989; Sangster, 1996; Viets et al., 1996; Heijlen et al., 2003; Stoffell et al., 2008; Appold and Wenz, 2011;

Wenz et al., 2012; Pelch et al., 2015; Field et al., 2020). These studies collectively show that fluid inclusions in MVT deposits typically have homogenization temperatures in the range of 75 to 175° C and salinities in the range of 10 to 30 weight percent NaCl equivalent (Basuki and Spooner, 2004), dominated by Na, Ca, K, Mg, and Cl. These properties of MVT fluids closely resemble those of sedimentary brines circulating through the Earth's crust today, leading to the inference that MVT fluids are likely ancient sedimentary brines.

Little attention has been given so far to determining the F content of MVT fluids, despite the fundamental importance of F concentration in the fluids to the formation of atypical, fluorite rich MVT districts such as Hansonburg, New Mexico and Illinois-Kentucky. Previous researchers have hypothesized that fluorite-rich MVT deposits formed from anomalously F-rich fluids (e.g. Hall and Friedman, 1963; Heyl et al., 1966; Richardson et al., 1988; Plumlee et al., 1995), but this has so far only been established in the Illinois-Kentucky district, where F concentrations in the mineralizing fluids likely reached several thousand ppm (Kenderes and Appold, 2017). However, whether fluorite abundance in MVT deposits generally correlates with F concentrations in mineralizing fluids cannot be known until F concentration in MVT fluids from more deposits are determined.

An implication of the high ore fluid F concentrations found by Kenderes and Appold (2017) for the Illinois-Kentucky district is that the ore fluid must have had spectacularly low pH in the range of 0 to 1.4, much lower than the range of 4 to 5.5 considered typical of MVT fluids (Sverjensky, 1986). These low pH values raise several important questions about the origin of the Illinois-Kentucky deposits, including:

2

1. How an acidic F-rich fluid can have ascended from a magmatic source at depth through faults that transected multiple limestone layers without the fluid losing its acidity and high F concentrations.

2. How far an acidic, F-rich fluid could have traveled laterally through limestone upon exiting the faults before becoming neutralized.

3. How much limestone would have been dissolved by an acidic F-rich fluid.

4. The relative abundances of minerals that an acidic, F-rich fluid would precipitate, including their spatial distribution.

5. Whether a F-rich fluid is truly needed to form large fluorite ore deposits.

Finally, significant uncertainty remains regarding the metal content of MVT mineralizing fluids, particularly, whether the fluids were enriched in Zn and Pb relative to typical sedimentary brines, a hypothesized driver for the formation of large metal-rich MVT deposits (Wilkinson, et al. 2009; Pelch et al., 2015; Smith-Schmitz and Appold, 2018). Studies that have been undertaken to measure Zn and Pb concentrations directly in fluid inclusions hosted in MVT ore-stage minerals have produced equivocal results (Czamanske et al., 1963; Pinckney and Haffty, 1970; Appold et al., 2004; Wilkinson et al., 2005; Stoffell et al., 2008; Wilkinson et al., 2009; Appold and Wenz, 2011; Wenz et al., 2012; Hammerli et al., 2013; and Pelch et al., 2015), illustrating a need to find corroborating methods. Smith-Schmitz and Appold (2018) used element partitioning theory combined with Zn concentrations measured in ore-stage calcite from Central Tennessee and Illinois Kentucky and previously published mineralizing fluid calcium concentrations for the two districts to determine Zn concentrations of no more than 10's of ppm for the ore-stage mineralizing fluids. However, calcite is rarely ore-stage in MVT

districts, limiting its usefulness for determining Zn concentrations in ore fluids. In contrast, dolomite is commonly an ore-stage mineral in MVT deposits (e.g. Hagni and Grawe, 1964; Jolly and Heyl, 1964; McCormick et al., 1971; Sverjensky, 1981), and like calcite, dolomite readily incorporates Zn into its crystal lattice. Thus, dolomite is potentially a more useful tool for predicting the Zn concentration in mineralizing fluids. Currently, that potential is unrealized due to a lack of experimental distribution coefficients for the partitioning of Zn between dolomite and water.

This dissertation is focused on addressing the three areas of uncertainty discussed above. Chapter 2 reports the F concentrations measured in main-stage quartz-hosted fluid inclusions from the fluorite-rich Hansonburg, New Mexico district and in ore-stage quartz-hosted fluid inclusions from the Illinois-Kentucky district using SEM-EDS analysis. The F concentrations measured in this study are compared with the results from previous studies and implications of the F concentrations for hydrothermal mineralization in the Hansonburg district are considered. In chapter 3, numerical reactive transport modeling is used to evaluate the hypothesis that F-rich MVT deposits are formed from unusually F-rich, acidic fluids. In the models, which are based on the Illinois-Kentucky district, either an acidic, F-rich fluid based on the values reported by Kenderes and Appold (2017) or a "typical" MVT mineralizing fluid having a pH of 4 and F concentration based on typical sedimentary brine values is introduced at the base of a vertical silicified fault that cross cuts a limestone-rich sedimentary sequence containing resident sedimentary brines. The results of the reactive transport modeling address the questions enumerated above. In chapter 4, the results of a series of dolomite precipitation experiments performed at 125, 150, and 200° C and 10 MPa with fluids having Zn

concentrations of about 10, 100, and 1000 ppm are evaluated. Experimental distribution coefficients for the partitioning of Zn between dolomite and aqueous solution are calculated. The proximity of the experiments to equilibrium are evaluated and used to determine which experimental distribution coefficients represent equilibrium values.

1.1 References

Appold, M. S., Numelin, T. J., Shepherd, T. J., & Chenery, S. R., 2004. Limits on the metal content of fluid inclusions in gangue minerals from the Viburnum Trend, southeast Missouri, determined by laser ablation ICP-Ms. *Econ. Geol.*, **99**, 185-198.

Appold, M. S., 2021. Applications of fluid inclusions to studies of sediment-hosted base metal ore deposits: case studies from the central U.S.A. and Brazil. In *Mineral. Assoc. Can. Short Course*, **49**, 47–72.

Appold, M. S., & Wenz, Z. J., 2011. Composition of ore fluid inclusions from the Viburnum Trend, Southeast Missouri district, United States: Implications for transport and precipitation mechanisms. *Econ. Geol.*, **106**, 55-78.

Basuki, N. I., & Spooner, E. T. C., 2002. A review of fluid inclusion temperatures and salinities in Mississippi Valley-type Zn-Pb deposits: Identifying thresholds for metal transport. *Exploration and Mining Geology*, **11**, 1-17.

Czamanske, G. K., Roedder, E., & Burns, F. C., 1963. Neutron activation analysis of fluid inclusions for copper, manganese, and zinc. *Science*, **140**, 401-403.

Crocetti, C. A., & Holland, H. D., 1989. Sulfur-lead isotope systematics and the composition of fluid-inclusions in galena from the Viburnum Trend, Missouri. *Econ. Geol.*, **84**, 2196-2216.

Field, J.D., Appold, M.S., Coveney Jr., R.M., and Bodnar, R.J., 2020, Geochemical characteristics of trace occurrences of Mississippi Valley-type mineralization in the US mid-continent: Implications for deposit growth: *Journal of Geochemical Exploration*, v. 213,

Gratz, J. F., & Misra, K. C., 1987. Fluid inclusion study of the Gordonsville zinc deposit, central Tennessee. *Econ. Geol.*, **82**, 1790-1804.

Hall W. E. and Friedman I., 1963. Composition of fluid inclusions, Cave-in-Rock fluorite district, Illinois, and Upper Mississippi Valley zinc-lead district. *Econ. Geol.* **58**, 886–911

Hammerli, J., Rusk, B., Spandler, C., Emsbo, P., & Oliver, N. H., 2013. In situ quantification of Br and Cl in minerals and fluid inclusions by LA-ICP-MS: A powerful tool to identify fluid sources. *Chem. Geol.*, **337**, 75-87.

Haynes, F. M., & Kesler, S. E., 1987. Chemical evolution of brines during Mississippi Valley-type mineralization; evidence from East Tennessee and Pine Point. *Econ. Geol.*, **82**, 53-71.

Heijlen, W., Muchez, P., Banks, D. A., Schneider, J., Kucha, H., & Keppens, E., 2003. Carbonate-hosted Zn-Pb deposits in Upper Silesia, Poland: Origin and evolution

of mineralizing fluids and constraints on genetic models. *Econ. Geol.*, **98**, 911-932.

Heyl, A. V., Delevaux, M. H., Zartman, R. E., and Brock, M. R., 1966. Isotopic study of galenas from the upper Mississippi Valley, the Illinois-Kentucky, and some Appalachian Valley mineral districts. *Econ. Geol.* **61**, 933-961.

Kenderes, S. M., and Appold, M. S., 2017. Fluorine concentrations of ore fluids in the Illinois-Kentucky district: Evidence from SEM-EDS analysis of fluid inclusion decrepitates. *Geochim. Cosmochim. Acta*, **210**, 132-151.

Kesler, S.E., and Simon, A.C., 2015. *Mineral resources, economics and the environment*. Cambridge University Press.

Kesler, S. E., Martini, A. M., Appold, M. S., & Walter, L. M., 1996. Na-Cl-Br systematics of fluid inclusions from Mississippi Valley-type deposits, Appalachian Basin: Constraints on solute origin and migration paths. *Geochimica et Cosmochimica Acta*, **60**, 225-233.

Leach, D. L., Bradley, D. C., Huston, D., Pisarevsky, S. A., Taylor, R. D., & Gardoll, S. J., 2010). Sediment-hosted lead-zinc deposits in Earth history. *Econ. Geol.*, **105**, 593-625.

Misra, K.C., 2000. *Understanding Mineral Deposits*. Kluwer Academic Publishers, Dordrecht, Netherlands.

Paradis, S., Hannigan, P., and Dewing, K., 2007. Mississippi Valley-type lead-zinc deposits. Mineral deposits of Canada: A synthesis of major deposit-types, district metallogeny, the evolution of geological provinces, and exploration methods: *Geol. Assoc. Can. Spec. Pub.* **5**, 185-203.

Pelch, M. A., Appold, M. S., Emsbo, P., and Bodnar, R. J., 2015. Constraints from fluid inclusion compositions on the origin of Mississippi Valley-type mineralization in the Illinois-Kentucky district. *Econ. Geol.* **110**, 787-808.

Pinckney, D. M., & Haffty, J., 1970. Content of zinc and copper in some fluid inclusions from the Cave-in-Rock district, southern Illinois. *Econ. Geol.*, **65**, 451-458.

Plumlee G. S., Goldhaber M. B. and Rowan E. L., 1995. The potential role of magmatic gases in the genesis of Illinois-Kentucky fluorspar deposits; implications from chemical reaction path modeling. *Econ. Geol.* **90**, 999–1011.

Roedder, E., 1968. Temperature, salinity, and origin of the ore-forming fluids at Pine Point, Northwest Territories, Canada, from fluid inclusion studies. *Econ. Geol.*, **63**, 439-450.

Roedder, E., 1977. Fluid inclusion studies of ore deposits in the Viburnum Trend, southeast Missouri. *Econ. Geol.*, **72**, 474-479.

Richardson C. K. and Pinckney D. M., 1984. The chemical and thermal evolution of the fluids in the Cave-in-Rock fluorspar district, Illinois: Mineralogy, paragenesis, and fluid inclusions. *Econ. Geol.* **79**, 1833–1856.

Richardson, C. K., Rye, R. O., & Wasserman, M. D., 1988. The chemical and thermal evolution of the fluids in the Cave-in-Rock fluorspar district, Illinois; stable isotope systematics at the Deardorff Mine. *Econ. Geol.*, **83**, 765-783.

Sangster, D. F., 1996. Mississippi Valley-type lead-zinc. *Geology of Canadian Mineral Deposit Types. Edited by OR Eckstrand, WD Sinclair and RI Thorpe. Geological Survey of Canada*, **8**, 253-261.

Stoffell, B., Appold, M. S., Wilkinson, J. J., McClean, N. A., Jeffries, T. E., 2008. Geochemistry and evolution of Mississippi Valley-type mineralizing brines from the Tri-State and Northern Arkansas districts determined by LA-ICP-MS microanalysis of fluid inclusions. *Econ. Geol.*, **103**, 1411-1435.

Sverjensky, D.A., 1986. Genesis of Mississippi Valley-type lead-zinc deposits. *Ann. Rev. Earth & Planet. Sci.* **14**, 177–199.

Viets, J. G., Hofstra, A. H., and Emsbo, P., 1996. Solute compositions of fluid inclusions in sphalerite from North American and European Mississippi Valley-type ore deposits: Ore fluids derived from evaporated seawater. *Soc. Econ. Geol. Spec. Pub.*, **4**, 465-482.

Wenz, Z. J., Appold, M. S., Shelton, K. L., and Tesfaye, S., 2012. Geochemistry of Mississippi Valley–type mineralizing fluids of the Ozark Plateau: A regional synthesis. *Am. J. Sci.* **312**, 22-80.

Wilkinson, J. J., Stoffell, B., Wilkinson, C. C., Jeffries, T. E., & Appold, M. S., 2009. Anomalously metal-rich fluids form hydrothermal ore deposits. *Science*, **323**, 764-767.

Yardley, B.W., 2005. 100th Anniversary Special Paper: metal concentrations in crustal fluids and their relationship to ore formation. *Econ. Geol.* **100**, 613-632.

Chapter 2: Determination of fluorine concentrations in mineralizing fluids of the Hansonburg, New Mexico Ba-F-Pb district via SEM-EDS analysis of fluid inclusion decrepitates

2.1 Abstract

The Hansonburg, New Mexico district in the southwestern U.S.A. contains anomalously fluorite rich carbonate-hosted base metal sulfide deposits. A long-standing hypothesis for this fluorite enrichment is that the Hansonburg mineralizing fluids were correspondingly enriched in F relative to the typical sedimentary brines that formed carbonate-hosted base metal deposits.

The purpose of the present study was to test this hypothesis by determining the F concentration in fluid inclusions hosted by drusy quartz that paragenetically overlaps fluorite. The fluid inclusions were thermally decrepitated creating evaporative solute mounds, which were then analyzed via scanning electron microscope-energy dispersive X-ray spectroscopy (SEM-EDS). Fluorine was detected in all evaporative solute mounds analyzed, equating to fluid inclusion F concentrations of 320 to 2500 ppm. These F concentrations are significantly greater than the F concentrations of tenth's to 10s of ppm F typical of sedimentary brines. Further, these high F concentrations indicate that the Hansonburg mineralizing fluid must have been very acidic during the time of fluorite mineralization with a pH of 1 to 2.4. This pH is much lower than the pH of 4.3 to 5.1 predicted in earlier studies and also much lower than the pH of 4 to 5.5 considered typical of carbonate-hosted Zn-Pb mineralizing fluids. High mineralizing fluid F concentrations in combination with low pH would have provided conditions favorable for the formation

of the observed Hansonburg mineral assemblage, i.e. fluorite-barite rich and metal sulfide mineral poor.

2.2 Introduction

Carbonate-hosted Zn-Pb deposits are diverse in mineralogy, age, and geographic occurrence, but have in common their precipitation from sedimentary brines. Numerous previous studies have quantified the concentrations of the major elements, Na, Ca, Mg, K, and Cl, in these brines for many deposits around the world. However, less is known about the concentrations of important ore mineral constituents like Pb, Zn, S, and F. A particular question is whether deposits that are dominated by a particular element formed from brines that were correspondingly rich in that element. For example, recently Kenderes and Appold (2017) conducted a study of fluid inclusions from the Illinois-Kentucky Mississippi Valley-type (MVT) district (Fig. 2-1), where fluorite greatly dominates over minerals of Pb, Zn, and Ba, comprising about 30-40% of the total
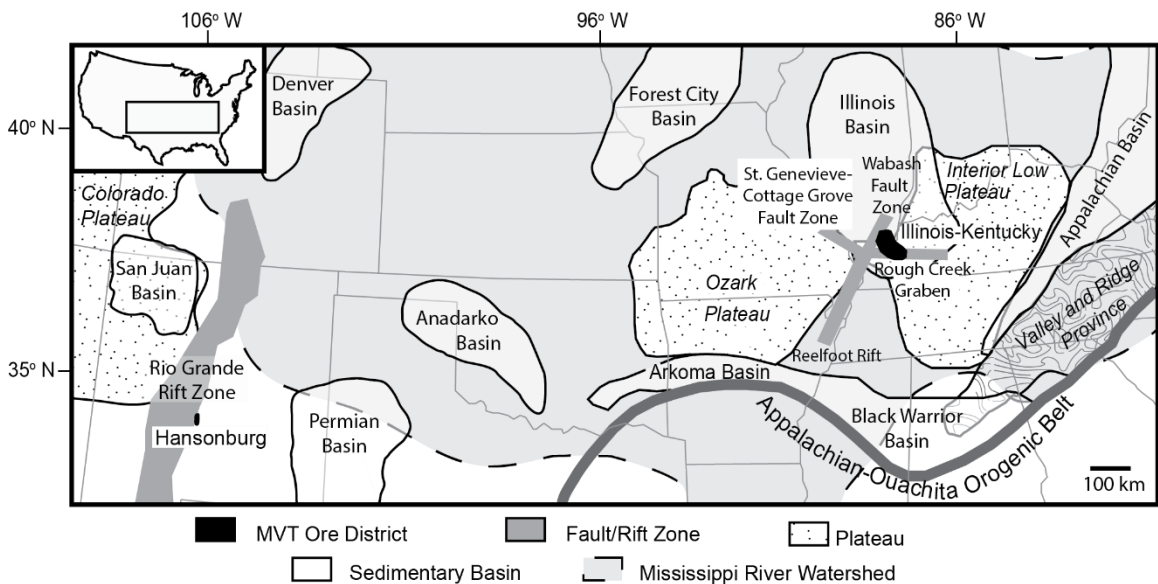
Figure 2-1. Map showing locations of the Hansonburg, New Mexico and Illinois-Kentucky MVT districts and major geologic features. Modified from Roedder et al. (1968) and Pelch et al. (2015).

mineralization (Denny et al., 2013). Their study showed that the Illinois-Kentucky mineralizing fluids were indeed rich in F with concentrations ranging from 680 to 2300 ppm, much higher than the 10s of ppm F concentrations typical of sedimentary brines (Appold, 2021). Similarly, a study by Putnam (1980) and Putnam et al. (1983) suggests that the Hansonburg, New Mexico mining district (Fig. 2-2), where fluorite comprises 10-23% of the total mineralization (Kottlowski, 1953; Williams et al., 1964; McLemore et al., 1998), was formed from F-rich fluids with concentrations between about 400 and 930 ppm. However, the methodology employed by Putnam (1980), and Putnam et al. (1983) causes some uncertainty about their results. That is, in contrast to Kenderes and Appold (2017), who analyzed individual fluid inclusions, Putnam (1980) and Putnam et al. (1983) analyzed bulk leachates comprised of mixtures of multiple fluid inclusions. Because bulk leachate analyses of fluid inclusions are susceptible to contamination from the host mineral matrix, and from secondary fluid inclusions, the actual F content of the Hansonburg mineralizing fluid is uncertain. In addition, because Putnam(1980) and Putnam et al. (1983) analyzed fluid inclusions hosted by galena, which only slightly overlaps fluorite in the paragenentic sequence, and a stage IV quartz sample from a site where fluorite is absent, the measured F concentrations may not be representative of F concentrations in the mineralizing fluid at the time of fluorite precipitation. Another study that attempted to measure F concentration in carbonate-hosted Zn-Pb mineralizing fluids was by Viets et al. (1996), who measured F/Cl ratios in fluid inclusions from 14 different MVT districts with variable fluorite abundances from around the world. Their data did not show any systematic correlation between fluorite abundance and mineralizing fluid F/Cl ratio, though they only analyzed 2-5 samples per district. In

addition, their data were obtained from bulk fluid inclusion leachates, again raising the possibility that the mineralizing fluid F signal was contaminated by F from the host mineral matrix or from secondary fluid inclusions. Thus, the concentration of F in the fluids that formed carbonate-hosted Zn-Pb deposits is not well established, and much more work is needed before any tendencies in mineralizing fluid F concentrations can be recognized.

Nonetheless, the recent study of the Illinois-Kentucky district by Kenderes and Appold (2017) is consistent with the hypothesis that fluorite-rich carbonate-hosted Zn-Pb deposits are formed from F-rich fluids, a hypothesis that can be tested further in the Hansonburg district (Fig. 2-2). The studies of Putnam (1980) and Putnam et al. (1983) also support this hypothesis, but their reported fluid inclusion F concentrations determined from bulk leachate analysis would be

Figure 2-2. Map of the U.S. state of New Mexico showing locations of the Hansonburg and other Rio Grande Rift MVT deposits and major geologic features. Modified from McLemore et al. (1988).

strengthened by corroboration from an individual fluid inclusion analytical technique. Increased confidence in the F concentration of Hansonburg mineralizing fluids would

also improve understanding of the origin of Hansonburg and fluorite-rich carbonate-hosted Zn-Pb deposits generally. For example, the association of fluorite deposits with continental rifts and lineaments has long been recognized and surmised to be the result of F-rich fluids emanating from the mantle (Worl, 1974; Van Alstine, 1976; Zappettini et al., 2017). The Illinois-Kentucky district fits this model in that it is located in a rift setting and formed from fluids that had a strong mantle component as indicated by $^3He/^4He$ ratios (Kendrick et al., 2002) and were apparently F-rich. The Hansonburg district, which lies in the Rio Grande rift, was formed from fluids that had a strong mantle component, as indicated by $\delta^{37}Cl$ and Br/Cl values (Partey et al., 2009), and may also have been F-rich. In addition, knowledge of mineralizing fluid F concentrations will provide another constraint on pH through the reaction

$$Ca^{2+}_{(aq)} + 2HF_{(aq)} \rightleftharpoons CaF_{2(s,fl)} + 2H^+_{(aq)} \tag{2-1}$$
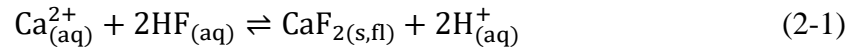
Putnam et al. (1983) reported a pH of 4.5 and Norman et al. (1985) reported a pH range of 4.3 to 5.1 for Hansonburg mineralizing fluids based on CO_2 contents in fluid inclusions and the assumption that the mineralizing fluid was in equilibrium with calcite. However, these calculations did not take into account the influence of HF on mineralizing fluid pH. Further, the CO_2 concentrations used to calculate pH were measured from bulk thermal fluid inclusion decrepitations in galena, fluorite, and quartz samples, leading to uncertainty about the source of the measured CO_2; i.e. whether the CO_2 was derived from fluids trapped at the time of mineral precipitation or from later fluids trapped in secondary fluid inclusions. Kenderes and Appold (2017) reported a calculated pH range of 0 to 1.4 for the Illinois-Kentucky mineralizing fluids based on their high Ca and F concentrations. The pH of the Hansonburg mineralizing fluid should also be low if its F

concentration was high. This would fundamentally affect how the mineralizing fluid transported and precipitated metals.

The purpose of the present study was to retest the hypothesis that the Hansonburg deposits were formed from a F-rich fluid by analyzing individual fluid inclusions rather than bulk mixtures of fluid inclusions. To that end, quartz-hosted fluid inclusions were thermally decrepitated and the compositions of the resulting solute mounds were individually analyzed using scanning electron microscope-energy dispersive X-ray spectroscopy (SEM-EDS).

2.3 Geologic Setting

The geologic setting of the Hansonburg deposits has been described in detail by Wilpolt and Wanek (1951), Kottlowski (1953), Kopicki (1962), Williams et al. (1964), Roedder et al. (1968), and Putnam et al. (1983). A summary of the geologic setting based on their work is provided here. The Hansonburg district is located on the eastern margin of the Rio Grande rift on the western face of the Oscura Mountains (Fig. 2-3). The

Figure 2-3. Simplified geologic map of the Hansonburg district showing locations of mines that provided samples used in this study. After Putnam (1983).

district is relatively small in geographic extent, with a north-south length of only about 5

km and an east-west length of no more than about 0.5 km, though exploratory drilling is reported to have intersected mineralization beyond this range (Putnam et al. 1983). Large-scale mining in the district has been limited by difficulties in separating the mixed barite-fluorite-galena ores and by lack of water to support mining operations (Norman et al., 1985), though some small-scale barite (32,400 metric tons), lead (5011 metric tons), and zinc (15 metric tons) production has occurred (Kottlowski, 1953; Williams et al., 1964; McLemore et al., 1998).

The stratigraphy of the Hansonburg district consists of granitic and gneissic Precambrian crystalline basement rocks overlain by Pennsylvanian sedimentary formations consisting of marine limestones, sandstones, and shales. Hansonburg mineralization occurs in pockets, cavities, and veins, or as bedding replacement deposits primarily in the Council Springs member of the Pennsylvanian aged Madera Limestone. The Council Springs member is a massive, silicified limestone that exhibits characteristic features of paleo-karst, including potholes on its unconformable upper contact, bedding-plane anastomoses, and dissolution cavities with diameters that range from a few centimeters to 50 meters (Kopicki, 1962; Putnam et al., 1983, Partey et al., 2009). Field evidence, including the unconformable upper contact of the Council Springs member, has been used to argue that the dissolution features are karst features formed by weathering during the Pennsylvanian (Putnam et al., 1983; North et al., 1985). However, Lueth et al. (2005) noted that a small subset of Hansonburg orebodies exhibit features consistent with sulfuric acid speleogenesis at the time of mineralization. Thus, the of timing of formation of dissolution cavities associated with the Hansonburg deposits remains ambiguous and may have occurred in multiple stages.

Hansonburg mineralization is exposed by north-trending *en echelon* normal faults in the Oscura uplift (Fig. 2-3). Movement along these faults began about 7 million years ago and is related to Rio Grande rifting (Chapin, 1979). Northwest-trending high angle fractures and reverse faults are exposed throughout the Hansonburg district and are thought to be related to shearing along the east-west trending Capitan lineament, which runs through the district. The Capitan lineament is thought to have been active during the Paleozoic period.

2.3.1. Nature of mineralization

Lueth et al. (2005) dated jarosite from the Hansonburg district using the $^{40}Ar/^{39}Ar$ method, determining a resultant mineralization age of 3.79 ± 0.16 to 7.97 ± 0.44 Ma. This age range lies within the age range of 3 to 9 Ma of nearby alkalic basalts dated by Seager et al. (1984) using the K-Ar method, and is coincident with late stage alkalic Rio Grande rift volcanism.

The principal hydrothermal minerals in Hansonburg consist of barite (9 to 59 wt. %), fluorite (10 to 23 wt. %), galena (1 to 5 wt. %), and quartz (Kottlowski, 1953; Williams et al., 1964; McLemore et al., 1998). Less abundant hydrothermal minerals include sphalerite, pyrite, chalcopyrite, calcite, and dolomite. Minor occurrences of secondary (supergene) minerals consist mainly of Pb, Cu, and Zn carbonate and sulfate minerals and selenite gypsum.

The general paragenetic sequence in Hansonburg (Fig. 2-4) can be broken down into four stages. The first stage is characterized by early silicification and dolomitization of the limestone with minor replacement of limestone by barite and galena. Stage two is characterized by sulfide minerals, primarily galena with some chalcopyrite, and minor barite. Stage three is characterized by multiple fluorite substages and barite. Stage four is characterized

Figure 2- 4. Paragenetic sequence of mineralization in the Hansonburg district. Adapted from Roedder et al. (1968) and Putnam (1980).

by colorless, smoky, and amethyst quartz with minor calcite. Drusy quartz precipitated during every paragenetic stage and largely overlapped the precipitation of other minerals in the paragenetic sequence noted above (Roedder et al., 1968, Putnam et al., 1983; Partey et al., 2009).

2.4 Methodology

2.4.1. Sample selection

The main focus of the present study was on primary fluid inclusions hosted in late stage II to stage III drusy quartz from the Hansonburg district. Drusy quartz was chosen for this study because it is transparent and precipitated over much of the paragenetic

17

sequence, overlapping multiple stages of fluorite precipitation (Fig. 2-4). A further

reason for choosing drusy quartz is that it does not incorporate much F into its matrix in

solid solution, thus reducing the risk of F contamination during fluid inclusion analyses.

Samples of drusy quartz were collected directly from exposures inside mine adits or from

surface spoil heaps associated with specific underground mines (Table 2-1). The

paragenetic position of the drusy quartz analyzed was identified based on careful

examination of its petrographic relationship with fluorite and galena.

Table 2-1. Geographic locations and identification codes of samples analyzed in the
present study.

Name	Sample ID prefix	UTM Easting	UTM Northing	UTM Zone	Latitude	Longitude
Hansonburg						
Blanchard mine						
Stop 1	HANBL1	372711	3742633	13S	33.81625 N	106.37536 W
Stop 2	HANBL1	372740	3742370	13S	33.81388 N	106.37501 W
South Cut	HANBLSC	372709	3741940	13S	33.81000 N	106.37528 W
Mex-Tex mine						
South Adit	HANMTSA	373545	3743742	13S	33.82635 N	106.36651 W
Royal Flush mine	HANRF	374130	3745516	13S	33.84242 N	106.36044 W
Illinois-Kentucky						
Deardorff mine	IKDM	0394032	4153297	16S	37.52055 N	88.19917 W

* All geographic coordinates were determined relative to the WGS 84 reference frame.

Once late stage II or stage III drusy quartz crystals had been identified, doubly

polished thin sections, about 100 to 200 μm thick, were prepared from them for fluid

inclusion analysis. Portions of thin sections in which primary fluid inclusion

assemblages suitable for analysis were identified were then broken out into chips that

ranged from 2-7 mm in diameter.

2.4.2 Microthermometry

Next, a Linkam THMSG600 heating-freezing stage located in the Department of

Geological Sciences at the University of Missouri--Columbia (MU) was used to perform

microthermometry on the fluid inclusions. Calibration of the Linkam stage was

accomplished using synthetic fluid inclusion standards including the melting temperature

of pure water (0° C), the critical temperature of pure water (374° C), the melting

temperature of pure CO_2 (−56.6° C), and the eutectic melting temperature for H_2O-NaCl

(−21.2° C). Measured homogenization temperatures (T_H) had a precision of ± 0.3° C and

measured last ice melting temperatures (T_m) had a precision of ± 0.2° C. The equation of

Bodnar (1993) was used to calculate equivalent weight percent (eq. wt%) NaCl from T_m.

2.4.3 SEM-EDS analysis

Following microthermometry, chips selected for F concentration analyses were

decrepitated by heating at a rate of 50° C per minute to a final temperature of

approximately 550° C in preparation for SEM-EDS analysis. This heating caused many

fluid inclusions to rupture and discharge their contents to the chips' surfaces, where the

water evaporated leaving evaporative solute mounds (Fig. 2-5A, B). When possible, the

evaporative mounds were correlated to their likely source fluid inclusions based on

relative proximity to one another.

Analyses of the evaporative solute mounds were performed using a Quanta 600F

environmental scanning electron microscope (ESEM) equipped with a Bruker Quanta

200 silicon drift detector (SDD) located at the MU Electron Microscopy Core. Samples

were affixed to aluminum stubs with carbon tape. To reduce charging of the quartz

chips, analyses were conducted under a low vacuum of 40 to 60 Pa.   Samples and
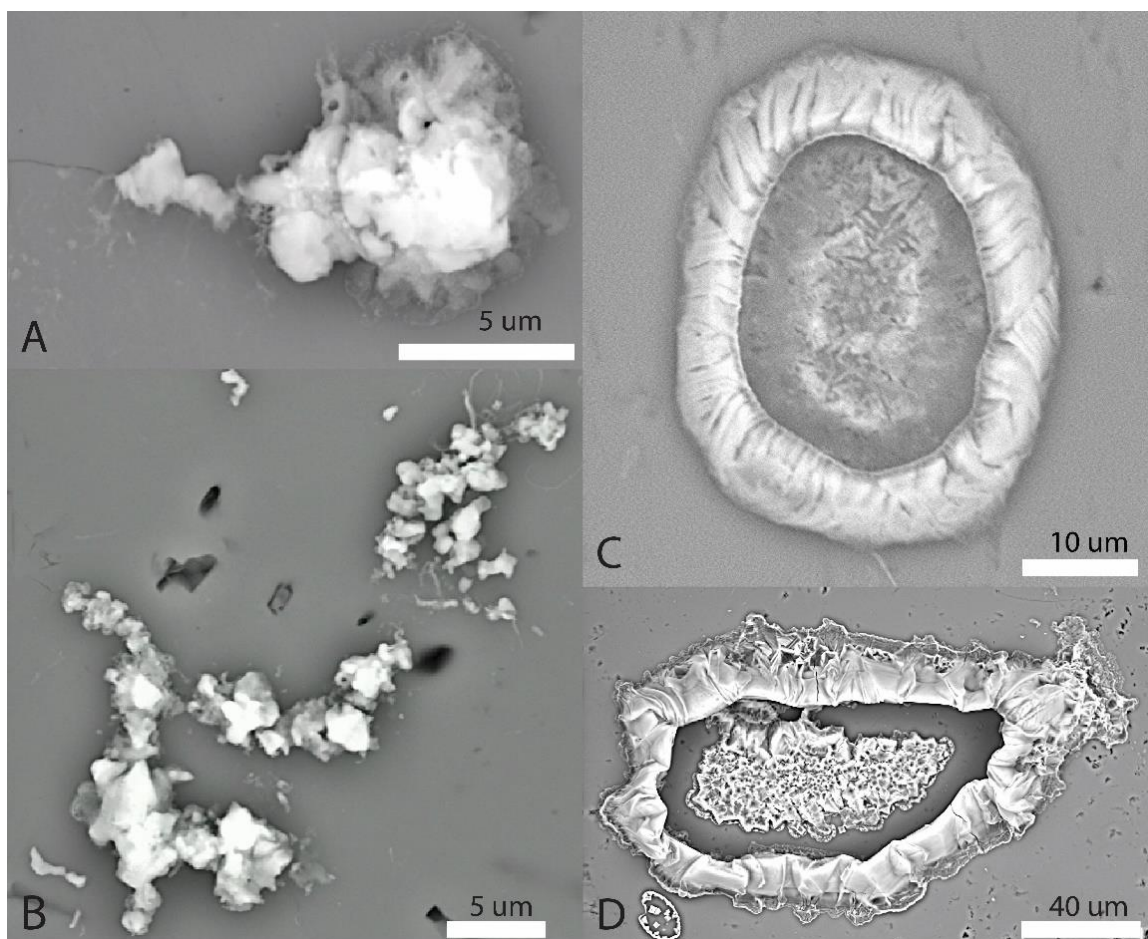
Figure 2-5. (A) and (B) Back-scattered electron (BSE) images of evaporative solute mounds generated from thermal decrepitation of quartz-hosted fluid inclusions from the Hansonburg and the Illinois-Kentucky districts, respectively. (C) and (D) BSE images of solute mounds generated from evaporation of droplets of standard solutions containing F concentrations of 206 ppm and 5060 ppm F, respectively. Evaporative solute mounds are lighter in color than the surrounding quartz matrix due to the presence of heavier elements, Cl, Ca, and K in the mounds as compared to the lighter Si and O in the quartz matrix.

standards were analyzed at accelerating voltages of 10, 15, and 20 keV to encompass the contrasting benefits of maximum signal generation produced at higher accelerating voltage and improved precision for light elements at lower accelerating voltage. A working distance of 10 ± 0.8 mm between the final pole piece of the lens and the sample surface was used. Spot sizes were chosen such that a count rate close to, but less than 130,000 counts per second (cps) was maintained when generating elemental maps. The

elements in the evaporative solute mounds targeted for analysis were C, O, F, Na, Mg, Al, Si, S, Cl, K, Ca, Fe, Cu, and Ag.

Element concentrations in the solute mounds were calculated from the SEM-EDS signals using the Phi-Rho-Z quantification method via the Bruker Espirit 2.0™ software. The boundaries of evaporative solute mounds targeted for composition analysis were carefully outlined so that only signal generated from the mounds and not the background mineral substrate was included in the quantification. Element maps were produced for each of these evaporative solute mounds in order to confirm correlation of F with Cl, an aqueous constituent not expected to be significantly present in any of the mineral hosts, and to look for "hotspots", i.e. small areas of elevated concentrations of one or more elements relative to the surrounding mound material. As hotspots of coincident Ca and F may have arisen from minute fluorite particles entrained within the fluid inclusion rather than true aqueous solute, mounds with more homogeneous element maps mounds were preferentially selected for quantification. Weight percent concentrations of elements in the evaporative solute mounds calculated using the Phi-Rho-Z method were then converted to atomic ratios relative to Cl.

2.4.4 Quantification

Determination of absolute fluid inclusion F concentrations from F/Cl ratios measured in the evaporative solute mounds required the generation of calibration curves specific to the instrument, operating conditions, and mineral substrate. To this end, three suites of five to six standard solutions containing known concentrations of F, Na, Mg, K, Cl, ± Ca were prepared (Table 2-2). The concentrations of Na, Mg, K, Cl, and Ca in the standard solutions were based on values reported by Wenz et al. (2012) for MVT

mineralizing fluids in the Ozark Plateau in the central U.S. Fluorine concentrations in the

standards ranged from 44 to 5,060 ppm.

Table 2-2. Standard solution compositions in ppm.

	Standard Suite 1					
	1-1	1-2	1-3	1-4	1-5	
F	106	201	504	1030	1880	
Cl	130,000	130,000	130,000	136,000	145,000	
Na	61,900	61,900	61,900	61,900	61,900	
Ca	15,500	15,500	15,500	15,500	15,500	
K	2,560	2,560	2,560	2,560	2,560	
Mg	1,650	1,650	1,650	1,650	1,650	
	Standard Suite 2					
	2-1	2-2	2-3	2-4	2-5	2-6
F	44	105	261	463	1040	2090
Cl	131000	131,000	131,000	131,000	131,000	142,000
Na	61,900	61,900	61,900	61,900	61,900	61,900
Ca	15,500	15,500	15,500	15,500	15,500	15,500
K	2,560	2,560	2,560	2,560	2,560	2,560
Mg	1,650	1,650	1,650	1,650	1,650	1,650
	Standard Suite 3 (No Ca)					
	3-1	3-2	3-3	3-4	3-5	3-6
F	138	252	517	1200	2560	5060
Cl	130,000	130,000	130,000	130,000	130,000	130,000
Na	62,100	62,100	62,100	62,100	62,100	62,100
K	2,960	2,960	2,960	2,960	2,960	2,960
Mg	1,560	1,560	1,560	1,560	1,560	1,560

In order to verify that all solutes remained in solution, aliquots of each standard solution

were examined using a microscope. Due to the low solubility of F in the presence of the

high Ca concentrations typical of MVT mineralizing fluids, on which the standard

solutions were modeled, a maximum F concentration of approximately 500 ppm was

found to be addable to the standard solutions at a pH of 4, the low end of the pH range of

4 to 5.5 typical of MVT mineralizing fluids (Sverjensky, 1984), before causing

precipitation of CaF_2. Higher concentrations of F up to about 2,000 ppm could be added

to the standard solutions by lowering the pH of the solutions to about 0.5 through the addition of HCl. Even higher concentrations of F up to 5,060 ppm were attained in suite three of the standard solutions by not including any Ca in the solutions.

Next, fine droplets of the standard solutions were sprayed with an atomizer onto clean thin sections of quartz that had been heated on a hot plate to a temperature of 150° C. Upon contact with the heated quartz thin sections, the droplets quickly evaporated, leaving behind oval to sub-oval solute mounds with thick rims and thinner centers (Fig. 2-5C, D). Heating the thin sections of quartz was found to be necessary in order to ensure the formation of compositionally homogeneous evaporative mounds, which was caused by the rapid evaporation of the water droplets. When the thin sections were not heated and the water droplets evaporated slowly, compositionally heterogeneous mounds formed, characterized by large halite crystals amidst smaller crystals of other minerals.

A total of 48 evaporative solute mounds derived from droplets of the standard solutions were analyzed to generate calibration curves. Mounds with diameters of less than 100 μm were targeted for generating the calibration curves so that the curves would be based on mounds that were as similar as possible in size to those derived from the fluid inclusions, thereby avoiding any possible artifacts caused by size differences. Standard solution mounds that were chosen for calculating the calibration curves had amorphous textures and homogeneous elemental distributions. Standard solution evaporative solute mounds were then analyzed at accelerating voltages of 10, 15, and 20 keV, as was done for the fluid inclusion evaporative solute mounds. For each accelerating voltage, the measured atomic F/Cl ratios in the evaporative solute mounds
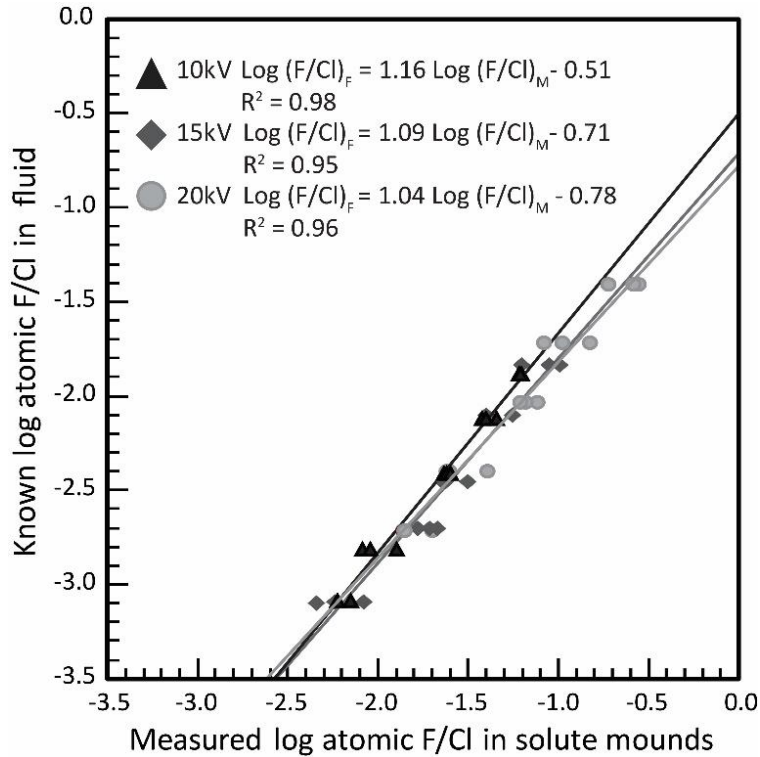
Figure 2-6. Experimentally determined correlations between known atomic F/Cl ratios in standard solutions and atomic F/Cl ratios in evaporative solute mounds formed from droplets of the standard solutions and measured using SEM-EDS. Standard solution evaporative solute mounds were analyzed at accelerating voltages of 10, 15, and 20 keV. The resultant linear regression equations shown in the upper left corner of the plot were used to calculate atomic F/Cl ratios in fluid inclusions based on the atomic F/Cl ratios of evaporative solute mounds formed from decrepitation of the fluid inclusions.

(F/Cl_M) were plotted versus the known atomic F/Cl ratios in the mounds' source standard solution fluids (F/Cl_F).

Linear regression of the points for each accelerating voltage was carried out to generate accelerating voltage specific calibration curves (Fig. 2-6). Linear regression of analyses completed using 10 keV accelerating voltage resulted in equation (2-2) below.

$$\log F/Cl_F = 1.16 * \log F/Cl_M - 0.51 \tag{2-2}$$

For analyses completed using 15 keV accelerating voltage, linear regression generated equation (2-3),

$$\log F/Cl_F = 1.09 * \log F/Cl_M - 0.71 \tag{2-3}$$

and linear regression of analyses done using 20 keV generated equation (2-4)

$$\log F/Cl_F = 1.04 * \log F/Cl_M - 0.78 \tag{2-4}$$

In the above equations, $(F/Cl)_F$ represents the atomic F/Cl value known for the standard solution fluid and $(F/Cl)_M$ represents the atomic F/Cl values measured in the solute mounds. For the standard solutions, $(F/Cl)_M$ is systematically higher than $(F/Cl)_F$ by 0.6 to 1.0 log units. Measured $(F/Cl)_M$ values generally lie within 0.25 log unit of the $(F/Cl)_M$ corresponding mean $(F/Cl)_M$ value.

In the course of computing these calibration curves, accelerating voltage specific detection limits for absolute F concentration in the fluid could also be determined based on the lowest detectable F concentrations in the standard solutions in Table 2-2. These detection limits were found to be around 100 ppm at 10 keV, between 44 and 105 ppm at 15 keV, and between 138 and 252 ppm at 20 keV.

Using the appropriate energy-specific calibration curves, atomic F/Cl values in fluid inclusions were calculated from the atomic F/Cl values measured in evaporative solute mounds derived from decrepitation of the fluid inclusions. Absolute F concentrations in the fluid inclusions were determined by multiplying the fluid inclusions' atomic F/Cl ratios by their estimated absolute Cl concentration. The Cl concentration used to calculate F concentration in any fluid inclusion was the average Cl concentration in all fluid inclusions in the host thin section chip. Fluid inclusion Cl concentrations were estimated from salinities determined from microthermometry, in which Cl was assumed to be more abundant than any other anion by at least one order of magnitude. This assumption is based on previous studies of the composition of fluid

inclusions in the Hansonburg district, in which the concentrations of Cl were reported to be 50 to more than 100 times greater than the concentrations of other anions (Putnam et al. 1983; Böhlke and Irwin, 1992; Partey et al., 2009). The Cl concentrations of 45,000 to 83,000 ppm estimated in the present study lie within the range of Cl concentrations of 24,000 to 99,000 ppm reported by Putnam et al. (1983) and Böhlke and Irwin (1992) for the Hansonburg district.

Although the focus of the present study was on the Hansonburg district, some samples of ore-stage quartz from the Illinois-Kentucky fluorite district were also studied according to the same procedures described above. Kenderes and Appold (2017) had previously measured F concentration in fluid inclusions from the Illinois-Kentucky district, but only for fluid inclusions hosted in sphalerite. By also determining F concentration in some quartz-hosted fluid inclusions from the Illinois-Kentucky district, a more direct comparison of fluid composition between the two districts can be made.

2.5 Results

2.5.1 Fluid inclusion petrography

About 90% of the fluid inclusions observed in the present study were primary, based on their petrographic association with recognizable primary growth features. Primary fluid inclusions in Hansonburg drusy quartz samples were observed to have two principal modes of occurrence. Most primary fluid inclusions occur in thick clusters that appear wedge-shaped when viewed in a plane that is perpendicular to the c axis (Fig. 2-7A-C). The fluid inclusions in these clusters are elongated in the direction of crystal growth, are distributed radially around the c axis, and are 4 to 50 µm in length with average length:width ratios of about two (Fig. 2-7C). About 15% of these fluid

26
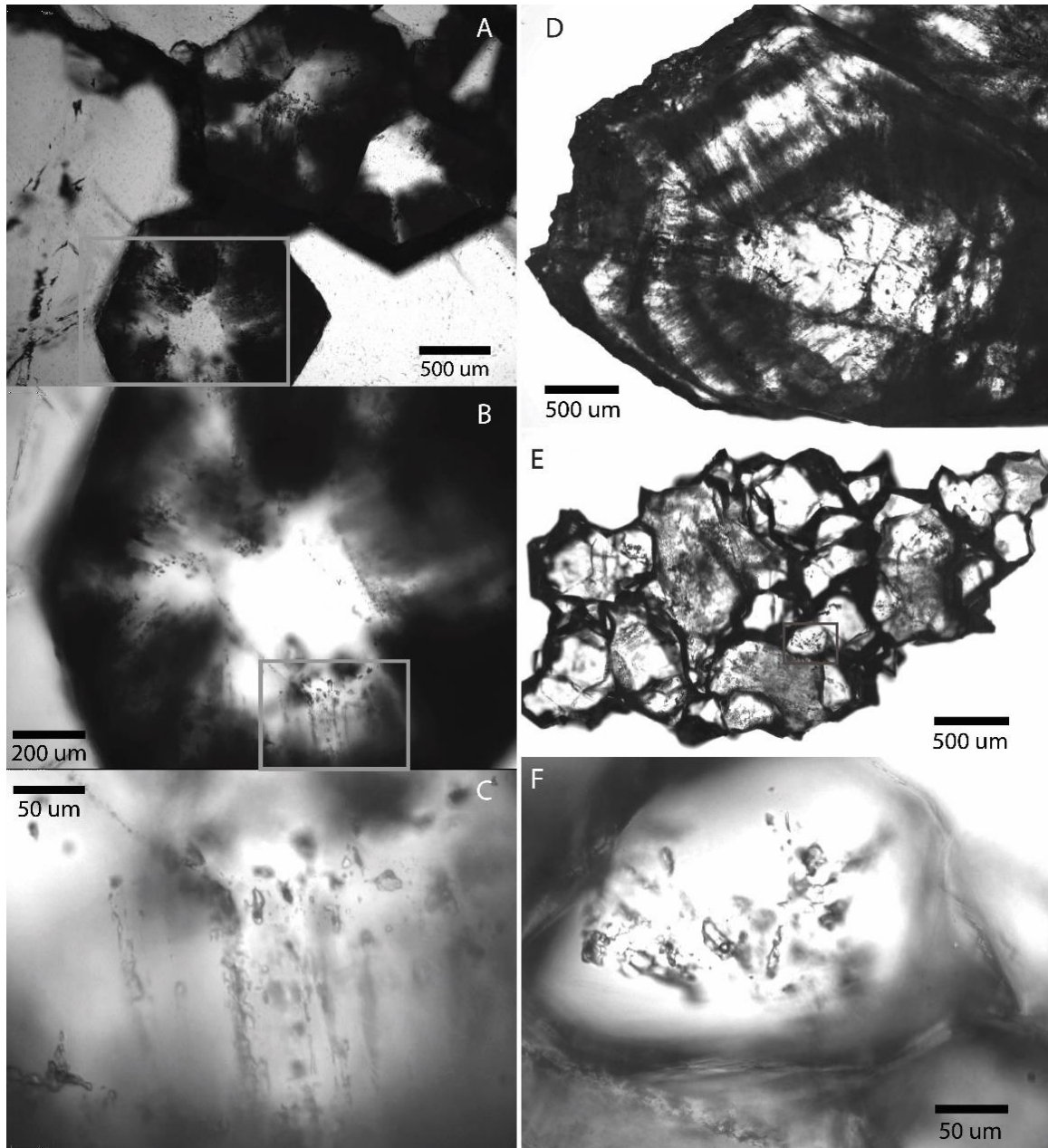
Figure 2-7. Photomicrographs of typical fluid inclusions hosted by drusy quartz from the Hansonburg district, shown under plane polarized transmitted light. (A-C) Sample HANBL1-1 at magnifications of 40x, 100x, and 400x, respectively, showing wedge-shaped fields of fluid inclusions in a quartz crystal. The view in these photomicrographs is perpendicular to the c-axis. FIA 6 is visible in C and inside the gray box in B. (D) Growth zones in drusy quartz in sample HANBL2-1 shown at 40x magnification from a view parallel to the c axis. Fluid inclusions are visible in the core of the crystal. (E-F) FIA 3, consisting of a cluster of fluid inclusions within a crystal in sample HANMTSA-12 at 40x and 400x magnification, respectively. Gray rectangles in A, B, and E indicate areas shown at greater magnification in B, C, and F, respectively.

27

inclusions appear to be necked down. In planes parallel or nearly parallel to the c-axis, the density of fluid inclusions in the quartz varies systematically to form concentric alternating light and dark bands (Fig. 2-7D). The second major mode of occurrence of primary fluid inclusion assemblages consists of nonplanar clusters of 3 to 10 fluid inclusions in the center of drusy quartz crystals (Fig. 2-7E-F). These fluid inclusions range in diameter from about 10 to 150 μm. For both modes of occurrence, the great majority of primary fluid inclusions contain two phases at 25° C--an aqueous liquid phase and a vapor phase, where the volume of liquid is greater than that of vapor. The remaining fluid inclusions contain a single aqueous liquid phase at 25° C. The single-phase fluid inclusions are petrographically associated with two-phase fluid inclusions that show evidence of necking down. This suggests that the single-phase fluid inclusions were originally part of larger fluid inclusions that completed the necking down process after the vapor phase had separated from the liquid phase.

2.5.2 Microthermometry

The Hansonburg drusy quartz-hosted fluid inclusions measured in this study have T_h values ranging from 115 to 217° C with a mean of 167° C, where more than 90% of the values lie between 130 and 190° C (Fig. 2-8, Table 2-3). The salinities of these
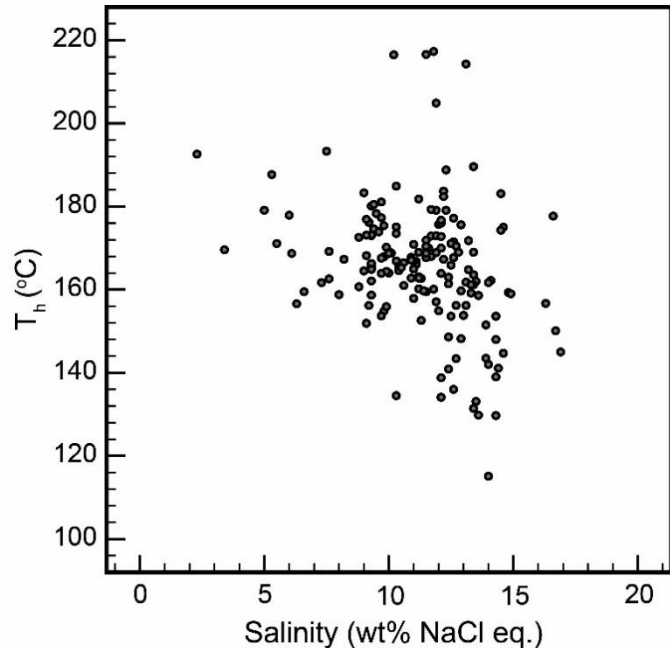
Figure 2-8. Homogenization temperature (°C) vs. salinity as wt% NaCl eq. measured in drusy quartz-hosted fluid inclusions from the Hansonburg district.

fluid inclusions range from 2.3 to 16.9 wt% NaCl eq. with a mean of 11 wt% NaCl eq.,

where more than 90% of the values lie between 8 and 15 wt% NaCl eq. The T_h and

salinity values measured in the present study are in excellent agreement with the T_h and

salinity values reported for fluorite-hosted fluid inclusions in earlier studies (Ames, 1958;

Roedder et al., 1968; Putnam, 1980; Böhlke and Irwin, 1992).

Table 2-3. Microthermometry results for drusy quartz-hosted fluid inclusions from the
Hansonburg, NM district.

Sample ID	Chip ID	FIA ID	Inclusion ID	Area (µm²)	T_h (°C)	Salinity (wt% NaCl eq)
HANBL1-1	1	1	1	630	172.6	8.8
HANBL1-1	1	1	2	1448	180.1	9.3
HANBL1-1	1	1	3	451	173.0	9.3
HANBL1-1	1	1	4	480	175.2	\
HANBL1-1	1	2	1	1912	174.6	9.4
HANBL1-1	1	2	2	1579	176.2	9.2
HANBL1-1	1	2	3	610	176.9	9.1
HANBL1-1	2	1	1	203	\	9.8
HANBL1-1	2	1	2	143	164.0	10.0
HANBL1-1	2	1	3	73	161.3	\
HANBL1-1	2	1	4	334	168.2	9.1
HANBL1-1	3	1	1	1360	175.1	10.3
HANBL1-1	3	1	2	859	169.2	10.0
HANBL1-1	3	1	3	1504	173.5	10.3
HANBL1-1	3	1	4	839	173.9	9.6
HANBL1-1	5	1	1	230	177.9	6.0
HANBL1-1	5	1	2	166	175.4	9.8
HANBL1-1	5	1	3	109	176.3	\
HANBL1-1	5	2	1	1355	164.4	9.9
HANBL1-1	5	2	2	478	166.9	10.3
HANBL1-1	5	2	3	168	161.0	10.6
HANBL1-1	5	2	4	231	166.5	10.6
HANBL1-1	5	3	1	820	179.1	5.0
HANBL1-1	5	3	2	348	165.6	9.3
HANBL1-1	5	3	3	989	165.6	10.4
HANBL1-1	5	4	1	984	158.6	13.6
HANBL1-1	5	4	2	1068	162.2	14.1
HANBL1-1	5	4	3	1624	162.0	13.5
HANBL1-1	5	4	4	423	159.2	13.3
HANBL1-1	6	1	1	599	183.3	9.0
HANBL1-1	6	1	2	1893	192.6	2.3
HANBL1-1	6	1	3	606	181.1	9.7
HANBL1-1	6	2	1	108	194.0	\
HANBL1-1	6	2	2	176	168.7	6.1

Sample ID	Chip ID	FIA ID	Inclusion ID	Area (µm²)	T_h (°C)	Salinity (wt% NaCl eq)
HANBL1-1	6	3	1	75	169.0	11.2
HANBL1-1	6	3	2	324	168.8	10.1
HANBL1-1	6	3	3	63	164.6	10.4
HANBL1-1	6	4	1	443	173.2	9.3
HANBL1-1	6	4	2	222	166.3	9.3
HANBL1-1	6	4	3	244	177.3	9.7
HANBL1-1	6	4	4	246	178.3	9.5
HANBL1-1	6	5	1	69	158.8	8.0
HANBL1-1	6	5	2	109	158.7	9.3
HANBL1-1	6	5	3	56	166.6	\
HANBL1-1	7A	1	1	125	164.3	\
HANBL1-1	7A	1	2	300	162.6	7.6
HANBL1-1	7A	1	3	73	161.7	7.3
HANBL1-1	7A	1	4	48	160.7	8.8
HANBL1-1	7A	1	5	92	160.8	\
HANBL1-1	7A	2	1	125	159.5	6.6
HANBL1-1	7A	2	2	154	156.6	6.3
HANBL1-1	7A	2	3	56	165.4	\
HANBL1-1	7B	3	1	3146	170.0	11.6
HANBL1-1	7B	3	2	2376	157.1	11.9
HANBL1-1	7B	3	3	1860	179.1	11.9
HANBL1-1	7B	4	1	87	168.0	11.7
HANBL1-1	7B	4	2	858	163.9	12.1
HANBL1-1	7B	4	3	1300	165.9	12.5
HANBL1-1	7B	5	1	304	164.5	9.0
HANBL1-1	7B	5	2	42	154.8	9.8
HANBL1-1	7B	5	3	81	156.2	9.2
HANBL1-1	7B	5	4	336	164.9	9.3
HANBL1-1	8	1	1	650	167.7	11.5
HANBL1-1	8	1	2	306	216.6	11.5
HANBL1-1	8	1	3	542	162.8	10.9
HANBL1-1	8	1	4	122	170.4	11.5
HANBL1-1	8	2	1	83	153.7	9.7
HANBL1-1	8	2	2	646	167.9	9.8
HANBL1-1	8	2	3	42	170.2	9.9
HANBL1-1	8	3	1	536	166.8	11.1
HANBL1-1	8	3	2	78	166.5	\
HANBL1-1	8	3	3	772	161.8	13.1
HANBL1-1	8	4	1	9838	173.1	9.1
HANBL1-1	8	4	2	3860	168.7	10.0
HANBL1-1	8	4	3	1079	180.5	9.4
HANBL1-1	8	5	1	111	172.9	11.7
HANBL1-1	8	5	2	59	183.7	12.2
HANBL1-1	8	5	3	148	169.6	3.4
HANBL1-1	8	5	4	166	179.3	11.7
HANBL1-1	8	6	1	55	163.9	9.7
HANBL1-1	8	6	2	52	167.6	9.7

Sample ID	Chip ID	FIA ID	Inclusion ID	Area (µm²)	T_h (°C)	Salinity (wt% NaCl eq)
HANBL1-1	8	6	3	1466	169.2	7.6
HANBL1-1	8	7	1	266	171.1	5.5
HANBL1-1	8	7	2	335	167.3	8.2
HANBL1-1	8	7	3	60	187.7	5.3
HANBL2-1	3	1	1	77	216.5	10.2
HANBL2-1	3	1	2	63	217.3	11.8
HANBL2-1	3	1	3	47	217.3	\
HANBL2-1	3	2	1	275	175.7	\
HANBL2-1	3	2	2	324	204.9	11.9
HANBL2-1	3	2	3	56	188.8	12.3
HANBL2-1	3	2	4	259	179.1	12.3
HANBL2-1	3	3	1	216	173.0	11.9
HANBL2-1	3	3	2	17	172.8	12.1
HANBL2-1	3	3	3	274	184.9	10.3
HANBL2-1	3	3	4	633	\	11.4
HANBL2-1	3	3	5	193	165.3	10.5
HANBL2-1	3	5	1	154	171.5	12.6
HANBL2-1	3	5	2	513	175.7	12.0
HANBL2-1	3	5	3	97	156.2	13.1
HANBL2-1	3	5	4	2460	163.5	\
HANBL2-1	3	5	5	43	175.6	12.9
HANBLSC-1	1	1	1	160	166.1	11.1
HANBLSC-1	1	1	2	102	165.0	11.0
HANBLSC-1	1	1	3	133	167.8	10.9
HANBLSC-1	1	1	4	480	160.2	11.2
HANBLSC-1	1	1	5	83	162.7	11.3
HANBLSC-1	1	2	1	215	167.5	10.9
HANBLSC-1	1	2	2	72	166.8	11.0
HANBLSC-1	1	2	3	48	170.9	11.0
HANBLSC-1	1	2	4	70	181.8	11.2
HANBLSC-1	1	2	5	31	167.1	10.9
HANBLSC-1	2	1	1	41	163.1	11.2
HANBLSC-1	2	1	2	11	152.6	11.3
HANBLSC-1	2	1	3	122	161.4	12.4
HANBLSC-1	3	1	1	71	162.8	11.2
HANBLSC-1	3	1	2	517	160.4	\
HANBLSC-1	3	1	3	912	159.5	11.5
HANBLSC-1	3	1	4	189	160.1	11.8
HANBLSC-1	3	1	5	562	158.1	\
HANBLSC-1	4	1	1	521	171.9	11.5
HANBLSC-1	4	1	2	610	163.0	12.4
HANBLSC-1	4	1	3	79	161.7	14.0
HANBLSC-1	4	1	4	249	167.7	12.6

Sample ID	Chip ID	FIA ID	Inclusion ID	Area (μm²)	T_h (°C)	Salinity (wt% NaCl eq)
HANBLSC-7	1	1	1	349	151.9	9.1
HANBLSC-7	1	1	2	127	159.7	11.4
HANBLSC-7	1	1	3	276	160.6	\
HANBLSC-7-1	1	1	4	1862	157.9	11.0
HANBLSC-7-1	1	1	5	46	162.1	9.3
HANBLSC-7-1	1	2	1	221	134.1	12.1
HANBLSC-7-1	1	2	2	247	169.0	13.4
HANBLSC-7-1	1	2	3	612	167.3	12.2
HANBLSC-7-1	1	3	1	2126	158.7	9.3
HANBLSC-7-1	1	3	2	83	134.5	10.3
HANBLSC-7-1	1	3	3	185	155.9	9.9
HANMTSA-11	2	2	1	1310	168.7	11.5
HANMTSA-11	2	2	2	124	170.0	12.1
HANMTSA-11	2	2	3	190	176.0	12.1
HANMTSA-11	2	2	4	39	168.9	11.9
HANMTSA-11	3	1	1	18	183.1	14.5
HANMTSA-11	3	1	2	31	159.3	14.8
HANMTSA-11	3	1	3	11	203.7	\
HANMTSA-11	3	1	4	11	168.3	\
HANMTSA-11	3	1	5	55	177.7	\
HANMTSA-11	3	2	1	39	175.0	14.6
HANMTSA-11	3	2	2	136	182.4	12.2
HANMTSA-11	3	2	3	39	214.3	13.1
HANMTSA-11	3	3	1	79	177.2	12.6
HANMTSA-11	3	3	2	356	176.7	12.1
HANMTSA-11	3	3	3	48	171.1	12.5
HANMTSA-12	1	1	1	1536	131.4	13.4
HANMTSA-12	1	1	2	907	153.6	14.3
HANMTSA-12	1	1	3	1588	145.0	16.9
HANMTSA-12	1	2	1	678	138.8	12.1
HANMTSA-12	1	2	2	290	193.3	7.5
HANMTSA-12	1	3	1	665	144.7	14.6
HANMTSA-12	1	3	2	1407	\	13.3
HANMTSA-12	2	1	1	742	143.5	13.9
HANMTSA-12	2	1	2	312	115.1	14.0
HANMTSA-12	2	1	3	55	129.7	14.3
HANMTSA-12	2	2	1	1207	159.0	14.9
HANMTSA-12	2	2	2	886	156.7	16.3
HANMTSA-12	2	3	1	1953	171.8	13.2
HANMTSA-12	2	3	2	397	189.6	13.4
HANMTSA-12	2	4	1	96	150.1	16.7
HANMTSA-12	2	4	2	43	129.8	13.6
HANMTSA-12	2	4	3	82	142.0	14.0
HANMTSA-12	3	1	1	5820	139.0	14.3
HANMTSA-12	3	1	2	317	\	13.7

Sample ID	Chip ID	FIA ID	Inclusion ID	Area (μm²)	T_h (°C)	Salinity (wt% NaCl eq)
HANMTSA-12	3	2	1	23	140.9	12.4
HANMTSA-12	3	2	2	25	153.6	12.5
HANMTSA-12	3	2	3	150	136.0	12.6
HANMTSA-12	3	2	4	44	\	12.5
HANRF-15	1	1	1	171	161.2	13.4
HANRF-15	1	1	2	93	163.6	13.4
HANRF-15	1	1	3	443	164.8	13.2
HANRF-15	1	1	4	179	161.2	13.3
HANRF-15	1	1	5	143	156.2	12.7
HANRF-15	1	2	1	70	143.4	12.7
HANRF-15	1	2	2	78	169.0	12.8
HANRF-15	1	2	3	16	170.4	\
HANRF-15	1	2	4	68	148.6	12.4
HANRF-15	1	2	5	177	154.9	12.0
HANRF-15	2	1	1	92	153.8	13.0
HANRF-15	2	1	2	24	170.5	12.7
HANRF-15	2	1	3	41	148.2	12.9
HANRF-15	2	1	4	19	159.7	12.9
HANRF-15	3	1	1	3760	151.5	13.9
HANRF-15	3	1	2	230	148.0	14.3
HANRF-15	3	1	3	191	133.1	13.5
HANRF-15	3	1	4	2773	141.1	14.4
HANRF-15	3	1	5	476	174.3	14.5

2.5.3 SEM-EDS

Sixty-one SEM-EDS analyses of evaporative solute mounds derived from decrepitated fluid inclusions were performed in this study. Of these, 54 were from stage II to stage III drusy quartz from Hansonburg (Table 2-4). The other seven were from ore-stage quartz from the Illinois-Kentucky district. Evaporative solute mounds were identified based on their morphology, texture, and chemical signature in back scattered electron (BSE) images. Mound shapes ranged from subcircular to highly elongate, where length:width ratios exceeded 10. Mound widths were typically on the order of 1s of μm and lengths ranged from 1s to a few 10s of μm. Mound textures varied from homogeneous clusters of very fine-grained amorphous particles to heterogeneous clusters containing cubic crystals of halite surrounded by finer-grained evaporate residue.

Table 2-4. Elemental compositions of evaporative solute mounds derived from fluid inclusions as determined by SEM-EDS analysis.

Sample ID	Mound ID	C (wt%)	O (wt%)	F (wt%)	Na (wt%)	Mg (wt%)	Al (wt%)	Si (wt%)	S (wt%)	Cl (wt%)	K (wt%)	Ca (wt%)	Fe (wt%)	Cu (wt%)	Ag (wt%)
Hansonburg, NM fluid inclusions															
HANBL1-1	1-1	4.7	44	0.35	4.4	0.02	0.48	41	0.01	5.3	-	0.11	0.03	-	-
HANBL1-1	1-2	5.6	42	0.74	5.3	-	0.49	38	0.39	6.7	-	0.17	0.05	0.11	-
HANBL1-1	2-1A	5.0	42	0.56	6.3	0.04	0.52	38	-	7.7	0.09	0.39	-	-	-
HANBL1-1	2-1B	5.0	42	0.55	6.4	0.03	0.51	38	-	7.7	0.09	0.39	-	-	-
HANBL1-1	2-2	9.1	35	2.5	13	0.07	0.36	22	0.10	17	0.33	1.2	-	-	-
HANBL1-1	2-3	8.2	38	1.1	11	0.03	0.36	25	0.08	15	0.10	0.43	0.03	-	-
HANBL1-1	2-4	14	33	1.2	10	0.06	0.49	24	-	16	0.30	0.62	0.09	0.16	-
HANBL1-1	2-5	15	38	0.48	7.5	-	0.42	29	0.01	9.8	0.16	0.24	-	-	-
HANBL1-1	3-1	12	33	1.9	12	0.03	0.54	20	0.09	17	0.50	0.86	-	-	-
HANBL1-1	3-2	14	36	2.1	9.1	0.02	0.97	24	0.03	12	0.20	1.1	-	-	-
HANBL1-1	3-3	13	35	2.8	8.8	-	0.37	26	0.01	12	0.17	1.6	0.05	-	-
HANBL1-1	5-2	17	34	1.5	11	-	0.29	21	0.47	13	0.08	1.1	-	-	-
HANBL1-1	5-3	13	33	1.8	13	-	0.33	21	1.1	15	0.16	1.2	-	-	-
HANBL1-1	5-4	19	31	0.98	12	-	0.26	20	0.12	16	0.06	0.85	-	-	-
HANBL1-1	5-5	12	36	2.2	11	-	0.34	23	0.83	13	0.10	1.4	-	-	-
HANBL1-1	5-6	5.8	39	1.3	10	-	0.34	27	0.42	14	-	1.2	-	-	-
HANBL1-1	6-1A	6.9	35	1.5	11	0.08	0.34	27	0.14	16	-	1.2	-	-	0.18
HANBL1-1	6-1B	4.6	36	2.4	11	0.06	0.40	27	0.16	16	-	2.2	0.05	-	0.02
HANBL1-1	7-1	5.4	44	0.54	5.0	-	0.45	36	0.22	4.9	-	0.75	0.04	-	2.1
HANBL1-1	7-4	6.2	40	0.32	8.3	-	0.41	33	0.34	9.9	-	0.42	0.02	-	0.88
HANBL1-1	7-5	6.4	39	0.43	8.4	0.06	0.43	32	0.42	9.7	0.08	0.61	-	-	1.5
HANBL1-1	8-1	8.6	32	1.2	14	0.10	0.49	29	0.12	14	0.35	0.36	0.01	-	-
HANBL1-1	8-2	16	29	1.4	15	0.06	0.29	18	0.11	20	0.34	0.47	-	-	-
HANBL1-1	8-3	13	37	1.1	11	0.10	0.42	23	0.07	13	0.29	0.26	-	-	-

Sample ID	Mound ID	C (wt%)	O (wt%)	F (wt%)	Na (wt%)	Mg (wt%)	Al (wt%)	Si (wt%)	S (wt%)	Cl (wt%)	K (wt%)	Ca (wt%)	Fe (wt%)	Cu (wt%)	Ag (wt%)
HANBL1-1	8-5	11	40	0.96	8.0	0.09	0.52	33	0.03	6.6	0.15	0.17	-	-	-
HANBL2-1	1-1	8.1	40	1.1	9	0.05	0.37	29	0.03	11	0.39	0.46	-	-	-
HANBL2-1	1-2	4.4	45	0.64	6	0.07	0.43	35	-	7.9	-	0.28	-	-	-
HANBL2-1	1-3	1.9	45	0.85	7	0.05	0.44	35	-	9.3	0.19	0.28	-	-	-
HANBL2-1	2-1	7.3	47	0.37	3	0.05	0.45	37	0.09	3.9	-	0.19	-	-	-
HANBL2-1	2-3	9.4	43	1.3	6	0.16	0.48	31	0.01	7.3	-	0.62	-	-	-
HANBL2-1	3-1	11	37	0.38	9	-	0.30	31	-	11	0.10	0.14	-	-	-
HANBL2-1	3-3	8.8	45	0.67	3	0.09	0.48	39	0.01	3.2	-	0.24	0.02	-	-
HANBL2-2	1-1	9.2	36	1.4	11	0.08	0.52	27	0.03	14	-	0.79	0.06	-	-
HANBLSC-7-1	1-2	2.6	42	0.68	8	-	0.41	36	0.04	9.2	0.06	0.40	-	-	-
HANBLSC-7-1	1-2B	2.4	46	0.81	5	0.10	0.52	38	0.18	5.9	0.19	0.87	-	-	-
HANBLSC-7-1	1-3	7.3	48	0.46	3	0.06	0.28	37	0.08	3.3	-	0.37	0.03	-	-
HANBLSC-7-1	2-1	6.2	39	1.1	9	0.05	0.46	33	0.03	10	0.08	0.58	0.01	-	-
HANBLSC-7-1	2-2	8.5	44	0.61	4	0.08	0.56	37	0.03	4.7	-	0.15	-	-	-
HANBLSC-7-1	3-1A	5.3	43	1.0	5	0.10	0.46	39	-	5.9	-	0.32	0.04	-	-
HANBLSC-7-1	3-1B	4.8	45	0.51	3	0.08	0.60	42	0.02	3.9	0.13	0.15	0.03	-	-
HANBLSC-7-1	3-1C	6.9	44	0.85	5	-	0.41	38	-	5.2	0.08	0.36	0.07	-	-
HANBLSC-7-1	3-2	4.8	43	0.71	7	0.09	0.48	37	0.01	6.9	-	0.18	0.01	-	-
HANBLSC-7-1	3-3	5.0	40	0.45	9	0.06	0.41	35	0.02	10	-	0.20	0.02	-	-
HANBLSC-7-1	4-1	8.8	33	1.7	13	0.11	0.46	27	0.07	15	0.20	0.47	0.01	-	-
HANMTSA-12	1-1	3.0	45	0.52	4	-	0.34	42	-	4.5		0.20	0.01	-	-
HANMTSA-12	1-3	4.0	43	0.53	5	-	0.24	39	0.10	7.6	0.16	0.29	0.02	-	-
HANMTSA-12	1-4	9.4	43	0.54	6	0.11	0.29	34	0.05	6.2	-	0.15	-	-	-

Sample ID	Mound ID	C (wt%)	O (wt%)	F (wt%)	Na (wt%)	Mg (wt%)	Al (wt%)	Si (wt%)	S (wt%)	Cl (wt%)	K (wt%)	Ca (wt%)	Fe (wt%)	Cu (wt%)	Ag (wt%)
HANMTSA-12	2-6	9.8	38	0.93	8	-	0.16	32	0.04	10	-	0.35	-	-	-
HANMTSA-12	2-1	19	35	0.73	11	0.12	0.21	21	0.08	12	-	0.23	-	-	-
HANMTSA-12	3-1	5.9	33	0.84	16	-	0.24	24	-	19	-	0.27	-	-	-
HANMTSA-12	3-2	5.0	42	0.48	6	0.05	0.30	38	-	7.7	-	0.16	0.02	-	-
HANMTSA-12	3-3	12	34	0.43	12	-	0.13	25	0.02	16	0.07	0.15	-	-	-
HANRF-15*	1-1	5.7	44	0.56	6	-	0.39	38	0.01	4.2	-	0.04	0.04	-	-
HANRF-15	1-2	6.9	33	1.5	15	0.06	0.36	24	0.06	18	0.13	0.55	0.02	-	-
Illinois-Kentucky fluid inclusions															
IKDM1-1	2-3	3.6	27	2.1	19	0.30	0.42	17	0.07	29	0.79	0.07	0.01	-	-
IKDM1-1	3-2	9.3	35	1.7	11	0.41	1.1	28	-	12	0.52	1.2	-	-	-
IKDM1-1	3-3	14	36	0.54	8.6	0.20	1.4	27	-	11	1.2	0.63	-	-	-
IKDM1-1	3-4	16	34	1.2	9.2	0.08	0.73	29	0.01	9.4	-	0.61	0.01	-	-
IKDM1-1	4-1	3.4	40	1.7	8.0	0.13	0.58	37	-	8.3	-	0.97	-	-	-
IKDM1-1	4-2	4.5	39	1.6	10	0.20	0.65	30	0.65	12	0.29	0.93	0.01	-	-
IKDM1-1	4-3	4.4	40	1.1	10	0.47	0.65	29	0.71	11	1.7	1.0	0.01	-	-
IKDM1-1	4-5	6.7	35	1.8	12	0.25	0.60	27	0.18	14	-	1.8	0.01	-	-

* Contains 0.36 wt% Ba

Most mounds were located along visible fractures reaching the surfaces of quartz crystals. In BSE images, evaporative solute mounds appear lighter than the surrounding quartz matrix due to the presence of heavier elements like Cl, Ca, and K in the mounds (Fig. 2-5). Mounds that were in direct contact with fluorite or that contained fluorite mineral inclusions were not analyzed to avoid creating interferences with the F signal arising from the mounds. As noted above, when possible, evaporative solute mounds were correlated to their source FIAs that had been characterized by microthermometry. Solute mounds observed on the surface of an individual quartz crystal were assumed to have been derived from the FIAs hosted within that quartz crystal. Solute mounds observed on the surface of a quartz crystal that hosted a single FIA were assumed to originate from that FIA. Solute mounds observed on the surface of a quartz crystal that contained multiple FIAs could not be correlated with one another. However, for Hansonburg drusy quartz, most such mounds are likely to have been derived from primary fluid inclusions, as petrography in the present study showed that more than 90% of drusy quartz-hosted fluid inclusions are primary in origin. Most fluid inclusions observed in quartz from the Illinois-Kentucky district exhibited the same associations with primary growth features and similar morphologies to those of the Hansonburg fluid inclusions and were therefore identified as primary. Thus, most evaporative solute mounds generated by decrepitation of Illinois-Kentucky quartz are likely to have come from primary fluid inclusions. However, for Hansonburg drusy quartz, such a test could not be conducted because the major element composition of primary fluid inclusions in Hansonburg stage II and stage III minerals has not been reliably determined in previous studies.

The atomic Na/Cl ratios measured in evaporative solute mounds (Na/Cl$_M$) derived from the standard solutions were consistently higher than the known atomic Na/Cl ratio in the standard solutions themselves (Na/Cl$_F$) (Fig. 2-9). In contrast, the atomic Ca/Cl, K/Cl, and Mg/Cl ratios in the evaporative solute mounds derived from the standard solutions were consistently lower than their respective known values in the

Figure 2-9. Comparison of log atomic ratios of Na, Ca, K, and Mg relative to Cl known in the standard solutions and measured by SEM-EDS in solute mounds derived from the evaporation of droplets of the standard solutions.

standard solutions themselves. From these differences, calibration factors could be calculated to determine the actual Na/Cl, Ca/Cl, K/Cl, and Mg/Cl ratios in the fluid inclusions from the measured ratios in the evaporative solute mounds.

The actual fluid inclusion Na/Cl values thus determined for Hansonburg drusy quartz range from 0.7 to 1.4 with an average value of 0.96 (Fig. 2-10). These Na/Cl ratios are higher than the Na/Cl ratios of 0.6 to 0.9 typical of carbonate-hosted base metal mineralizing fluids (e.g. Hall and Friedman, 1963; Crocetti and Holland, 1989; Viets et al., 1996; Stoffell et al., 2008; Wenz et al., 2012; Pelch et al., 2015). Limited previous fluid inclusion composition data for Hansonburg also show high Na/Cl ratios relative to those typical of carbonate-hosted base metal mineralizing fluids. Putnam (1980) reported

atomic Na/Cl ratios of 0.88 ± 0.14, 2.9 ± 0.7, and 1.3 ± 0.3 determined from bulk leachate analysis of fluid inclusions hosted by galena, fluorite, and late quartz, respectively. In that study, atomic absorption spectroscopy was used to measure the concentrations of cations in the leachates and specific-ion electrodes were used to measure the concentrations of Cl and F. Böhlke and Irwin (1992) reported an atomic Na/Cl ratio of

Figure 2-10. Comparison of log atomic ratios of Na, Ca, K, and Mg relative to Cl in Hansonburg quartz-hosted fluid inclusions as determined in the present study and in previous studies by Putnam (1980) and Böhlke and Irwin (1992).

1.2 ± 0.3 determined from SEM-EDS analyses of evaporative solute mounds derived from fluorite-hosted fluid inclusions. Overall, the fluid inclusion Na/Cl ratios determined in the present study agree closely with the Na/Cl ratios determined in previous studies by Böhlke and Irwin (1992) and Putnam (1980). In contrast, the Ca/Cl, Mg/Cl, and K/Cl values determined in the present study do not agree closely with those from previous studies. Ca/Cl and Mg/Cl values are significantly higher and K/Cl values are significantly lower in the present study than the respective values of these ratios in these previous studies.

Figure 2-11. False color elemental X-ray maps of F, Cl, Na, Ca, and K derived from SEM-EDS analysis of evaporative solute mounds generated by decrepitation of fluid inclusions hosted by quartz from samples HANBL1-1(A-E) and HANBL-SC7-1 (F-J) from the Hansonburg, New Mexico district and sample IKDM1-1(K-O) from the Illinois-Kentucky district. Areas of greater brightness in a map correspond to greater elemental abundance.

Fluorine was detected in all evaporative solute mounds generated by decrepitation of quartz-hosted fluid inclusions from both the Hansonburg and Illinois-Kentucky districts (Fig. 2-11A, F, and K). In every case the F signal was restricted to the mounds and was never detected in the surrounding quartz matrix, indicating that the F signal was not a result of contamination by F from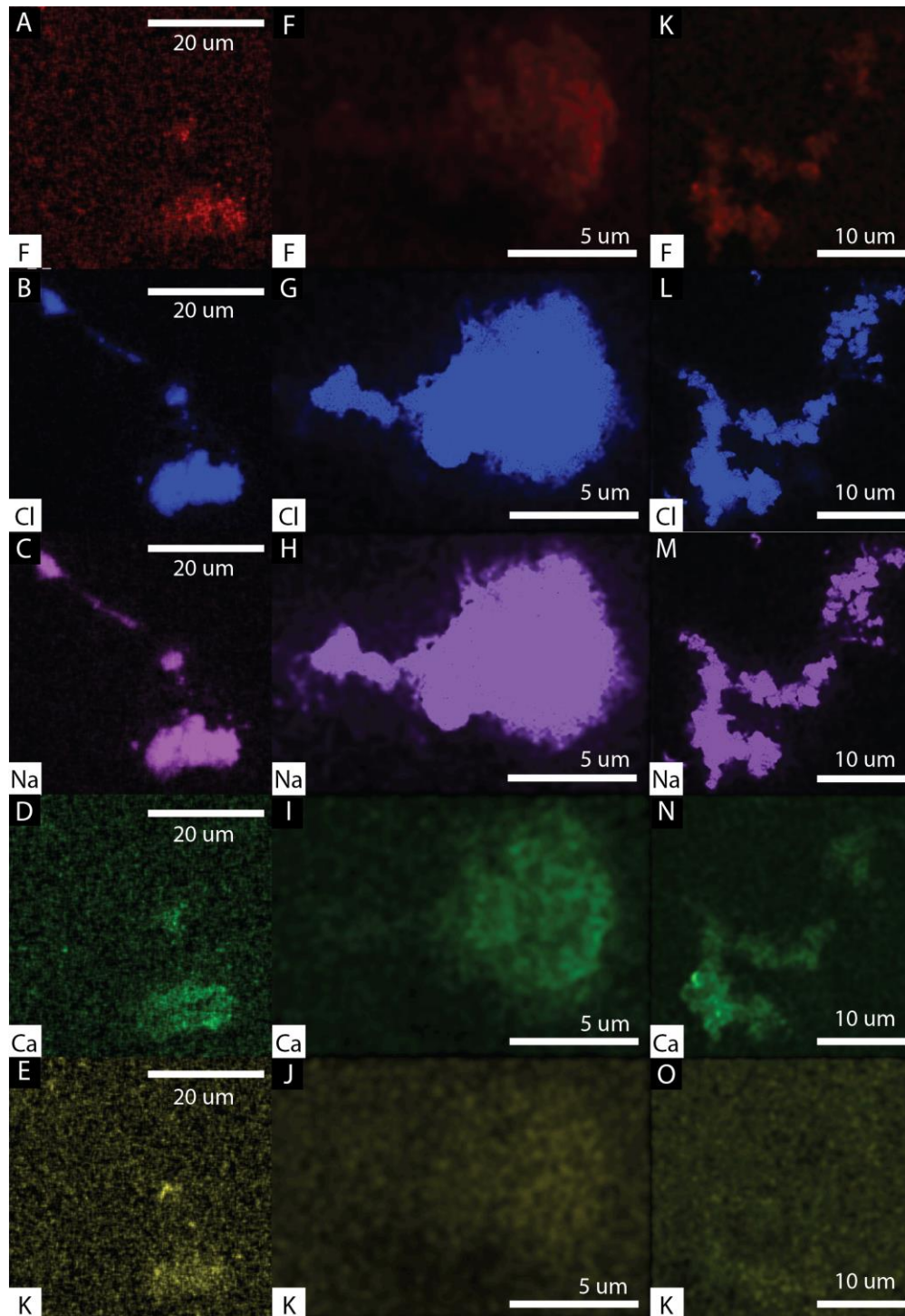 solid solution or a mineral inclusion in the quartz matrix. Instead, the coincident and homogeneous distribution of F in the solute mounds with Na and Cl, known fluid inclusion solutes, suggests that F was also a fluid inclusion solute and did not come from accidental F-mineral inclusions entrained within the fluid inclusions. Another concern regarding the interpretation of the F signals is that they may represent Fe. In SEM-EDS spectra, the Fe Lα peak at 0.71 keV significantly overlaps the F Kα peak at 0.68 keV. However, Fe also has a Kα peak at 6.4 keV, which is missing in all of the spectra generated in the present study. Thus, the peaks near 0.7 keV in these spectra probably genuinely represent F.

Table 2-5. Elemental compositions of evaporative solute mounds derived from fluid inclusions as determined by SEM-EDS analysis.

Sample ID	Mound ID	Fluorine (ppm)	Error (ppm)	
			+	-
Hansonburg, NM fluid inclusions				
HANBL1-1	1-1	583	183	149
HANBL1-1	1-2	1003	303	242
HANBL1-1	2-1A	679	208	168
HANBL1-1	2-1B	671	206	166
HANBL1-1	2-2	1372	409	324
HANBL1-1	2-3	689	207	165
HANBL1-1	2-4	704	211	168
HANBL1-1	2-5	442	136	110
HANBL1-1	3-1	1123	334	264
HANBL1-1	3-2	1775	527	417
HANBL1-1	3-3	2454	727	575
HANBL1-1	5-2	1691	521	502
HANBL1-1	5-3	1682	517	498
HANBL1-1	5-4	864	268	258
HANBL1-1	5-5	2523	775	746
HANBL1-1	5-6	1324	408	394
HANBL1-1	6-1A	1155	353	339
HANBL1-1	6-1B	1881	572	551

| Sample ID	Mound ID	Fluorine (ppm)	Error (ppm)	
			+	-
HANBL1-1	7-1	1248	362	347
HANBL1-1	7-4	417	98	92
HANBL1-1	7-5	599	135	126
HANBL1-1	8-1	717	252	228
HANBL1-1	8-2	641	224	203
HANBL1-1	8-3	709	249	226
HANBL1-1	8-5	1289	454	412
HANBL2-1	1-1	1108	354	291
HANBL2-1	1-2	2133	652	525
HANBL2-1	1-3	1117	342	276
HANBL2-1	2-1	934	290	235
HANBL2-1	2-3	1055	325	263
HANBL2-1	3-1	380	122	100
HANBL2-1	3-3	2480	773	628
HANBL2-2	1-1	1005	380	333
HANBLSC-7-1	1-2	769	251	209
HANBLSC-7-1	1-2B	1487	485	402
HANBLSC-7-1	1-3	1488	495	415
HANBLSC-7-1	2-1	1121	364	302
HANBLSC-7-1	2-2	1406	463	387
HANBLSC-7-1	3-1A	1901	618	513
HANBLSC-7-1	3-1B	1407	467	391
HANBLSC-7-1	3-1C	1779	581	483
HANBLSC-7-1	3-2	1093	358	298
HANBLSC-7-1	3-3	465	155	130
HANBLSC-7-1	4-1	1327	354	295
HANMTSA-12	1-1	1500	552	480
HANMTSA-12	1-3	883	324	282
HANMTSA-12	1-4	1128	414	360
HANMTSA-12	2-6	1247	386	312
HANMTSA-12	2-1	802	249	202
HANMTSA-12	3-1	521	159	127
HANMTSA-12	3-2	774	241	196
HANMTSA-12	3-3	316	99	81
HANRF-15	1-1	1574	425	356
HANRF-15	1-2	956	249	205
Illinois-Kentucky fluid inclusions				
IKDM1-1	2-3	1380	356	291
IKDM1-1	3-2	2636	683	560
IKDM1-1	3-3	944	254	212
IKDM1-1	3-4	2518	655	539
IKDM1-1	4-1	3998	1035	850
IKDM1-1	4-2	2559	663	545
IKDM1-1	4-3	2034	531	437
IKDM1-1	4-5	2455	635	521
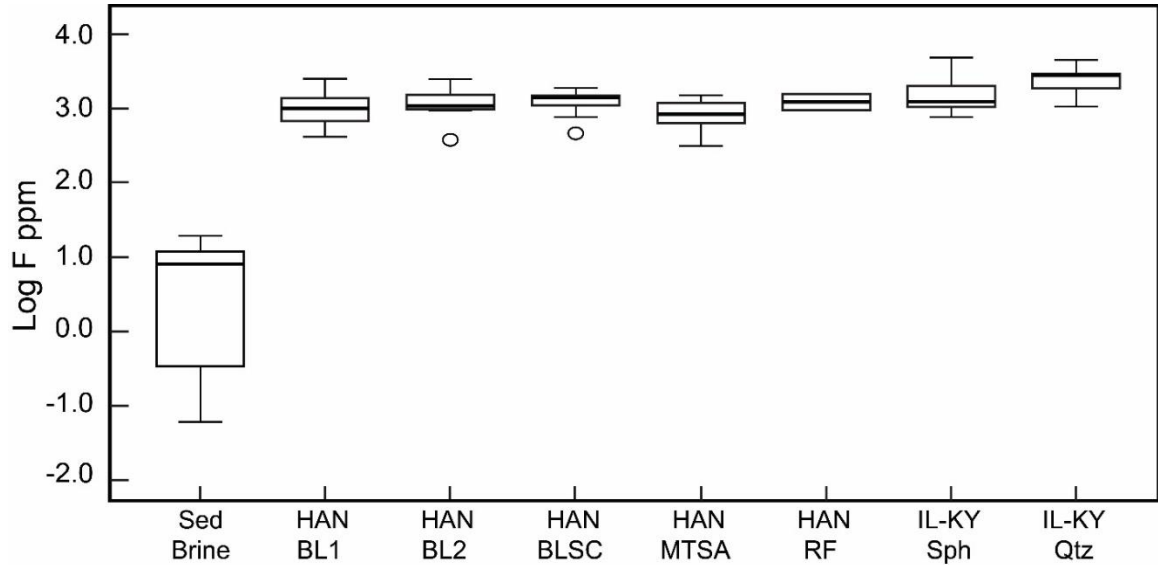
Figure 2-12. Boxplot comparing F concentrations in sedimentary brines (Appold, 2021) to those in quartz-hosted fluid inclusions from the Hansonburg and Illinois-Kentucky districts (this study) and in sphalerite-hosted fluid inclusions from the Illinois-Kentucky district (Kenderes and Appold, 2018).

Calculated F concentrations in fluid inclusions from Hansonburg and Illinois-Kentucky ore-stage quartz range from 320 to 2500 ppm and 940 to 4000 ppm, respectively (Fig. 2-12, Table 2-5). The quartz-hosted fluid inclusion F concentrations found in the present study for Illinois-Kentucky agree well with the sphalerite-hosted fluid inclusion F concentrations of 680 to 4300 ppm for Illinois-Kentucky found by Kenderes and Appold (2017). These results suggest that both the Hansonburg and Illinois-Kentucky ore deposits were formed from anomalously F-rich sedimentary brines.

2.6. Discussion

2.6.1 Uncertainty analysis

Uncertainties in the calculated fluid inclusion F concentrations reported in Table 2-5 were computed via the propagation of errors expression below (Skoog et al., 2007).

$$\sigma_F = C_F \sqrt{\sum_{i=1}^{n} \left(\frac{\sigma_i}{x_i}\right)^2} \tag{2-5}$$

In equation (2-4) σ_F represents one standard deviation absolute uncertainty in fluid inclusion F concentration, C_F is the fluid inclusion F concentration, σ_i is the standard deviation of x in experimental category i, and n is the total number of experimental categories. Three main sources contribute most of the uncertainty in the calculated fluid inclusion F concentrations. The first source is the uncertainty in the F and Cl concentrations measured in the evaporative solute mounds. These uncertainties are calculated from the Phi-Rho-Z data reduction method and express instrument specific uncertainty in the measured F and Cl concentrations from uncertainty caused by interference from adjacent or overlapping peaks from different elements such as F and Na, and heterogeneity in mound topography and composition. The σ_i values thus determined for concentrations measured in the mounds are on the order of 100s to 1000s of ppm F and 1000s of ppm Cl.

The second category of significant uncertainty comes from the regression of the accelerating voltage-specific calibration curves (Eqs. (2-2), (2-3), and (2-4)) used to convert the F/Cl ratios measured in an evaporative solute mound to F/Cl ratios in the source fluid inclusion. The calculated σ_i values in log atomic F/Cl ratios are ±0.065 for the 10 keV curve (Eq. (2-2)), ±0.11 for the 15 keV curve (Eq. (2-3)), and ±0.096 for the 20 keV curve (Eq. (2-4)).

The third major category contributing to the calculated uncertainty in fluid inclusion F concentrations is uncertainty in the Cl concentrations in the original fluid inclusions. The mean Cl concentrations used to calculate F concentrations ranged from 49,000 to 88,000 ppm. The σ_i values for Cl concentrations were calculated using the

standard deviations in salinities of fluid inclusions hosted in individual quartz crystals or chips as appropriate and varied from 740 to 16,000 ppm for the Hansonburg samples and were about 13,000 ppm for the Illinois-Kentucky samples.

2.6.2 *Variability in F concentration*

The calculated mineralizing fluid F concentrations for the five Hansonburg sample locations considered in the present study are similar, with two sites, the south adit at the Mex-Tex mine and stop 1 at the Blanchard mine, having lower mean F concentrations than the other sites. The mean F concentration for the south adit of the Mex-Tex mine is 900 ppm, whereas the mean F concentration for stop 1 is 1100 ppm. The remaining three sample locations--Royal Flush mine and stop 2 and south cut at the Blanchard mine--all had mean F concentrations of 1300 ppm. The drusy quartz analyzed from the south adit of the Mex-Tex mine is likely to be paragenetically late, as it is intergrown with fluorite that is immediately followed by amethyst quartz (Fig. 2-4). This suggests that the F concentration of the Hansonburg mineralizing fluid may have decreased during the later stages of mineralization.

2.6.3 *pH*

An important question regarding the formation of the Hansonburg district is the pH of the mineralizing fluids. As shown by equation (1), mineralizing fluid pH is directly related to HF concentration. If the mineralizing fluid was saturated with respect to fluorite and quartz and had the Ca concentration of 8,400 ppm reported by Putnam et al. (1983), then mineralizing fluid pH as a function of HF concentration can be calculated. Figure 2-13 shows the results of such a calculation performed at temperatures of 140° C and 200° C using the Geochemist's Workbench® software and the

thermo.com.V8.r6+ thermodynamic database (Bethke et al., 2020). The fluid salinity and major element composition used in the calculations were obtained from the fluid inclusion studies of Putnam et al. (1983) and Böhlke and Irwin (1992). For the 320 to 2500 ppm F concentration range found in the present study, the pH of the Hansonburg mineralizing fluid would have been between 1.0 and 2.4 (Fig. 2-13). This range is significantly lower than the pH range of 4.3 to 5.1 predicted for Hansonburg by Putnam et al. (1983) and Norman et al. (1985). However, the pH calculations by Putnam et al. (1983) and Norman et al. (1985) assumed the mineralizing fluid to have been saturated with respect to calcite and did not account for F concentrations on the order of 100s to 1000s of ppm. If the mineralizing fluid truly had the major element composition, CO_2 fugacity, and pH reported by Putnam et al. (1983) and Norman et al. (1985), was saturated with respect to calcite, but had F concentrations of 320 to 2500 ppm, then based on geochemical modeling conducted in the present study, the mineralizing fluid would
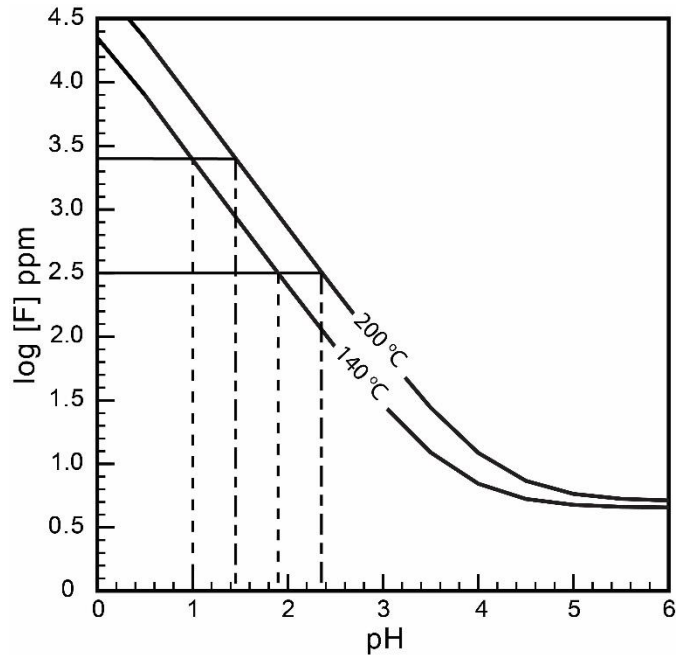
Figure 2-13. Concentration of F (ppm) as a function of pH at 140 and 200 °C and the saturation pressure of water, assuming fluorite saturation in a fluid with the average major element composition of fluid inclusions reported by Putnam et al. (1983) and Böhlke and Irwin (1992). Horizontal black lines represent the maximum and minimum fluid inclusion F concentrations determined in the present study. Vertical dashed lines represent their corresponding pH values at 140 and 200° C.

46

have been supersaturated with respect to fluorite by a factor of 10^5 to 10^6. Conversely, if the mineralizing fluid was otherwise the same but was saturated with respect to fluorite and had the low pH values shown in Figure 2-13, then the fluid would have been significantly undersaturated with respect to calcite.

The question then arises as to what evidence exists to indicate the saturation state of the mineralizing fluid with respect to calcite. Putnam et al. (1983) and Norman et al. (1985) argued that the absence of limestone dissolution features associated with mainstage hydrothermal mineral deposition, especially the limited replacement of limestone with fluorite, barite, and sulfide minerals indicate that the mineralizing fluid was in equilibrium with calcite. However, the host rock in the Hansonburg district underwent pervasive silicification early in the paragenetic sequence prior to fluorite precipitation (Roedder et al., 1968; Putnam et al., 1983). This silicification is most intense near the ore bodies and in brecciated limestone, where it extends along faults and fractures (Kottlowski, 1953, Norman et al. 1985; Kottlowski and Steensma, 1979). Lasky (1932) suggested that the silicification may have served as a seal that prevented replacement of the limestone by hydrothermal minerals. This is supported by numerical reactive transport modeling by Smith and Appold (2019) for the Illinois-Kentucky district, which shows that silicified faults can effectively transmit HF-rich acidic fluids through hundreds of meters of limestone while preventing reactions between the fluids and surrounding unaltered limestone. In Hansonburg, the idea that mineralizing fluids were transmitted from Precambrian crystalline basement rocks through a sedimentary thickness of less than 200 m via faults and fractures before entering the Council Springs member (Kottlowski, 1953; Putnam, 1980) is supported by hydrogeologic modeling of

regional paleoflow near the Hansonburg district (Mailloux et al. 1999) and the strong

association of ore bodies with faults and fractures. Early silicification of faults traversing

the sedimentary carbonates would have prevented the neutralization of the mineralizing

fluid by dissolution of limestone and thus explains the absence of extensive limestone

dissolution features linked to ore formation such as those observed in the Illinois-

Kentucky district (Kenderes and Appold, 2017). Therefore, the absence of field evidence

for extensive ore-stage limestone dissolution features does not necessarily mean that the

mineralizing fluid was saturated with respect to calcite.

The low mineralizing fluid pH of 1 to 2.4 predicted for the Hansonburg district

has implications for the precipitation of metal sulfide minerals like the implications

reported by Kenderes and Appold (2017) for the Illinois-Kentucky district. Like Illinois-

Kentucky, Hansonburg is enriched in fluorite and barite relative to metal sulfide minerals

whereas most carbonate-hosted base metal deposits around the world are metal sulfide

mineral dominant and are thought to have precipitated from fluids with pH values

between 4 and 5.5 (Sverjensky, 1984). The solubilities of metal sulfide minerals like

galena and sphalerite, typically the most abundant metal sulfide minerals in carbonate-

hosted base metal deposits, are highly sensitive to pH (Fig. 2-14). The solubility of

barite, one of the most abundant ore minerals in the Hansonburg district, is also sensitive

to pH at values of less than about 3 at the ore-forming temperatures in the district. To

quantify the effect of pH on the solubilities of sphalerite, galena, and barite, a suite of

calculations was completed using Geochemist's Workbench®. The model fluid used for

these calculations had the same salinity and major element composition as fluid used in

the fluorite solubility calculation (Fig. 2-14). In addition, the model fluid had a constant total S concentration of 100 ppm based on a mineralizing fluid H_2S concentration of approximately 50 ppm reported by Putnam et al. (1983) and the assumption of equimolar H_2S and SO_4 in the fluid. Oxygen fugacity (f_{O_2}) was set to vary as a function of temperature and pH such that the molar concentrations of sulfide and sulfate in the fluid remained equal. This condition was chosen based on the abundance of both barite and galena in the ore mineral assemblage and their overlap in the paragenetic sequence, suggesting that the f_{O_2} of the fluid was in a range that allowed sulfate and sulfide to coexist in significant concentrations.
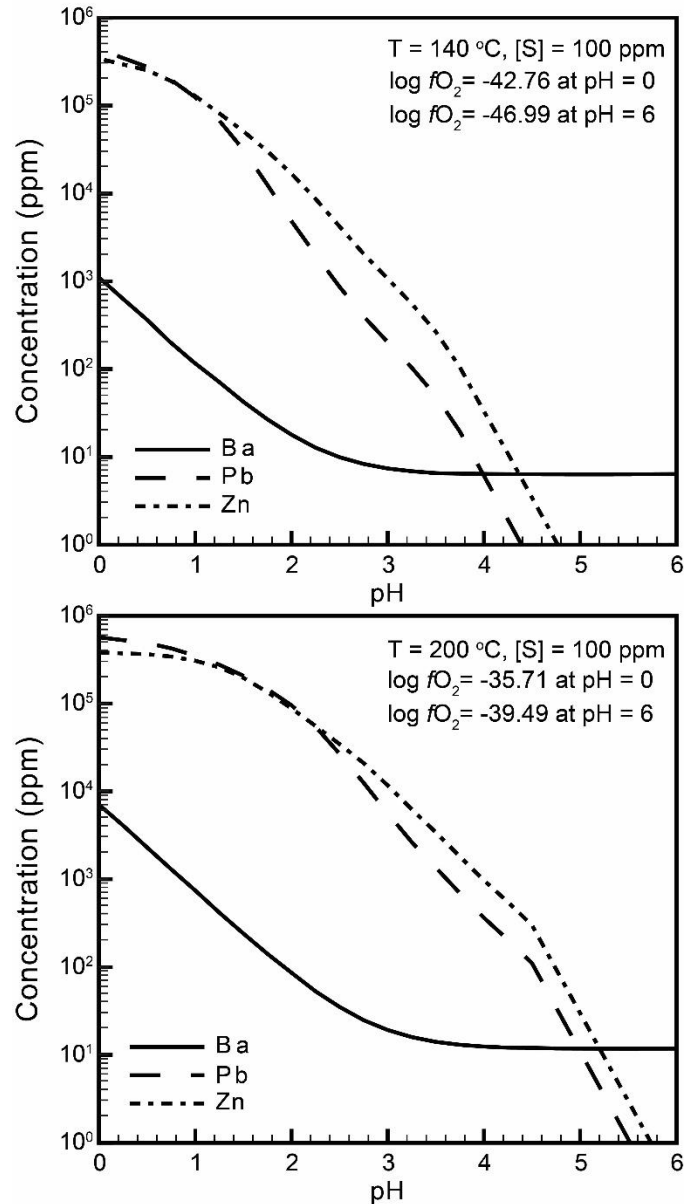
Figure 2-14. Concentration of Ba, Pb, and Zn (ppm) as a function of pH at 140 and 200° C and the saturation pressure of water assuming barite, galena, and sphalerite saturation respectively in a fluid with the 100 ppm S and average major element composition of fluid inclusions reported by Putnam et al. (1983) and Böhlke and Irwin (1992). Oxygen fugacity was allowed to vary as a function of pH and temperature such that in molar concentration $[H_2S] = [HSO_4^-] + [H_2SO_4]$.

49

The geochemical calculations indicate that a decline in mineralizing fluid pH from 4.5 to 1.5 increases the solubility of sphalerite and galena by 4.2 and 4.7 orders of magnitude, respectively at 140° C, and by 2.8 and 3.3 orders of magnitude, respectively at 200° C. The high solubility of metal-sulfide minerals at low pH would have inhibited their precipitation during fluorite precipitation unless the metal and sulfide concentrations of the mineralizing fluid were very high. Barite precipitation is also suppressed between pH values of 4.5 and 1.5, with solubility increases of 1.1 orders of magnitude at 140° C and 1.3 at 200° C. These increases in solubility are significantly lower than those of sphalerite and galena, meaning that the suppression of barite precipitation would also be lower. Thus, the low pH of the Hansonburg mineralizing fluid may have suppressed the precipitation of metal sulfide minerals without correspondingly suppressing the precipitation of barite nearly as much, especially during fluorite precipitation, resulting in the fluorite-barite dominant ore mineral assemblage observed in the district.

2.6.4 Implications for mineralizing fluid origin

The source of F in the Hansonburg district and other similar carbonate-hosted base metal-F-Ba deposits associated with the Rio Grande rift has been a topic of considerable discussion. McLemore et al. (1998) proposed that F could have been leached from Proterozoic granitic basement rocks. However, modern geothermal fluids in the southern Rio Grande rift that apparently have had contact with such rocks have F concentrations of only up to about 15 ppm (Witcher, 1995). Further, groundwater elsewhere around the world that has equilibrated with granitic rocks has maximum F concentrations of only a few 10s of ppm (White et al., 1963; Chae et al., 2007; Mondel et al., 2009; Brindha et al., 2011). These concentrations are orders of magnitude lower than

the 100s to 1000s of ppm F found in the present study. In addition, the pH of modern

groundwater in the area of the Hansonburg district ranges from 5 to 11 (Witcher, 1995;

Williams et al., 2013), well above the mineralizing fluid pH values of 1 to 2.4 predicted

in the present study. A lower pH at the time of main-stage hydrothermal mineralization

would have allowed greater amounts of F to be leached from the basement rocks. Lueth

et al. (2005) have proposed that the Hansonburg mineralizing fluid was acidified during

hydrothermal jarosite precipitation by oxidation of H_2S to SO_4^{2-}, but this process requires

high oxygen fugacity, limiting it to shallow depths.

The most widely hypothesized source of F in the Hansonburg mineralizing fluid is

F-rich fluid exsolved from alkaline magmas during the later stages of formation of the

Rio Grande rift (Worl, 1974; Van Alstine, 1976; McLemore et al. 1998; Lueth et al.,

2005; Partey et al., 2009). To determine whether the fluids exsolved from Rio Grande

rift magmas could have been rich enough in F to account for the high F concentration in

the Hansonburg mineralizing fluid, the experimental F partitioning relationship of Seifert

et al. (2000) was used to calculate the HF/H_2O fugacity (*f*) ratio of the magmatic fluid

based on the F/OH mole fraction (*X*) ratio in apatite.

$$\log \left(\frac{f_{HF}}{f_{H_2O}} \right)^{Fluid} = \log \left(\frac{X_F}{X_{OH}} \right)^{Ap} - 1.523 - 3200/T \qquad (2\text{-}6)$$

The closest Rio Grande rift rocks to the Hansonburg district for which apatite

composition data were found are from the Spanish Peaks area in south-central Colorado

(Lord et al., 2016). The F concentration in apatite in these rocks ranged from 1.33 to 2.93

weight percent, equating to a magmatic fluid HF/H_2O fugacity ratio range of 9.6×10^{-5} to

1.0×10^{-3} when calculated over a temperature range of 900 to 1200° C, respectively (Fig.

2-15). If the HF/H_2O fugacity ratio of the magmatic fluid remained constant as the fluid

ascended and cooled, then according to speciation calculations performed with the Geochemist Workbench® software, the F concentration in the magmatic fluid would have ranged between 300 and 6,000 ppm at the mineralization temperatures of 140 to 200° C.. In these speciation calculations, the major element (Na, Mg, Cl, Ca, Cl) concentrations were derived from Yardley (2005) and a salinity of 10 wt. % NaCl equivalent, a pH of 1, and saturation with respect to quartz in the model magmatic fluid were assumed. More generally, apatite in mafic and ultramafic

Figure 2-15. Calculated HF/H_2O fugacities in magmatic fluids in equilibrium with apatites from basalts calculated at temperatures from 900 to 1200° C. Closed symbols represent the minimum, maximum, and median values at each temperature for Rio Grande rift apatites (n = 7, Lord et al., 2016). Open symbols represent the minimum, maximum, and median values for apatites from representative mafic to ultramafic igneous rocks (n = 603, Seifert et al. 2000; Meurer and Natland, 2001; Boureau et al. 2007; Orejana et al., 2008; Engvik et al. 2009; Zhang et al., 2012; Parat et al., 2011; Larrea et al., 2014; Choi et al., 2020)

igneous rocks may have F concentrations ranging from negligible to over 4 weight percent (e.g. Seifert et al. 2000; Meurer and Natland, (2001); Boudreau et al. 2007; Orejana et al., 2008; Engvik et al. 2009; Zhang et al., 2012; Parat et al., 2011; Cucciniello et al., 2017; Choi et al., 2020). For apatite crystals containing measurable quantities of both F and OH, this equates to magmatic fluid HF/H_2O fugacity ratios up to 7.5×10^{-5}
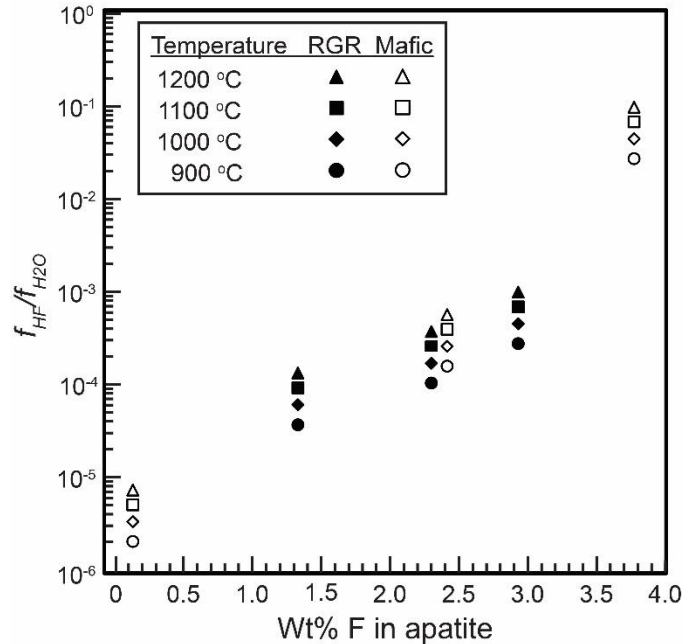
and corresponding F concentrations of hundreds of thousands of ppm in the magmatic

fluid if the fluid maintained a constant HF/H_2O fugacity ratio as it ascended and cooled to

140 to 200° C.

A further consideration is how much magmatic fluid mixed with sedimentary

brine to form the resultant mineralizing fluid mixture and whether those mixing

proportions could account for the high F concentration in the resultant mineralizing fluid

mixture. Partey et al. (2009) plotted Br/Cl ratios vs. $\delta^{37}Cl$ values measured in fluorite

hosted fluid inclusions to estimate the relative contributions of asthenosphere-derived and

evaporite-derived Cl to the total mineralizing fluid Cl. Partey et al. (2009) estimated the

asthenospheric Cl component in the Hansonburg mineralizing fluid to have varied

significantly from minor to a maximum of 49% of the total Cl in the mineralizing fluid.

If the relative proportions of Cl derived from asthenospheric and sedimentary sources

accurately represent the proportions of magmatic fluid and sedimentary brine that mixed

to form the mineralizing fluid, then a magmatic fluid containing up to 6,000 ppm F could

account for the mineralizing fluid F concentrations found in the present study.

Figure 2-16 shows a conceptual model for hydrothermal mineralization in the

Hansonburg district based on modeling of groundwater flow in the Rio Grande rift basin

in the vicinity of the Hansonburg district over the last 28 million years by Mailloux et al.

(1999) in conjunction with geological information from Clemons (1996) cited by Lueth et

al. (2005). This conceptual model resembles the conceptual model widely hypothesized

for the Illinois-Kentucky district (e.g. Plumlee et al., 1995; Kenderes and Appold, 2017,

and references therein). In the Hansonburg model, meteoric water migrated downward
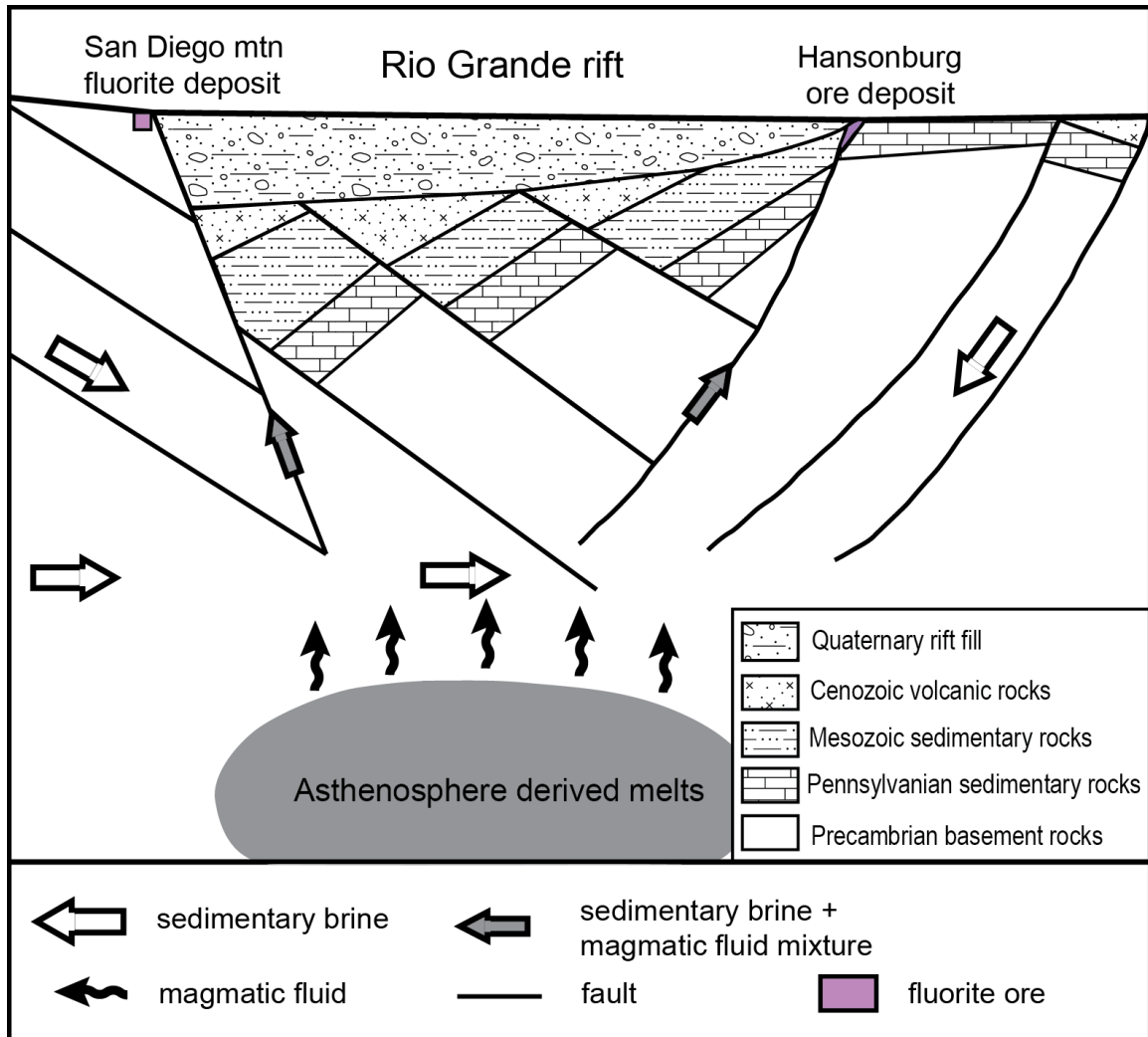
Figure 2-16. Conceptual fluorite genesis model for the Hansonburg district after Lueth et al. (2005) and Partey et al. (2009), in which F-rich, acidic magmatic fluids mix with sedimentary brines at depth, and the resulting ore fluid mixture rises along faults and cools, precipitating galena and barite early on followed by fluorite and barite.

into the rift basin, through the sedimentary units, then penetrated the fractured crystalline basement rocks to a depth of 2.8 km below the sedimentary overburden, driven predominantly by gradients in topography (Mailloux et al., 1999). The water then migrated through the basement rocks before discharging toward the eastern edge of the Rio Grande rift. As the meteoric water migrated, it evolved into a sedimentary brine and an ore fluid by acquiring elements like Na, Cl, Ca, Ba, S, and Pb through interactions

with sedimentary and basement source rocks such as the Permian evaporites and Precambrian granites in the region. A fluorine rich magmatic fluid exsolved from mafic to ultramafic magmas derived from the asthenospheric mantle then mixed to varying degrees with the sedimentary brine at depth. The resulting hot, fluorine rich, acidic fluid mixture then rose along silicified faults, precipitating galena, barite, and fluorite in open spaces in and adjacent to the faults. The abundance of limestone in the -host rock suggests the possibility that pH neutralization by dissolution of limestone caused precipitation of the main-stage hydrothermal minerals. However, as discussed above, the Hansonburg district does not show evidence for large-scale limestone dissolution and the limestone that is associated with the ore bodies is highly silicified, making the limestone resistant to dissolution. Thus, pH neutralization through dissolution of limestone seems unlikely to have been the main ore precipitation mechanism.

A more likely fluorite precipitation mechanism for Hansonburg is cooling. Figure 2-13 shows that at the pH values predicted in the present study, cooling could be an efficient precipitation mechanism for fluorite. For example, at a pH less than about 3.5, a drop in temperature from 200 to 140° C results in a decline of about 0.5 order of magnitude in the solubility of fluorite.

Determination of the precipitation mechanism of the other two major ore minerals, barite and galena, is complicated by the question of the oxidation state of sulfur in the mineralizing fluid. Figure 2-17 shows the predominance fields of the sulfur species, H_2S, HSO_4^-, and SO_4^{2-}, as a function of temperature, oxygen fugacity, and pH. Earlier studies of the Hansonburg district estimated $\log f_{O_2}$ values of about -36 to -39 for a 200° C mineralizing fluid (shaded box in Fig. 2-17) early in the paragenesis during

galena precipitation, and about -41 to -44 at 150° C (stippled box in Fig. 2-17) during main stage fluorite and barite precipitation (Putnam et al., 1983; Norman et al., 1985). Each of these log f_{O_2} ranges straddles the boundary between the HSO_4^- and H_2S species predominance fields at their respective temperatures of 200 and 150° C. This suggests that as the mineralizing fluid cooled, the sulfate/sulfide activity ratio likely remained relatively constant and
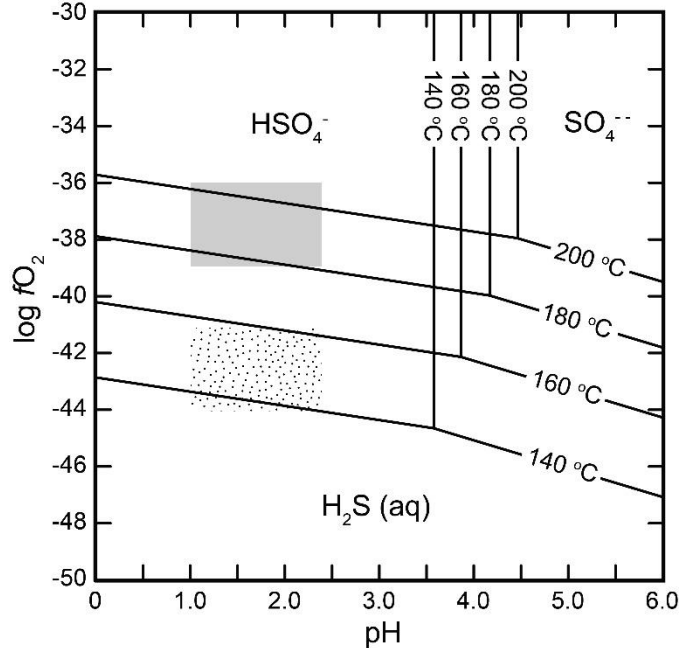

Figure 2-17. Stability fields for sulfur species in ore fluid as a function of log f_{O_2} and pH calculated from 140 to 200 °C using Geochemist Workbench® software. Boxes shows range of log f_{O_2} values at 200°C (shaded) and 150 °C (stippled) predicted by Putnam et al. (1983) and Norman et al. (1985) over the range of pH values predicted for ore stage fluids in this

near unity. However, further small perturbations to the log f_{O_2} may have been enough to make the mineralizing fluid relatively either more sulfide or sulfate rich, thus promoting the precipitation of either galena or barite, respectively.

2.7 Conclusions

Analyses of evaporative solute mounds formed by thermal decrepitation of quartz-hosted fluid inclusions from the Hansonburg and Illinois-Kentucky districts were performed using SEM-EDS. The fluid inclusions from both districts were found to have F concentrations on the order of 100s to 1000s of ppm. Because the Hansonburg fluid inclusions analyzed in this study were in samples of drusy quartz from throughout the

56

fluorite paragenetic sequence, this indicates that Hansonburg mineralizing fluid was F-rich throughout the time of fluorite precipitation. The Illinois-Kentucky fluid inclusions analyzed in this study are from a narrower interval of the paragenetic sequence when quartz, fluorite, and sulfide mineral precipitation coincided. These results corroborate those of Kenderes and Appold (2017) who found sphalerite-hosted fluid inclusions in the Illinois-Kentucky district to be similarly F-rich. The F concentrations found in both the Hansonburg and Illinois-Kentucky fluid inclusions are orders of magnitude higher than the tenths to 10s of ppm F typical of sedimentary brines.

The high F concentrations found in Hansonburg fluid inclusions indicate that the Hansonburg mineralizing fluid had a pH in the range of 1 to 2.4 during fluorite mineralization, much lower than the pH range of 4.3 to 5.1 predicted for the district in earlier studies and also much lower than the typical pH range of 4 to 5.5 considered typical of carbonate-hosted base metal mineralizing fluids. High F concentrations would have promoted fluorite precipitation while the corresponding low pH would have suppressed metal sulfide mineral precipitation without significantly suppressing barite precipitation, resulting in fluorite-barite-rich, metal-sulfide mineral-poor mineral assemblage observed in the district.

The high F concentrations found in Hansonburg fluid inclusions in this study support a genetic model in which F-rich magmatic fluids mixed with resident sedimentary brines to form the mineralizing fluid. Mineral-water partitioning theory estimates of the F concentrations in this magmatic fluid based on the composition of apatite from Rio Grande rift basalt indicate that such a magmatic fluid could have

contained up to hundreds of thousands of ppm F, sufficient to account for the ore-fluid F

concentrations measured in this study.

2.8 References

Ames, L. L., 1958. Chemical analyses of the fluid inclusions in a group of New Mexico minerals. *Econ. Geol.* **53**, 473-480.

Appold, M. S., 2021. Applications of fluid inclusions to studies of sediment-hosted base metal ore deposits: case studies from the central U.S.A. and Brazil. In *Mineral. Assoc. Can. Short Course*, **49**, 47–72.

Bethke, C., Farrell, B., and Yeakel, S., 2020. Geochemist's Workbench ® : Release 12: GWB Reference Manual. RockWare Incorporated.

Bodnar, R. J., 1993. Revised equation and table for determining the freezing point depression of H2O-NaCl solutions. *Geochim. Cosmochim. Acta*, **57**, 683-684.

Böhlke, J. K., and Irwin, J. J., 1992. Brine history indicated by argon, krypton, chlorine, bromine, and iodine analyses of fluid inclusions from the Mississippi Valley type lead-fluorite-barite deposits at Hansonburg, New Mexico. *Earth Planet. Sci.Lett.* **110**, 51-66.

Boudreau, A. E., Simon, A. C., 2007. Crystallization and degassing in the basement sill, McMurdo dry valleys, *Antarct. J. Petrol.* **48**, 1369-1386

Brindha, K., Rajesh, R., Murugan, R., and Elango, L., 2011. Fluoride contamination in groundwater in parts of Nalgonda District, Andhra Pradesh, India. *Environ. Monit. Assess.* **172**, 481-492.

Chae, G.T., Yun, S.T., Mayer, B., Kim, K.H., Kim, S.Y., Kwon, J.S., Kim, K. and Koh, Y.K., 2007. Fluorine geochemistry in bedrock groundwater of South Korea. *Sci. Total Environ.* **385**, 272-283.

Chapin, C. E., 1979. Evolution of the Rio Grande rift–A summary. *Rio Grande rift: tectonics and magmatism*, Washington D.C., American Geophysical Union **14**, 1-6.

Choi, E., Fiorentini, M. L., Giuliani, A., Foley, S. F., Maas, R., and Taylor, W. R., 2020. Subduction-related petrogenesis of Late Archean calc-alkaline lamprophyres in the Yilgarn Craton (Western Australia). *Precambr. Res.*, **338**, 105550.

Crocetti, C. A., and Holland, H. D., 1989. Sulfur-lead isotope systematics and the composition of fluid-inclusions in galena from the Viburnum Trend, Missouri. *Econ. Geol.* **84**, 2196-2216.

Cucciniello, C., Melluso, L., le Roex, A. P., Jourdan, F., Morra, V., de'Gennaro, R., and Grifa, C., 2017. From olivine nephelinite, basanite and basalt to peralkaline trachyphonolite and comendite in the Ankaratra volcanic complex, Madagascar: 40Ar/39Ar ages, phase compositions and bulk-rock geochemical and isotopic evolution. *Lithos* **274**, 363-382.

Denny F. B., Devera J. A., and Kittler A., 2013. *Bedrock geology of Saline Mines Quadrangle, Gallatin and Hardin Counties, Illinois* (eds. F. B. Denny, J. A. Devera, and A. Kittler). Illinois Geol. Quadrang. Map, 1–10.

Engvik, A. K., Golla-Schindler, U., Berndt, J., Austrheim, H., and Putnis, A., 2009. Intragranular replacement of chlorapatite by hydroxy-fluor-apatite during metasomatism. *Lithos*, **112**, 236-246.

Hall W. E. and Friedman I., 1963. Composition of fluid inclusions, Cave-in-Rock fluorite district, Illinois, and Upper Mississippi Valley zinc-lead district. *Econ. Geol.* **58**, 886–911

Kenderes, S. M., and Appold, M. S., 2017. Fluorine concentrations of ore fluids in the Illinois-Kentucky district: Evidence from SEM-EDS analysis of fluid inclusion decrepitates. *Geochim. Cosmochim. Acta*, **210**, 132-151.

Kendrick M. A., Burgess R., Leach D., and Pattrick R. A. D., 2002. Hydrothermal fluid origins in Mississippi Valley-type ore districts: Combined noble gas (He, Ar, Kr) and halogen (Cl, Br, I) analysis of fluid inclusions from the Illinois-Kentucky fluorspar district, Viburnum Trend, and Tri-State districts, midcontinent. *Econ. Geol.* **97**, 453–469.

Kopicki, R. J., 1962. *Geology and ore deposits of the northern part of the Hansonburg district, Bingham, New Mexico*. [Master's Thesis]: New Mexico Institute of Mining and Technology.

Kottlowski, F. E., 1953. Geology and ore deposits of a part of the Hansonburg Mining District Socorro County, New Mexico. *New Mex. Bur. Mines Min. Resour. Circ*. **23**, 1-9.

Kottlowski, F. E., and Steensma, R. S., 1979. Barite-fluorite-lead mines of Hansonburg mining district in central New Mexico. *New Mex. Geol.* **1**, 17-20.

Lasky, S. G., 1932. The ore deposits of Socorro County, New Mexico. *New Mex. Bur. Mines Min. Resour Bull.* **8**, 63-71

Lord, A. B. H., McGregor, H., Roden, M. F., Salters, V. J., Sarafian, A., and Leahy, R., 2016. Petrogenesis of coeval sodic and potassic alkaline magmas at Spanish Peaks, Colorado: Magmatism related to the opening of the Rio Grande rift. *Geochim. Cosmochim. Acta* **185**, 453-476.

Lueth, V.W., Rye, R.O., and Peters, L., 2005. "Sour gas" hydrothermal jarosite: ancient to modern acid-sulfate mineralization in the southern Rio Grande Rift. *Chem. Geol.* **215**, 339-360.

Mailloux, B. J., Person, M., Kelley, S., Dunbar, N., Cather, S., Strayer, L., and Hudleston, P., 1999. Tectonic controls on the hydrogeology of the Rio Grande Rift, New Mexico. *Water resources research*, **35**, 2641-2659.

McLemore, V. T., Giordano, T. H., Lueth, V.W., and Witcher, J. C., 1998. Origin of barite–fluorite–galena deposits in the southern Rio Grande rift, New Mexico. *Guideb. NM Geol. Soc*. **49**, 251-263.

Meurer, W. P., and Natland, J. H., 2001. Apatite compositions from oceanic cumulates with implications for the evolution of mid-ocean ridge magmatic systems. *J. Volcano. Geotherm. Res.* **110**, 281-298.

Mondal, N. C., Prasad, R. K., Saxena, V. K., Singh, Y., and Singh, V. S., 2009. Appraisal of highly fluoride zones in groundwater of Kurmapalli watershed, Nalgonda district, Andhra Pradesh (India). *Environ. Earth Sci.* **59**, 63-73.

Norman, D.I., Ting, W., Putnam, B.R. and Smith, R.W., 1985. Mineralization of the Hansonburg Mississippi-Valley type deposit, New Mexico: Insight from composition of gases in fluid inclusions. *Can. Mineral.* **23**, 353-368.

Orejana, D., Villaseca, C., Billström, K., and Paterson, B. A., 2008. Petrogenesis of Permian alkaline lamprophyres and diabases from the Spanish Central System and their geodynamic context within western Europe. *Contrib. Mineral. Petrol.* **156**, 477-500.

Parat, F., Holtz, F., and Klügel, A., 2011. S-rich apatite-hosted glass inclusions in xenoliths from La Palma: constraints on the volatile partitioning in evolved alkaline magmas. *Contrib. Mineral. Petrol.* **162**, 463-478.

Partey, F., Lev, S., Casey, R., Widom, E., Lueth, V.W. and Rakovan, J., 2009. Source of fluorine and petrogenesis of the Rio Grande rift-type barite-fluorite-galena deposits. *Econ. Geol.* **104**, 505-520.

Pelch, M. A., Appold, M. S., Emsbo, P., and Bodnar, R. J., 2015. Constraints from fluid inclusion compositions on the origin of Mississippi Valley-type mineralization in the Illinois-Kentucky district. *Econ. Geol.* **110**, 787-808.

Plumlee G. S., Goldhaber M. B. and Rowan E. L., 1995. The potential role of magmatic gases in the genesis of Illinois-Kentucky fluorspar deposits; implications from chemical reaction path modeling. *Econ. Geol.* **90**, 999–1011

Putnam, B. R., 1980. *Fluid inclusion and microchemical analysis of the Hansonburg Mississippi Valley–Type ore deposits in central New Mexico.* [Master's Thesis–Unpubl]: New Mexico Institute of Mining and Technology.

Putnam, B. R., Norman, D. I., and Smith, R. W., 1983. Mississippi Valley-type lead-fluorite-barite deposits of the Hansonburg mining district. In *Guideb. NM Geol. Soc., 34th Field Conference,* 253-259. New Mexico Geological Society.

Roedder E., Heyl, A. V., and Creel, J. P., 1968. Environment of Ore Deposition at the Mex-Tex Deposits, Hansonburg District, New Mexico, from studies of fluid inclusions. *Econ. Geol.* **63**, 336–348.

Seager, W.R., Shafiqullah, M., Hawley, J.W. and Marvin, R., 1984. New K-Ar dates from basalts and the evolution of the southern Rio Grande rift. *Geol. Soc. Am. – Bull.*, **95**, 87-99.

Seifert, W., Kämpf, H., and Wasternack, J., 2000. Compositional variation in apatite, phlogopite and other accessory minerals of the ultramafic Delitzsch complex, Germany: implication for cooling history of carbonatites. *Lithos*, **53**, 81-100.

Skoog, D. A., Holler, F. J., and Crouch, S. R., 2017. *Principles of instrumental analysis 7th ed.* Cengage learning.

Smith, S. E., Appold, M. S., 2019. Reactive transport modeling of ore formation in the Illinois-Kentucky fluorite district by mixing of magmatic, acidic, F-rich fluid with sedimentary brine. *Abstr. with Programs - Geol. Soc. Am.,* **51**

Stoffell, B., Appold, M. S., Wilkinson, J. J., McClean, N. A., Jeffries, T. E., 2008. Geochemistry and evolution of Mississippi Valley-type mineralizing brines from the Tri-State and Northern Arkansas districts determined by LA-ICP-MS microanalysis of fluid inclusions. *Econ. Geol.*, **103**, 1411-1435.

Sverjensky, D. A., 1984. Oil field brines as ore-forming solutions. *Econ. Geol.*, **79**, 23-37.

Van Alstine, R. E., 1976. Continental rifts and lineaments associated with major fluorspar districts. *Econ. Geol.* **71**, 977-987.

Viets, J. G., Hofstra, A. H., and Emsbo, P., 1996. Solute compositions of fluid inclusions in sphalerite from North American and European Mississippi Valley-type ore deposits: Ore fluids derived from evaporated seawater. *Soc. Econ. Geol. Spec. Pub.*, **4**, 465-482.

Wenz, Z. J., Appold, M. S., Shelton, K. L., and Tesfaye, S., 2012. Geochemistry of Mississippi Valley–type mineralizing fluids of the Ozark Plateau: A regional synthesis. *Am. J. Sci.* **312**, 22-80.

Witcher, J. C. 1995. A geothermal resource database: New Mexico. Southwest Technology Development Institute, New Mexico State University.

White, D.E., Hem, J.D. and Waring, G.S., 1963. *Chemical composition of subsurface waters*. No. 440-F.

Williams, F. E., Fillo, P. V., and Bloom, P. A., 1964. *Barite deposits of New Mexico*. State Bureau of Mines and Mineral Resources, New Mexico Institute of Mining and Technology.

Wilpolt, R. H., and Wanek, A. A., 1951. Geology of the region from Socorro and San Antonio east to Chupadera Mesa. *Socorro County, New Mexico: USGS, Oil and Gas Investigations Map OM-121, scale*, *1*(63), 360.

Worl, R.G., 1974. Geology of fluorspar deposits of the western United States. In *A symposium on the geology of fluorspar: KY Geol. Surv. Spec. Pub*, **22**, 31-54.

Yardley, B.W., 2005. 100th Anniversary Special Paper: metal concentrations in crustal fluids and their relationship to ore formation. *Econ. Geol.* **100**, 613-632.

Zappettini, E. O., Rubinstein, N., Crosta, S., and Segal, S. J., 2017. Intracontinental rift-related deposits: A review of key models. *Ore Geol. Rev.*, **89**, 594-608.

Zhang, C., Holtz, F., Ma, C., Wolff, P. E., and Li, X., 2012. Tracing the evolution and distribution of F and Cl in plutonic systems from volatile-bearing minerals: a case study from the Liujiawa pluton (Dabie orogen, China). *Contrib. Mineral. Petrol.,* **164**, 859-879.

Chapter 3: Reactive transport modeling of ore formation in the Illinois-Kentucky fluorite district by mixing of an acidic, F-rich fluid with resident sedimentary brines

3.1 Abstract

The fluorite dominant Illinois-Kentucky Mississippi Valley-type (MVT) district is the largest occurrence of fluorite in the U.S. and is atypical of MVT mineralization, which is typically dominated by sphalerite, galena, and/or barite. A long-standing hypothesis regarding ore formation in the llinois-Kentucky district is that the ore fluids were enriched in F that was introduced by magmatic fluids exsolved at depth from Permian ultramafic magmas that mixed with a resident sedimentary brine. The F-rich fluid mixture was likely further transmitted from depth along faults and fractures until intersecting permeable limestone layers, where ore precipitation occurred due to reaction with limestone or mixing with other resident brine. Recent fluid inclusion studies of the Illinois-Kentucky district suggest that the ore fluid had a F concentration between 680 and 4300 ppm, a range that would require a pH between 0 and 1.4, significantly lower than the pH range of 4 to 5.5 typical of MVT ore fluids.

The present study was undertaken to investigate the implications of such an acidic, F-rich fluid for water rock interactions and ore formation via reactive transport modeling. The models indicate that an acidic, F-rich fault fluid can ascend a silicified fault through 100's of meters of limestone without becoming neutralized. Although some of the fluid ascending the fault migrates into the adjacent limestone at greater depths, most of the fluid exits the fault where it intersects the permeable Ste. Genevieve Limestone aquifer, a major ore host formation. Upon exiting the fault, the fluid reacts

with the limestone and is neutralized within a few meters. Intense limestone dissolution

with a corresponding increase in porosity to more than 55% after 2000 years is localized

to the intersection of the fault with the Ste. Genevieve Limestone. The models indicate

that the neutralization of acidic, F-rich fluid is a very efficient fluorite precipitation

mechanism that produces a fluorite dominant ore assemblage like that observed in

Illinois-Kentucky. High-grade fluorite precipitation is also limited to the vicinity of the

fault, reaching up to 20% by volume in the permeable layers and up to 5% in the

underlying limestone layers after 2,000 years. These results are generally consistent with

field observations. In contrast, under otherwise identical hydrogeologic conditions,

models in which the fault fluid had much lower F concentration of only 4 ppm and a pH

of 4 that is more typical of MVT fluids were found to require several orders of

magnitude more time to produce ore grades and tonnages observed in the field, and also

not to produce a fluorite dominant mineral assemblage.

3.2 Introduction

The Illinois-Kentucky Mississippi Valley-type (MVT) district represents an

atypical occurrence of MVT mineralization dominated by fluorite instead of sphalerite,

galena, or barite. On average, the fluorite grade in the district is about 30 to 40%,

whereas the zinc, lead, and barite grades are only about 2 to 3%, 0.5 to 1%, and 1%,

respectively (Trace and Amos, 1984; Denny et al., 2013). The Illinois-Kentucky district

not only has a high fluorite grade but a high fluorite mass of originally at least 11 million

tonnes (Yancey, 1995; Goldstein, 1997), making it the largest known occurrence of

fluorite in the U.S. The large masses of unusually fluorite-rich MVT ore in the Illinois-

Kentucky district raise the question of how this ore may have formed. A long held

genetic hypothesis for the Illinois-Kentucky district is that the fluorite precipitated from ore fluids that were produced from mixing between a resident sedimentary brine and F-rich magmatic fluids derived from ultramafic magmatic bodies emplaced at depth in the district during the Permian period (e.g. Hall and Friedman, 1963; Heyl et al., 1966; Grogan and Bradbury, 1968; Hall and Heyl, 1968; Plumlee et al., 1995; Denny et al., 2015; Kenderes and Appold, 2017). The F-rich magmatic fluid and sedimentary brine mixture likely migrated from depth along subvertical faults, then exited the faults at shallower depths where the faults intersect permeable limestone formations (Fig. 3-1).
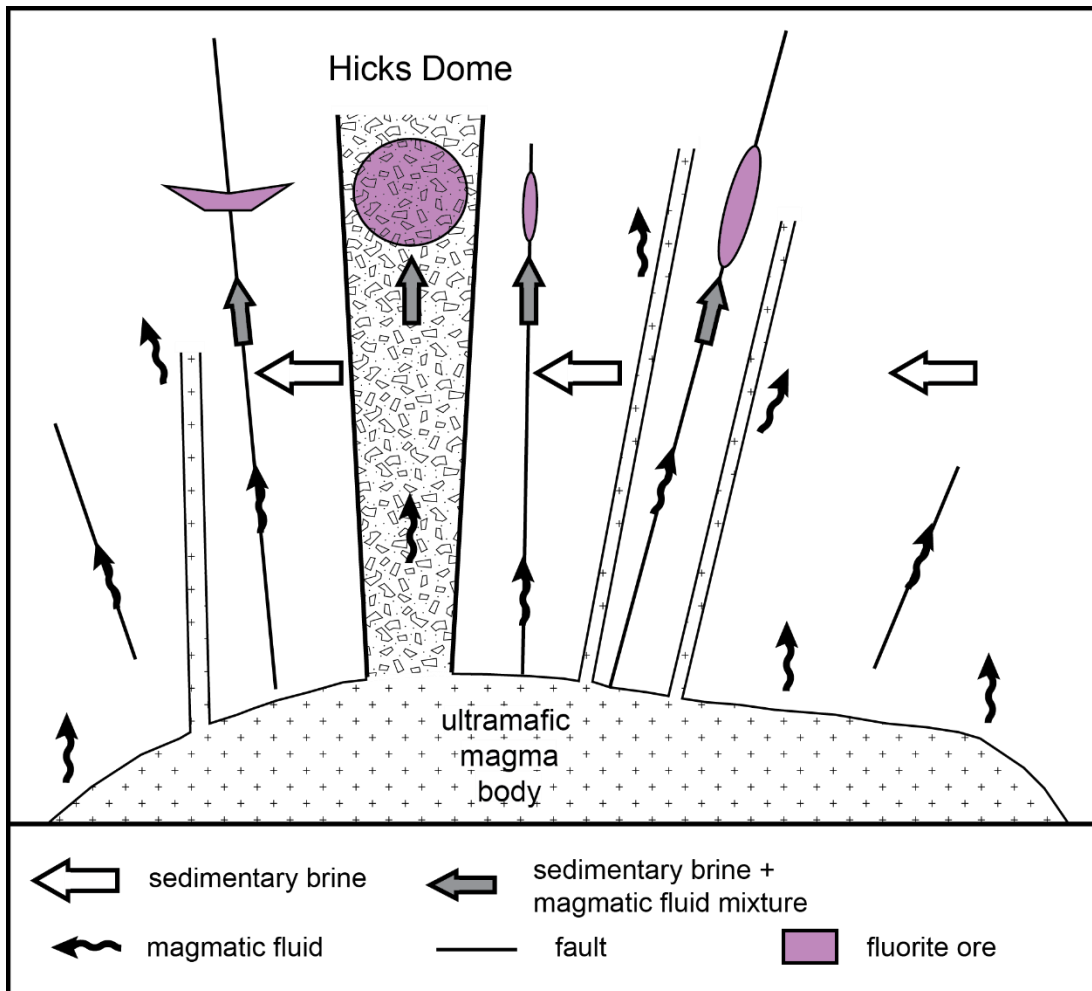

Figure 3-1. Conceptual ore genesis model after Plumlee et al. (1995) and Kenderes and Appold (2017) in which magmatic fluids travelling along faults, fractures, and diatremes mix with resident sedimentary brine forming the ore fluid from which fluorite ore precipitates.

Support for this hypothesis comes from a recent fluid inclusion study by Kenderes and Appold (2017), which suggests that the Illinois-Kentucky ore fluid had a F concentration between 680 and 4300 parts per million (ppm). Based on the high Ca concentration of the ore fluid, which averaged around 16,000 ppm (Pelch et al., 2015), in order for F to have remained dissolved in the ore fluid in such concentrations, a very low pH of 0 to 1.4 would have been required, which is much lower than the pH range of 4 to 5.5 typical of MVT ore fluids (Sverjensky, 1984). Further support for this genetic hypothesis comes from a reaction path modeling study by Plumlee et al. (1995), who found that introduction of a HF-rich fluid into a brine at 300° C, and the subsequent cooling of this fluid mixture to 150° C and its reaction with limestone could produce a fluorite-rich deposit. In their model, Plumlee et al. (1995) calculated the ore fluid to have a F concentration of 2000 ppm and a pH of 2.1.

The purpose of the present study was to conduct a further test of the hypothesis that F-rich, acidic fluids were responsible for the formation of the Illinois-Kentucky MVT mineralization. The present study extended the work of Plumlee et al. (1995) by coupling fluid flow, heat transport, and solute transport with chemical reaction using numerical reactive transport modeling. This allowed predictions of the spatial distribution of mineralization and fluid characteristics to be made that are not possible in static fluid reaction path models, which permit only chemical reaction sequences to be predicted. Of particular interest was the behavior of the mineralizing fluids as they rose through the faults and exited laterally through the ore-hosting aquifers, including the amount of limestone dissolution they caused, how far the fluids could travel before their

acidity became neutralized and they lost their mineralizing capacity, and the relative

abundance and locations of minerals precipitated.

3.3   Geologic Setting

Detailed descriptions of the geologic setting of the Illinois-Kentucky MVT

district have been provided by Bastin et al. (1939), Brecke (1962), Brown et al. (1954),

Heyl et al. (1965), Grogan and Bradbury (1968), Baxter et al. (1973); Baxter and

Bradbury (1989); and Bradbury and Baxter, (1992).   The following description is

summarized from their work. The Illinois-Kentucky MVT district encompasses an area

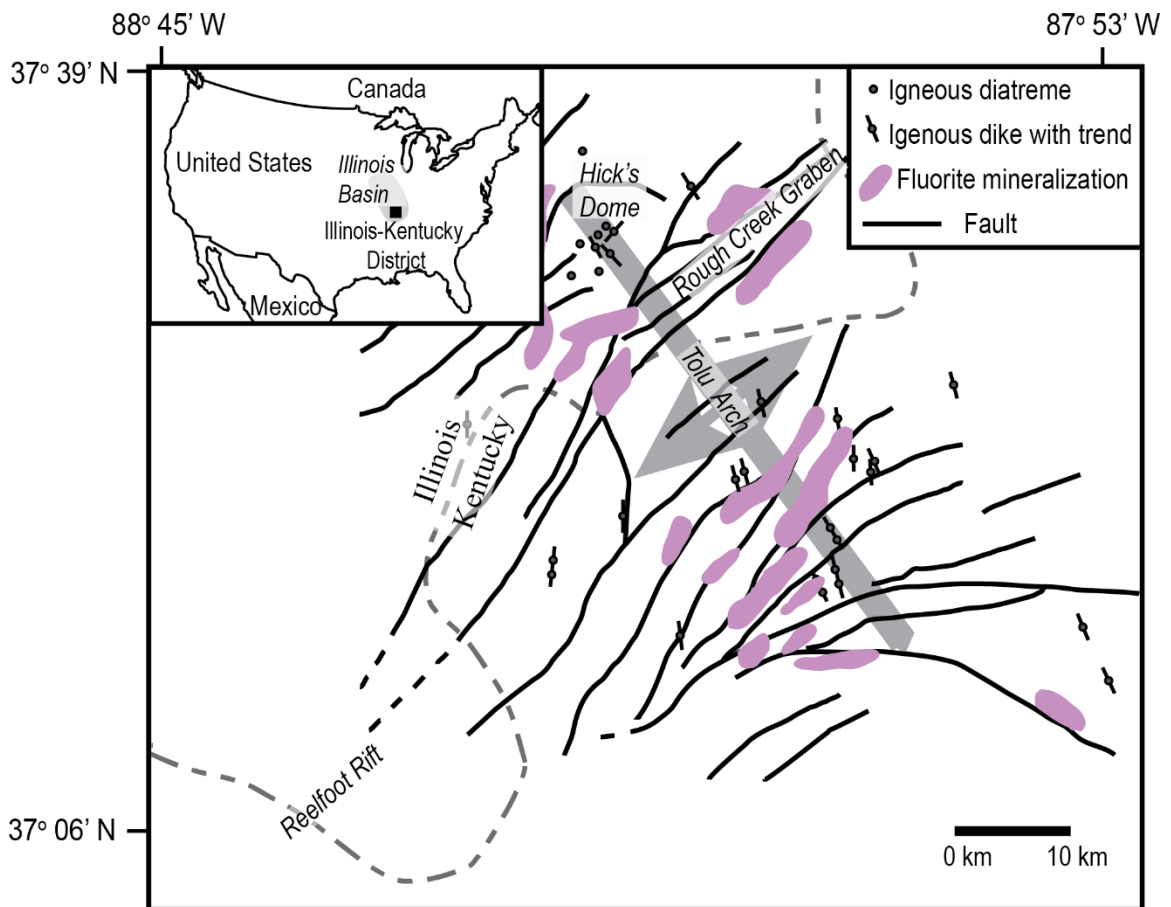of approximately 2600 km^2 near the southern end of the Illinois basin near the

Figure 3-2. Map of the Illinois-Kentucky district showing occurrences of MVT mineralization, igneous occurrences, and major structural features including faults. Inset map shows location of Illinois-Kentucky district. After Kenderes and Appold (2017).

68

intersection between the Cambrian Rough Creek Graben and the Neoproterozoic Reelfoot Rift (Fig. 3-2).

Mineralization in the district is associated with the Tolu arch, a northwest trending domal anticline that is cross cut by a series of northeast trending normal faults and intruded by numerous Permian aged ultramafic dikes and sills. The apex of the Tolu arch is located at Hicks dome, widely interpreted to be a cryptoexplosive igneous structure based on the presence of ultramafic dikes, diatremes, and intrusive breccia pipes near the center of the structure as well as associated radially distributed faults and fractures. These structures and intrusive igneous bodies are considered to be the result of emplacement of a deep-seated igneous body in the Illinois-Kentucky district, possibly associated with reactivation of the Reelfoot Rift and Rough Creek Graben during the Late Paleozoic formation and later Mesozoic breakup of Pangea.

Three main styles of MVT ore mineralization are observed in the Illinois-Kentucky district. The first and most widespread is vein filling mineralization found in normal faults hosted in Middle to Upper Mississippian limestone. The faults in the district commonly exhibit vertical displacements from 30 to 150 m, though along portions of the Rough Creek and Dixon Grabens displacement exceeds 600 m (Nelson, 1995). Some of these faults penetrate to the Precambrian basement where they offset the contact between the basement and overlying Paleozoic sedimentary rocks (Potter et al., 1995). These faults may have acted as conduits for the flux of F derived from magma bodies emplaced in the basement to the shallower Mississippian limestones that host fluorite mineralization.

Bedding replacement deposits are the second type of MVT mineralization observed, primarily near the northern edge of the Rough Creek Graben in the Cave-in-Rock and Harris Creek subdistricts. As with the vein deposits, bedding replacement deposits are associated with fractures and faults. These deposits appear to have formed where siliciclastic aquitards, such as the Rosiclare Shale, arrested the rise of mineralizing fluids. These fluids then spread laterally through the underlying limestone, dissolving it and precipitating fluorite in thin, laterally extensive bodies.

Breccia deposits are the third type of MVT mineralization and mainly occur around Hicks Dome. The breccias are comprised of igneous and sedimentary clasts, with fluorite, barite, and sulfide mineralization occurring as cement, veinlets within rock fragments, and as replacement of limestone clasts (Bradbury and Baxter, 1992). The igneous breccias at Hicks Dome and associated fluorite are relatively enriched in rare earth elements, while fluorite from other part of the district are poor in rare earth elements (Moorehead, 2013; Denny et al., 2015).

Attempts to date MVT mineralization in Illinois-Kentucky have led to a wide range of estimates. Harder (1987, *in* Symons, 1994) used fission track dating to find Cretaceous ages of 135.7 ± 4.5 to 140.6 ± 4.7 Ma. Ruiz et al. (1998) used $^{87}Sr/^{86}Sr$ ratios measured in fluorite and the assumption that all Sr in the fluorite was derived from Permian igneous rocks located in the district to calculate a Jurassic age of 200 Ma. Symons (1994) reported a late Jurassic age for mineralization from paleomagnetic analysis. Brannon et al. (1997) used Th-Pb and U-Pb dating on ore-stage calcite to find the respective Jurassic ages of 194 ± 13 Ma and 195 ± 23. Chelsey et al. (1994) reported the oldest dates for the district from $^{147}Sm/^{144}Nd$ dating of fluorite. Their reported

Permian age of 272 ± 17 Ma falls within the age range of 258 ± 13 to 281 ± 14 Ma

determined for igneous intrusions in the district (Zartman et al., 1967; Nelson and Lumm,

1984; Snee and Hayes, 1992; Reynolds et al., 1997; Fifarek et al., 2001; Denny, 2005).

The mineralogy of the Illinois-Kentucky district is simple, with fluorite,

sphalerite, galena, and barite composing the ore mineral assemblage. Fluorite is

generally the dominant ore mineral, with the exception of the Hutson and Old Jim

deposits, where sphalerite is the dominant ore mineral. The sulfide minerals,

chalcopyrite and pyrite, are widespread in the district but not very abundant. Gangue

mineralization consists predominantly of calcite, with minor amounts of dolomite, quartz,

siderite, and witherite. The paragenetic sequences of the vein and bedding replacement

deposits, the two main deposit types in the district, are broadly similar (Richardson and

Pinckney, 1984; Spry et al., 1990; Fuhrmann, 1994; Spry and Fuhrmann, 1994). Both

deposit types are characterized by multiple distinct fluorite precipitation stages with

sphalerite, galena, and other sulfide minerals overlapping with at least one stage of

fluorite precipitation.

3.4 Modeling approach

In order to investigate fluid-rock interactions that may have led to ore formation

in the Illinois-Kentucky district, numerical reactive transport modeling was conducted

using the TOUGHREACT 2.0 software with the ECO2N equation of state module (Xu et

al., 2011). The model domain had horizontal dimensions of 500 m $\times$ 250 m and a height

of 500 m and encompassed a stratigraphic interval from the Fort Payne Limestone to the

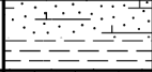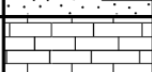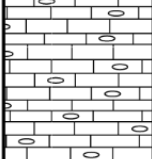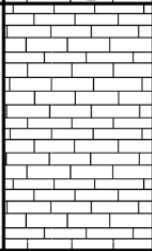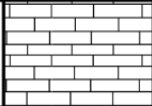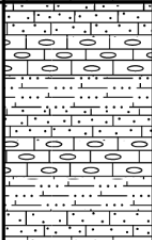| SYSTEM	SERIES	FORMATION	MEMBER	LITHOLOGY	THICK-NESS (m)	LITHOLOGIC DESCRIPTION
MISSISSIPPIAN	VALMEYERAN	AUX VASES SANDSTONE	Rosiclare		6 to 12	calcareous sandstone shale at base
		STE. GENEVIEVE LIMESTONE	Joppa		6 to 15	limestone locally oolitic and cherty
			Karnak		3 to 11	light limestone, locally oolitic
			Spar Mtn.		0 to 4	calcareous sandstone lenses
			Fredonia		25 to 30	fine-grained, cherty limestone locally oolitic
		ST. LOUIS LIMESTONE			106 to 122	fine grained, cherty limestone
		SALEM LIMESTONE			150 +/-	dark to black fine-grained limestone, locally fossiliferous
		ULLIN LIMESTONE			40 to 110	fine-grained limestone, crinoidal, bryzoans abundant
		FORT PAYNE FORMATION			70 to 195	siltstone, very fine-grained siliceous, cherty limestone

Figure 3-3. Interval of the Illinois-Kentucky district stratigraphic column on which the reactive transport models were based. Adapted from Grogan and Bradbury (1968) and Spry and Furman (1994).

Rosiclare Shale (Figs. 3-3 and 3-4). A vertical fault zone 9 m wide extended from the bottom boundary of the model domain to the base of the Rosiclare Shale.

The model domain was discretized into a rectangular prismatic grid consisting of 44 nodes in the x direction, 23 nodes in the y direction, and 51 nodes in the z direction. The nodal spacing in the z direction was constant at 10 m, whereas nodal spacing in the x

and *y* directions increased progressively from 3 m inside the fault to a maximum of 20 m with increasing distance from the fault.
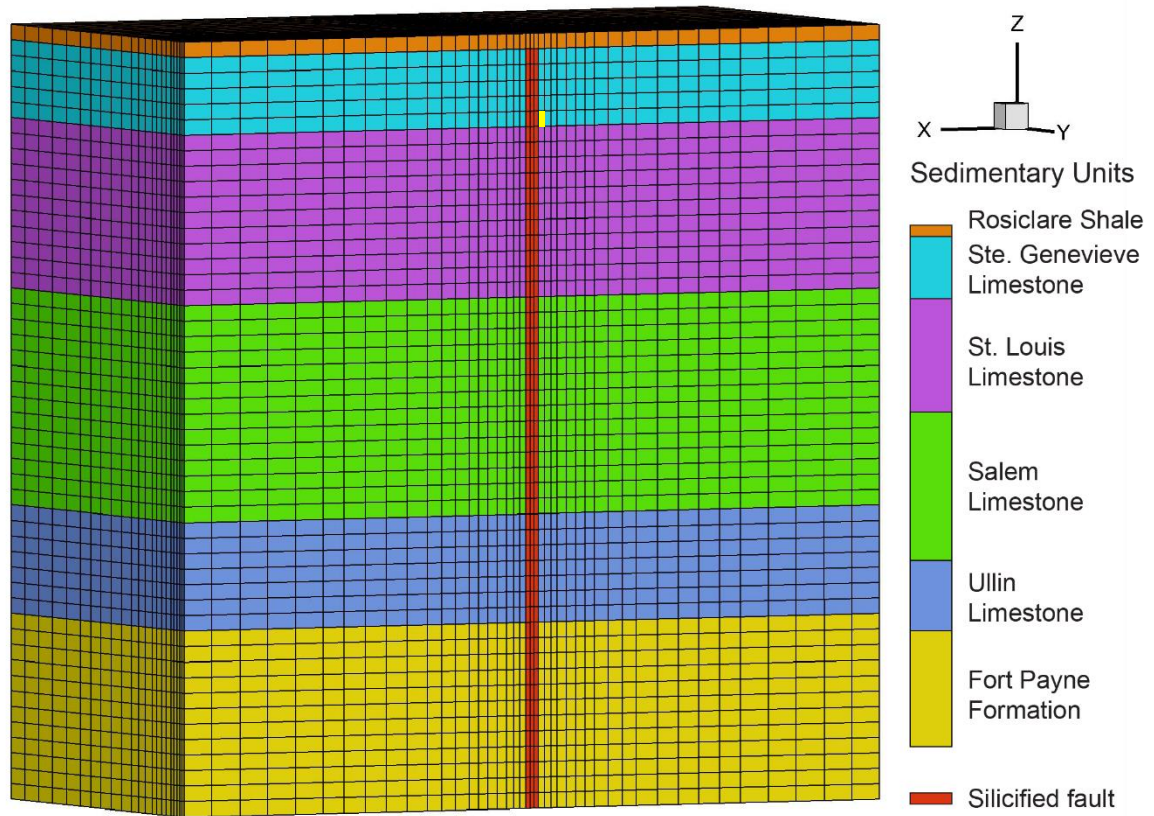
Figure 3-4. Numerical grid and hydrostratigraphic units for the reactive transport models. The yellow, highlighted cell in the Ste. Genevieve Limestone is the location of the fluorite grade evolutions shown in figure 3-16.

Values of hydrologic parameters used in the models are shown in Table 3-1. The permeabilities of the hydrostratigraphic units at the time of ore formation are not well constrained, therefore permeabilities within the range of typical values for limestone, siltstone, and shale were assigned to the Ste. Genevieve, Ft. Payne, and Rosiclare units, respectively (Domenico and Schwartz, 1998). The remaining sedimentary units were assigned permeabilities one hundred times lower than that of the Ste. Genevieve to facilitate the ascension of the fault fluid to the Ste. Genevieve. An initial simulation in which the permeabilities of the St. Louis, Salem, and Ullin units were

Table 3-1. Hydrologic parameters and initial mineral abundances of hydrostratigraphic units

Sedimentary Units	Thickness m	Initial Porosity	Initial Permeability		Initial Mineralogy						
			horizontal (m²)	vertical (m²)	Albite	Calcite	Illite	Orthoclase	Kaolinite	Oligoclase	Quartz
Rosiclare Shale	10	0.10	1.0E-19	1.0E-20	5%	0%	50%	10%	20%	5%	10%
Ste. Genevieve LS	50	0.15	1.0E-15	1.0E-16	0%	99%	0%	0%	0%	0%	1%
St. Louis LS	110	0.10	1.0E-17	1.0E-18	0%	80%	4%	0%	2%	0%	15%
Salem LS	140	0.10	1.0E-17	1.0E-18	0%	95%	3%	0%	1%	0%	1%
Ullin LS	70	0.10	1.0E-17	1.0E-18	0%	90%	6%	0%	2%	0%	2%
Ft. Payne Formation	120	0.05	2.0E-18	2.0E-19	5%	45%	7%	10%	3%	0%	30%
Silicified fault		0.10	1.0E-16	1.0E-14	5%	0%	0%	5%	0%	0%	90%

assumed to be ten times lower than that of the Ste. Genevieve failed to maintain a sufficient vertical pressure gradient to drive the fault fluid from the base of the fault into the Ste. Genevieve. The hydrostratigraphic units were assumed to be less permeable in the vertical direction than in the horizontal directions. The model fault was assumed to be more permeable than any of the hydrostratigraphic units and to be more permeable in the vertical direction than in the horizontal directions.

Specified temperature and specified pressure boundary conditions were applied at the fault base, the far left ($x = 0$) and far right ($x = 500$) ends of the model domain. No flow boundary conditions were applied to the remaining edges of the model domain.

An initial temperature of 90° C was assigned to the top of the model domain with a vertical geothermal gradient of 25 °C/km. A pressure of 150 bars was assigned to the left edge of the top model boundary ($x = 0$, Fig. 3-4). A lateral pressure gradient of 96 Pa/m corresponding to a regional hydraulic head gradient of 0.01 m/m was assigned in the x direction, and pressure was assumed to increase hydrostatically with increasing depth in the vertical direction. The pressure at the base of the vertical fault was set to 75% of lithostatic pressure (~339 bar), which caused fluid to move up the fault.

In all of the model simulations, resident sedimentary brine was assumed to be initially present throughout the model domain. However, two different broad resident brine scenarios were investigated—a one resident brine scenario, in which a single prevalent resident brine was initially present throughout the model domain, and a two resident brine scenario, in which the prevalent resident brine of the previous scenario was present everywhere in the model domain except in the lower Rosiclare Shale and upper Ste. Genevieve Limestone (Fig. 3-4), which contained a brine that was richer in sulfur but

poorer in Pb and Zn than the prevalent brine. The major element composition, silica, aluminum, carbonate, and F concentrations of the prevalent and sulfur-rich, metal-poor brines were identical and derived from Pelch et al. (2015), equilibrium with respect to quartz, kaolinite, and calcite, and typical modern sedimentary brines (Appold, 2021), respectively (Table 3-2). Both brines had a moderately acidic pH of 5.2, typical of MVT ore fluids (Sverjensky, 1984), and a reducing log f_{O_2} of -55.4 (Pelch et al., 2015).

Table 3-2. Compositions of model fluids used in this study.

Aqueous Species	Resident brine mol/kg	Sulfur-rich brine mol/kg	Fault Fluid 1a mol/kg	Fault Fluid 1b mol/kg	Fault Fluid 2a mol/kg	Fault Fluid 2b mol/kg
AlO_2^-	5.0E-07	5.0E-07	5.0E-07	5.0E-07	5.0E-07	5.0E-07
Ca^{2+}	3.7E-01	3.7E-01	7.5E-02	3.7E-01	7.5E-02	3.7E-01
Cl^-	3.7E+00	3.7E+00	3.3E+00	3.7E+00	3.3E+00	3.7E+00
K^+	8.0E-02	8.0E-02	8.0E-02	8.0E-02	8.0E-02	8.0E-02
Mg^{2+}	4.1E-02	4.1E-02	4.1E-02	4.1E-02	4.1E-02	4.1E-02
Na^+	2.8E+00	2.8E+00	2.8E+00	2.8E+00	2.8E+00	2.8E+00
$SiO_2(aq)$	1.0E-03	1.0E-03	1.0E-03	1.0E-03	1.0E-03	1.0E-03
F^-	6.0E-05	6.0E-05	6.0E-02	2.0E-04	6.0E-02	2.0E-04
SO_4^{2-}	1.0E-06	1.0E-02	1.0E-02	1.0E-04	1.0E-06	1.0E-06
Pb^{2+}	2.1E-05	3.3E-09	2.0E-04	1.0E-05	2.0E-04	2.0E-04
Zn^{2+}	3.0E-04	1.6E-07	6.0E-03	1.0E-04	6.0E-03	6.0E-03
Ba^{2+}	3.5E-04	3.5E-04	3.5E-04	3.5E-04	3.5E-04	3.5E-04
salinity (wt% NaCl)	20	20	20	20	20	20
pH	5.5	5.5	1.1	4.0	1.1	4.0
$\log f_{O_2}$	-55.4	-55.4	-55.4	-55.4	-55.4	-55.4

In the prevalent brine, the concentration of Zn was derived from Smith-Schmitz and Appold (2018), and the concentration of Pb was determined from the average Pb:Zn ratio

in modern sedimentary brines reported by Hanor (1996). In the prevalent brine, the sulfur concentration was chosen to cause sphalerite and galena to be slightly undersaturated. In the sulfur-rich, metal-poor brine, the sulfur concentration was chosen from the upper limit of the range of concentrations reported for modern sedimentary brines (Appold, 2021) and Zn and Pb concentrations were lowered to the saturation points of sphalerite and galena, respectively.

In all of the model simulations, F-bearing fluid was introduced into the model domain at the base of the vertical fault. The model F-bearing fluid was assumed to be a mixture of predominantly sedimentary brine and a smaller amount of magmatic fluid, which was the source of the F. This assumption is based on the likelihood that the magmatic fluid ascended the fault over a distance on the order of kilometers and thus would have had opportunity to mix with brine in the sedimentary units that the fault intersected (Potter et al., 1995). In the models, the fluid entering the fault could be either relatively F-rich, with a F concentration of 0.06 mol/kg (1000 ppm), representative of the F concentrations found by Kenderes and Appold (2017), or relatively F-poor, with a F concentration of 2×10^{-4} mol/kg (4 ppm), representative of the F concentrations typical of modern sedimentary brines (Appold, 2021). The remaining chemical constituents in the fluid entering the fault had concentrations the same as those of the prevalent resident brine, with the exception of Ca^{2+}, whose concentration was lowered to the point of fluorite saturation for a F concentration of 0.05 mol/kg, and Cl^{-}, whose concentration was lowered to maintain charge balance. Fluorite saturation also governed the pH of the high-F and low-F fault fluids.

Thus, a total of four model scenarios were investigated in the present study: (1a) a single resident brine with a high-F fault fluid, (1b) a single resident brine with a low-F fault fluid, (2a) two resident brines with a high-F fault fluid, (2b) two resident brines with a low-F fault fluid. The purpose of varying the F concentration in the models was to test the importance of F concentration in producing the mineral assemblages observed in the field. The purpose of varying the number and composition of the resident brines was to test the importance of two possible sulfide mineral precipitation mechanisms. In the single resident brine scenarios, sulfide mineral precipitation is caused by increasing the pH of the fault fluid. In the two resident brine scenarios, sulfide mineral precipitation is caused by mixing of the sulfide-rich fluid in the lower Rosiclare Shale and upper Ste. Genevieve Limestone with the more metal rich fluid ascending the fault and the prevalent sedimentary brine.

3.5 Results

3.4.1. Fluid Pressure, Flow, and Temperature
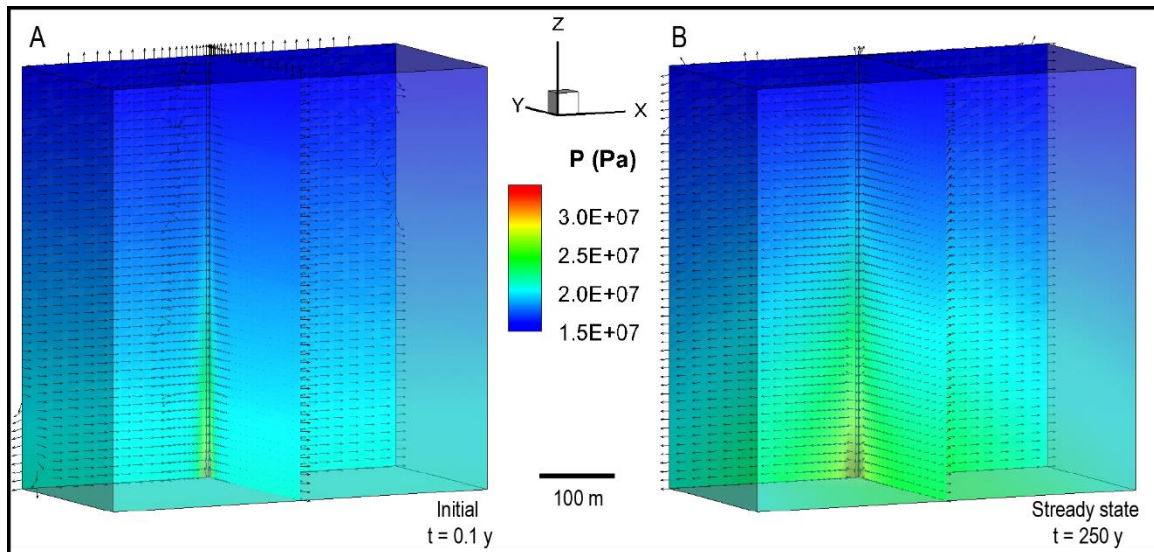
Figure 3-5. Simulated fluid pressure velocity fields after (A) 0.1 year and (B) 250 years shown in slice planes that are orthogonal to the *x* and *y* coordinate axes.

78

Because the four model scenarios differed only with respect to their chemical characteristics and were identical with respect to their physical characteristics, the four model scenarios produced identical fluid pressure, flow, and temperature fields. Figure 3-5 shows the evolution of the fluid pressure and flow fields in two slices through the model domain that are orthogonal to the x and y coordinate axes. Fluid flow is initially horizontal in the direction of increasing x, following the initial regional horizontal pressure gradient, and reaches average Darcy velocities ranging from 3×10^{-4} m/y in the Fort Payne Limestone to 0.2 m/y in the Ste. Genevieve Limestone. The presence of the high fluid pressure source at the base of the fault causes a surge of increased fluid pressure up the fault and a slower lateral diffusion of pressure from the fault into the lower permeability surroundings, reaching a steady state after 250 years. Fluid flow rates within the fault range from 400 m/y to 3 m/y from the base to the top of the fault. The elevated fluid pressures within the fault and their lateral diffusion led to a radial pattern of fluid flow away from the fault, significantly altering the initial flow field.
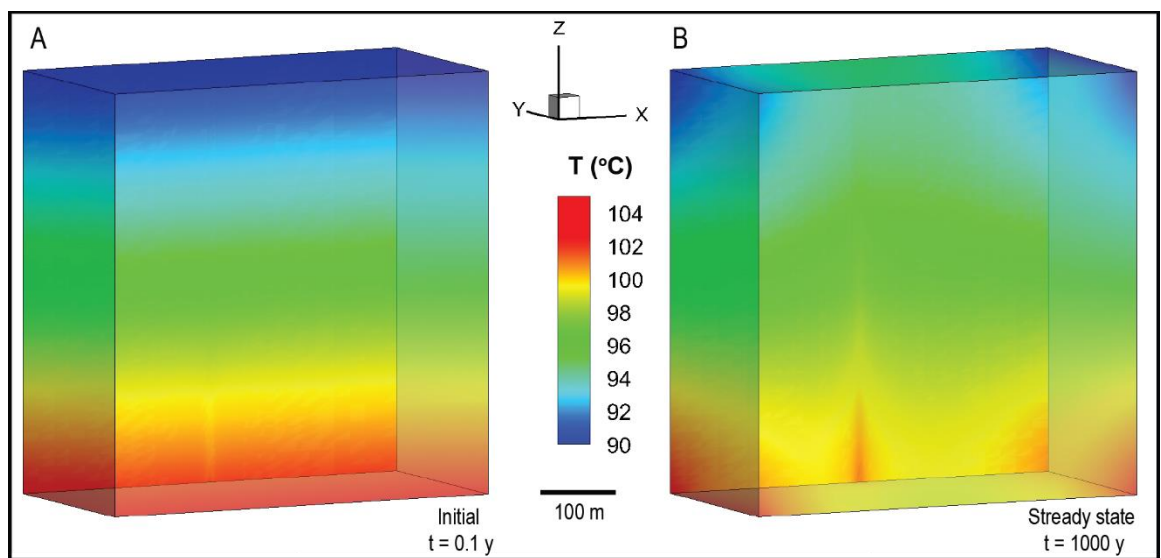
Figure 3-6. Simulated temperature field after (A) 0.1 year and (B) 1000 years.

The strong upward fluid flow in the fault causes a significant redistribution of heat relative to the initial linear conductive vertical temperature gradient, reaching a steady state by 1000 years. Heat from the lower portion of the model is advected upward, reducing temperatures near the base of the model by up to about 4° C, and raising temperatures near the top of the model by up to about 6° C. The vertical temperature gradient in the model was overall diminished, while a small horizontal temperature gradient centered on the fault was created.

3.4.2. Single Resident Brine Model (Scenarios 1a and 1b)

In this section, results are described from Model Scenarios 1a and 1b in which a single resident brine composition was initially present throughout the model domain and a fluid was introduced at the base of the fault that could be either relatively rich in F (1000 ppm) or poor in F (4 ppm), respectively (Table 3-2). However, in both model scenarios, the F concentration of the fault fluid was higher than that of the resident brine, which was 1 ppm.

3.4.2.1 pH

Figure 3-7 shows the simulated pH for the two model scenarios. The F content of the fault fluid was high enough in both model scenarios to lower the pH significantly from the initial value of 5.5 in the resident brine to 1.1 in the high-F fault fluid and 4.2 in the low-F fault fluid. These lower pH values were maintained along the entire height of the fault because its silicified boundaries prevented the fluid inside the fault from reacting with the surrounding limestone. Once the fluids exited the fault into limestone, they were

Figure 3-7. Simulated changes in pH for Model Scenario 1a after (A) 500 years, (B) 1000 years, (C) 2000 years, and for Model Scenario 1b after (D) 500 years, (E) 1000 years, and (F) 2000 years.

rapidly neutralized within about two meters of the fault to the pH of 5.5 of the resident brine. This shows that even a very low pH fluid cannot travel very far through limestone, limiting possible flow paths for the acidic fluorine ore fluids and locations where host

rock dissolution and fluorite mineralization could be expected. By 2000 years, only a small expansion of low pH fault fluid into the base of the Ste. Genevieve Limestone occurs in Scenario 1a but not in Scenario 1b, reflecting the differences in the respective acidities of the fault fluids in the two scenarios and their ability to dissolve the host rock.

3.4.2.2 Fluorine Concentration

The simulated F concentrations for Model Scenarios 1a and 1b are shown in Figure 3-8. Model Scenarios 1a and 1b are qualitatively similar, differing only in the magnitude of F concentration, which reaches a maximum of 1000 ppm in Model Scenario 1a in the fault and about 4 ppm in Model Scenario 1b. In both scenarios, F is transported rapidly up the fault, with slower horizontal transport of F occurring radially from the fault. The fastest horizontal F transport occurs in the Ste. Genevieve Limestone, forming a broad plume that ponds beneath the Rosiclare Shale. Significant horizontal migration of F also occurs deeper in the model, promoted by the higher fluid pressures near the base of the fault. These higher fluid pressures coupled with the higher permeability of the Ullin Limestone relative to the underlying basal Fort Payne Formation cause another broad plume of F to develop in the Ullin Limestone that gradually narrows with decreasing depth.

Figure 3-8. Simulated F concentrations (ppm) for Model Scenario 1a at (A) 500 years, (B) 1000 years, and (C) 2000 years, and for Model Scenario 1b at (D) 500 years, (E) 1000 years, and (F) 2000 years.

3.4.2.3 Calcite Dissolution and Porosity

Figure 3-9. Simulated changes in volume fraction of calcite for Model Scenario 1a after (A) 500 years, (B) 1000 years, (C) 2000 years, and for Model Scenario 1b after (D) 500 years, (E) 1000 years, and (F) 2000 years.

In both model scenarios, the lowered pH of the fluid ascending the fault causes

calcite dissolution along the fault as some of the fluid seeps into the adjacent limestone

units (Fig. 3-9). In Model Scenario 1a, calcite dissolution occurs along the entire length
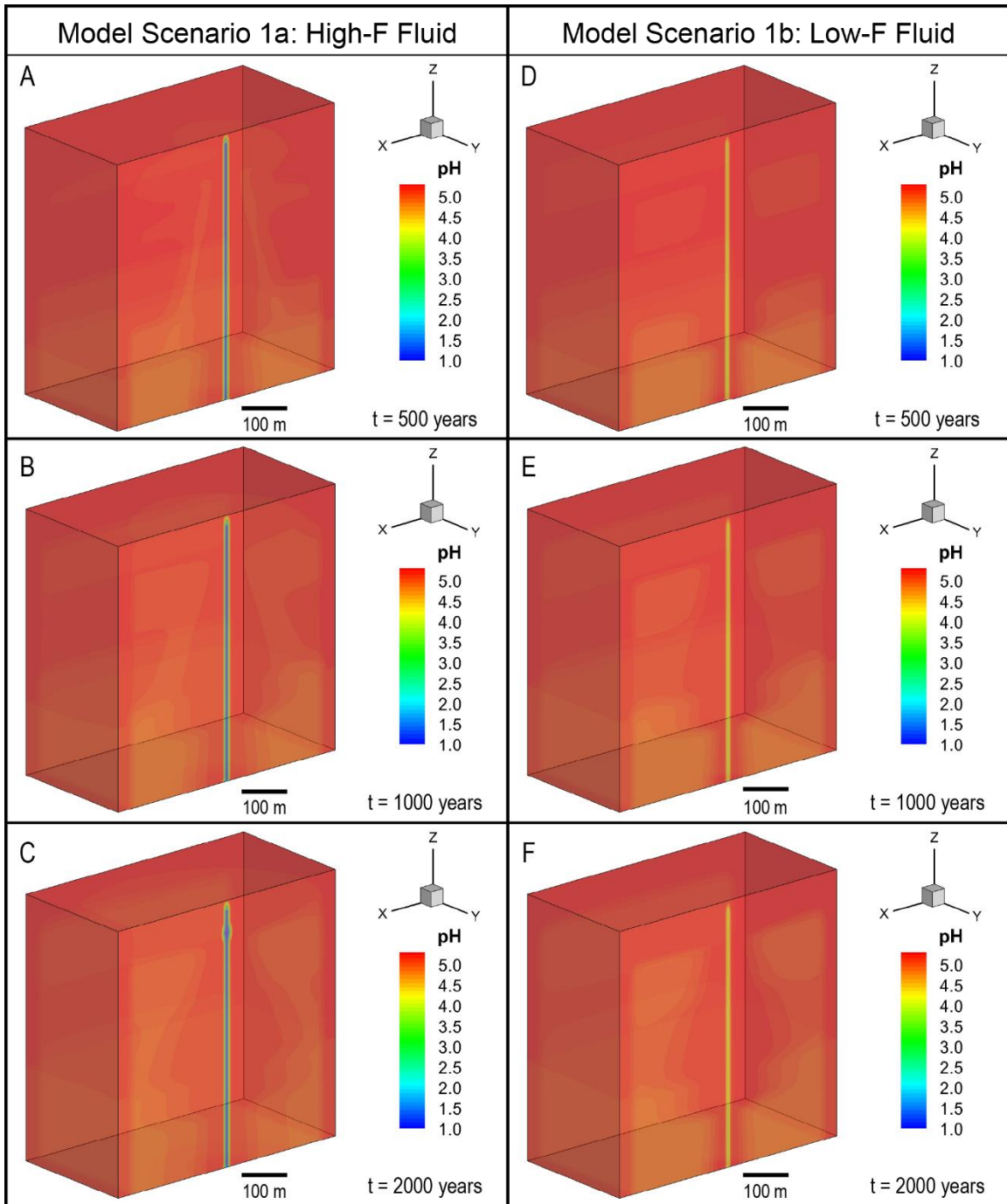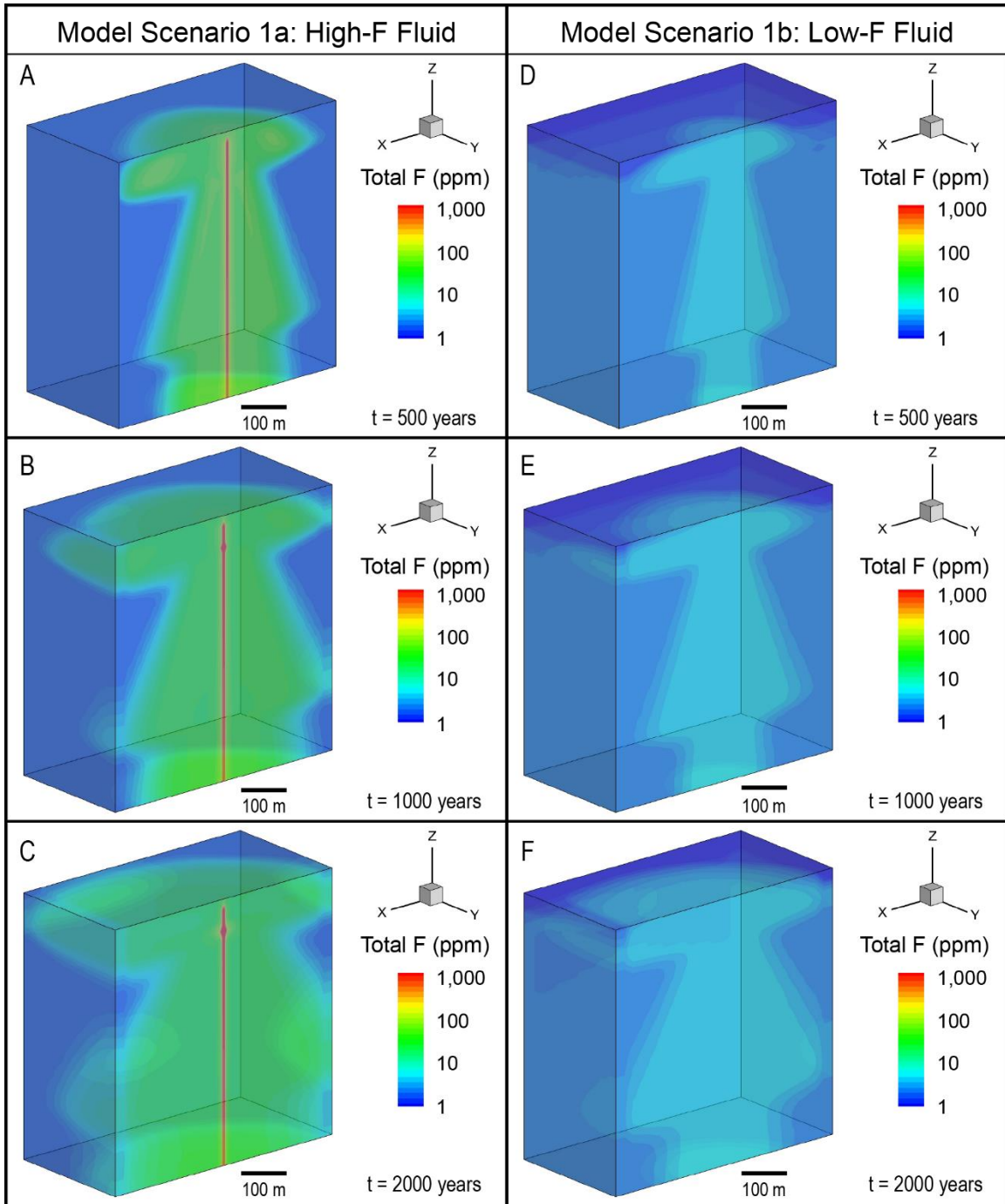

Figure 3-10. Simulated porosity (fraction) for Model Scenario 1a after (A) 500 years, (B) 1000 years, and (C) 2000 years and for Model Scenario 1b after (D) 500 years, (E) 1000 years, and (F) 2000 years.

of the fault whereas in Model Scenario 1b, calcite dissolution is discontinuous, especially

at earlier simulation times, and about an order of magnitude lower than in Model

85

Scenario 1a. In both of the model scenarios, most of the calcite dissolution occurs within a few meters of the fault, with the greatest amount of calcite dissolution occurring near the base of the Ste. Genevieve Limestone. In Model Scenario 1a after 2000 years, porosity there increased to over 55% and in Model Scenario 1b to about 16% from an initial porosity in both scenarios of 15% (Fig. 3-10).

3.4.2.4 Fluorite

The distribution of fluorite mineralization predicted for Model Scenarios 1a and 1b resembled the predicted distribution of aqueous F concentration. A broad, lateral plume of diffuse fluorite mineralization develops in the Ste. Genevieve Limestone near the top of the model domain and is underlain by two thicker plumes of diffuse mineralization (Fig. 3-11). Thus, in both scenarios, fluorite mineralization occurs along the entire height of the model domain but is most concentrated immediately adjacent to the fault, though little if any fluorite occurs within the fault itself. In Model Scenario 1a after 2000 years, fluorite mineralization reaches a volume fraction of 0.2 in the Ste. Genevieve Limestone and of 0.05 in the underlying limestone units. Fluorite concentrations decrease strongly with increasing distance from the fault, ranging from volume fractions of about 10^{-6} to 10^{-2} in the diffuse fluorite plumes. However, in the Ste. Genevieve Limestone within about 9 meters of the fault, fluorite has an average concentration of about 30 weight percent, which is about the average fluorite ore grade in the Illinois-Kentucky district, and a mass of about 2300 tonnes. In contrast, in Model Scenario 1b after 2000 years, fluorite reaches only negligible volume fractions on the order of 10^{-9} to 10^{-8}, several orders of magnitude lower than predicted in Model Scenario
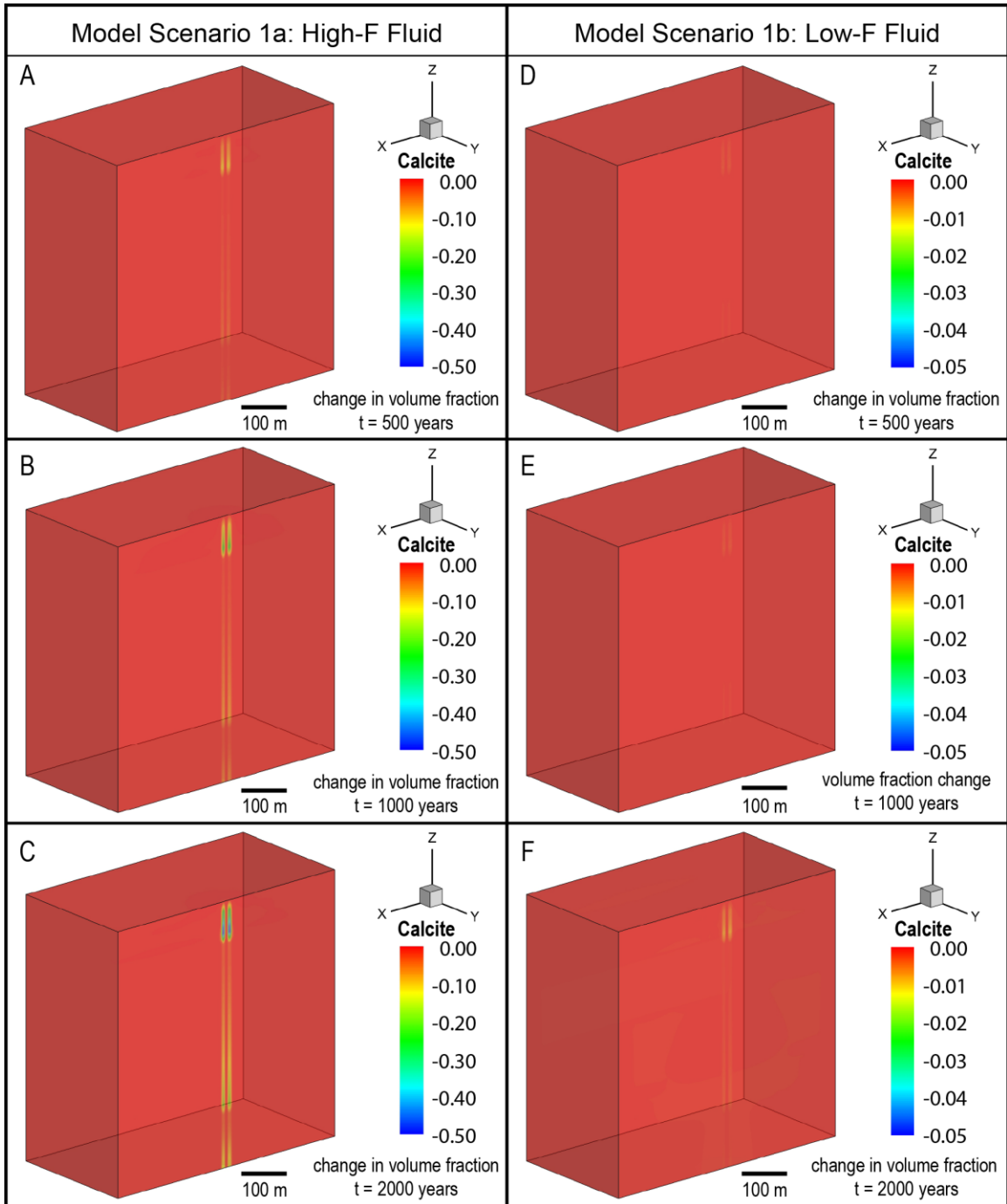
Figure 3-11. Simulated change in fluorite volume fraction for Model Scenario 1a after (A) 500 years, (B) 1000 years, and (C) 2000 years, and for Model Scenario 1b after (D) 500 years, (E) 1000 years, and (F) 2000 years.

1a. The results point to the importance of high aqueous F concentration in order to produce fluorite ore bodies. The high F concentrations increase the fluorite to host rock

87

ratio, as the high F concentrations acidify the fluid, promoting dissolution of the

limestone host rock, and supply abundant F for the precipitation of fluorite.

3.4.2.5 Galena and Sphalerite

Figure 3-12. Simulated change in galena volume fraction for Model Scenario 1a after (A) 500 years, (B) 1000 years, and (C) 2000 years, and for Model Scenario 1b after (D) 500 years, (E) 1000 years, and (F) 2000 years.
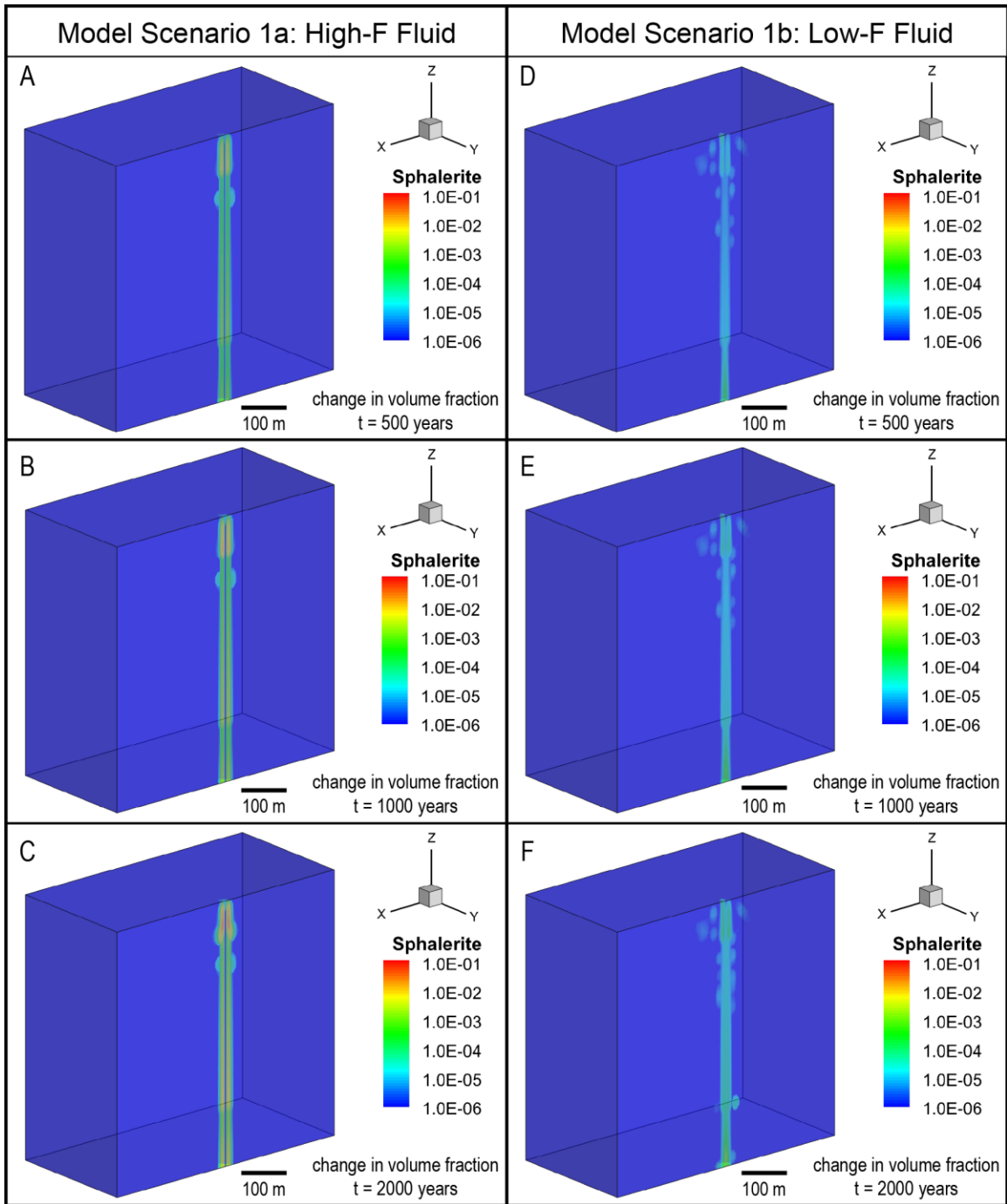
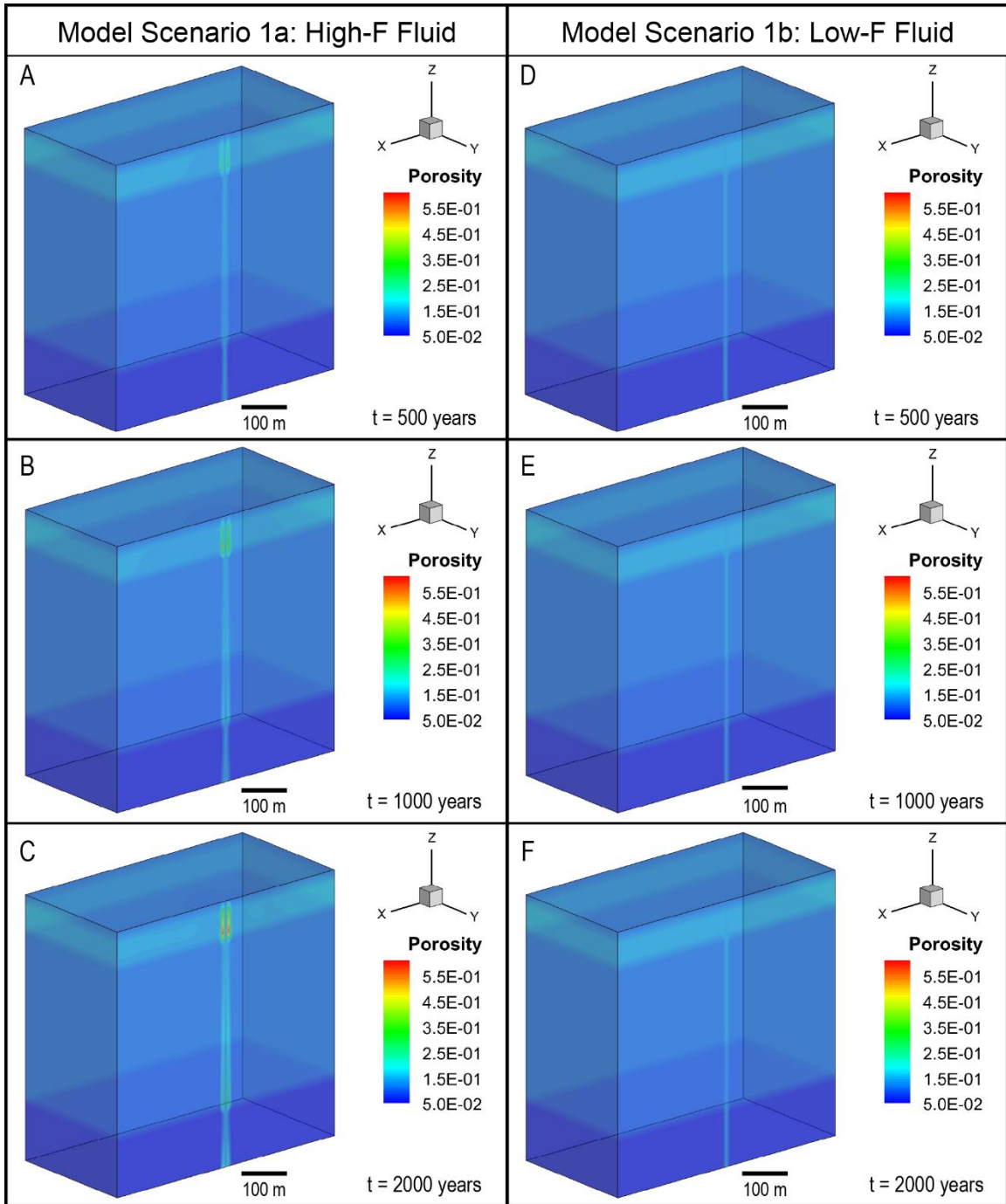**Figure 3-13.** Simulated change in sphalerite volume fraction for Model Scenario 1a after (A) 500 years, (B) 1000 years, and (C) 2000 years, and for Model Scenario 1b after (D) 500 years, (E) 1000 years, and (F) 2000 years.

In Model Scenarios 1a and 1b, sphalerite and galena were both predicted to precipitate mainly in a narrow (~5 to 10 m) radius along the fault (Figs. 12 and 13). However, in contrast to fluorite, sphalerite and galena were not predicted to precipitate in

89

broad diffuse zones far from the fault. In Model Scenario 1a, galena and sphalerite were particularly concentrated in the Ste. Genevieve Limestone within a radius of about 20 m from the fault, reaching maximum volume fractions of 0.0025 and 0.015, respectively, after 2000 years. Outside the Ste. Genevieve Limestone, volume fractions of galena and sphalerite along the fault are generally 1-2 orders of magnitude lower than inside the Ste. Genevieve.

In Model Scenario 1b, the predicted volume fractions of galena and sphalerite were overall orders of magnitude lower than in Model Scenario 1b, reaching maximum values of order 10^{-4} and 10^{-3}, respectively, after 2000 years. Further, the highest simulated galena and sphalerite volume fractions were in the basal Fort Payne Limestone rather than the Ste. Genevieve Limestone. Outside the Fort Payne, simulated galena and sphalerite volume fractions reached no higher than 10^{-6} to 10^{-5} and 10^{-5} to 10^{-4}, respectively. A further difference between Model Scenarios 1a and 1b is that in 1b, galena and sphalerite were predicted to precipitate within the fault as well as outside it. In addition, several small, discrete satellite bodies of mineralization were predicted to precipitate beyond the fault.

3.4.3 Two Resident Brine Model (Scenarios 2a and 2b)

In the single resident brine model (i.e. Model Scenario 1), galena and sphalerite precipitate mainly as a result of a pH increase as fluid migrates laterally out of the fault and reacts with the surrounding limestone. This sulfide mineral precipitation mechanism is inefficient because metals and sulfide are transported together in the same fluid and have solubility in one another's presence. Because the solubility of Pb and Zn in the absence of sulfide and the solubility of sulfide in the absence of base metals are high, a

more efficient sulfide mineral precipitation mechanism is mixing between a metal-rich, sulfide-poor fluid and a metal-poor, sulfide-rich fluid. The resultant mixture is highly supersaturated with respect to sulfide minerals, causing them to precipitate more quickly and in larger amounts than when metals and sulfide are transported together in the same solution and precipitate by pH change. The purpose of investigating Model Scenario 2 was to determine whether it fit field observations more closely than Model Scenario 1.

Because Model Scenarios 1 and 2 differed chiefly in their initial spatial distribution of aqueous metal and sulfide concentrations, they did not differ significantly in their predictions of aqueous F concentration or fluorite abundance. Further, because pH in the models is governed principally by F concentration, and because calcite dissolution and porosity are governed principally by pH, Model Scenarios 1 and 2 did not differ significantly in their predictions of pH, calcite dissolution, or porosity. Thus, plots of these results are not shown for Model Scenario 2. However, Model Scenarios 1 and 2 do differ significantly with respect to their simulated galena (Fig. 3-14) and sphalerite (Fig. 3-15) abundances, though Model Scenarios 2a and 2b do not. In both Model Scenarios 2a and 2b, most of the sulfide mineral precipitation occurs in a broad, tabular plume in the Ste. Genevieve Limestone centered on the fault, with the sphalerite plume a bit broader than the galena plume. In contrast to Model Scenario 1, where most of the sulfide mineral precipitation occurs along the fault, in Model Scenario 2 only a little galena precipitation occurs within and immediately adjacent to the fault in the units underlying the Ste. Genevieve Limestone. Volume fractions of galena and sphalerite in the plumes are on the order of 10^{-6} to 10^{-5}, with maximum values of 3.5×10^{-5} and 2×10^{-5}, respectively, near the intersection of the Ste. Genevieve with the fault where
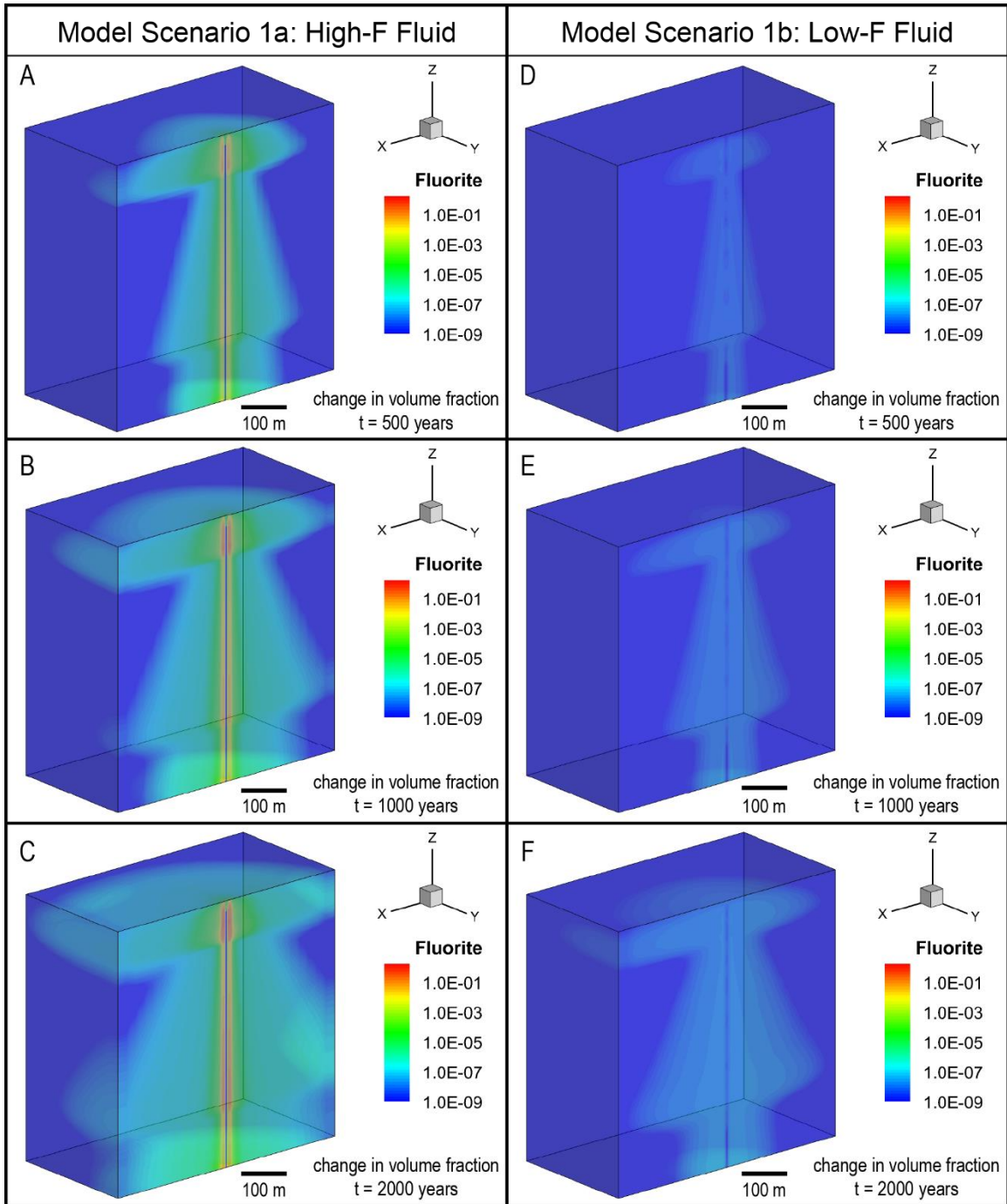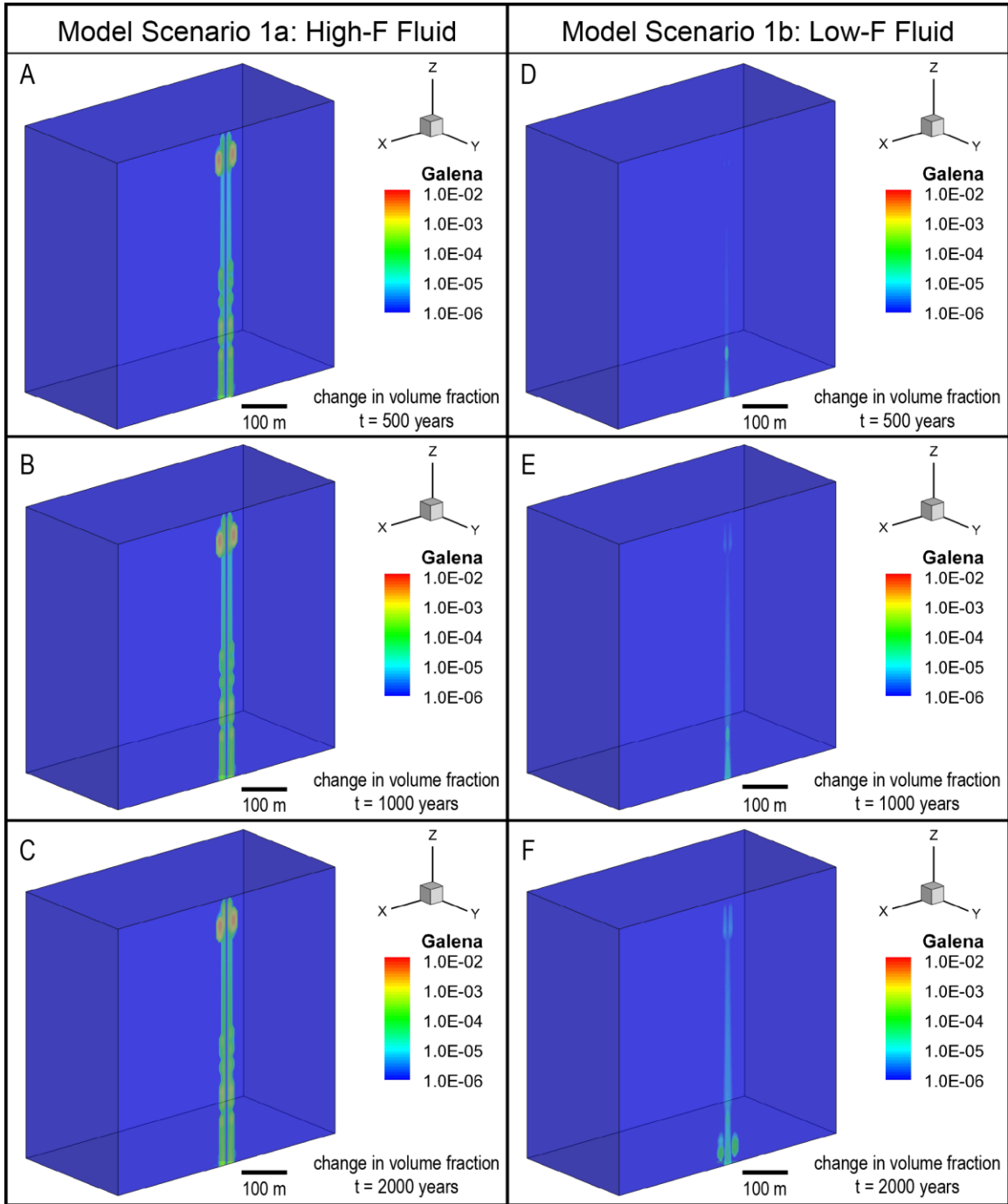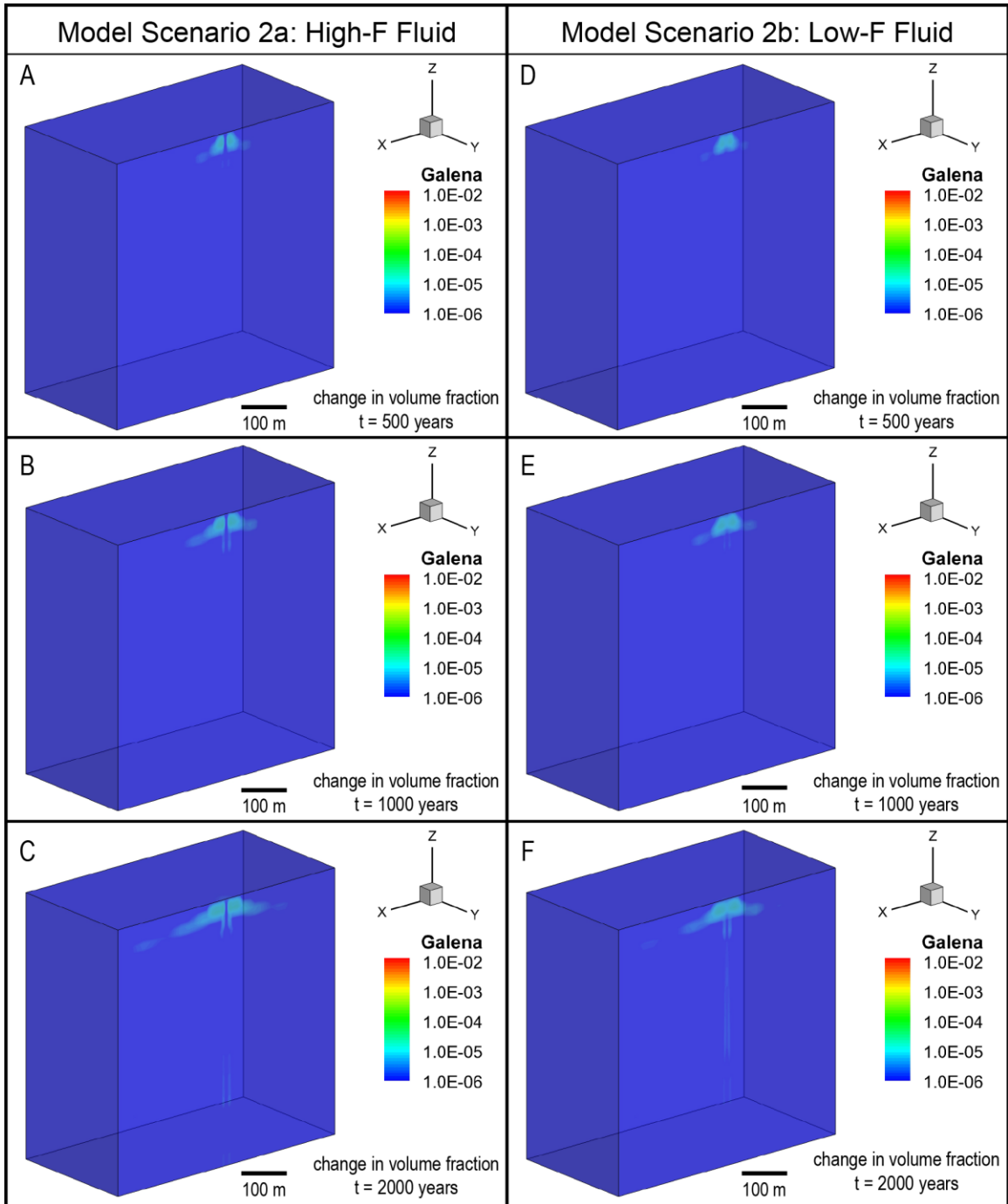
Figure 3-14. Simulated change in galena volume fraction for Model Scenario 2a after (A) 500 years, (B) 1000 years, and (C) 2000 years, and for Model Scenario 2b after (D) 500 years, (E) 1000 years, and (F) 2000 years.

mixing first occurs. These galena and sphalerite volume fractions are reached early in the simulations and do not change significantly over time, though the volume of the plumes grows by a factor of four from 500 to 2000 years of simulation time. The volume
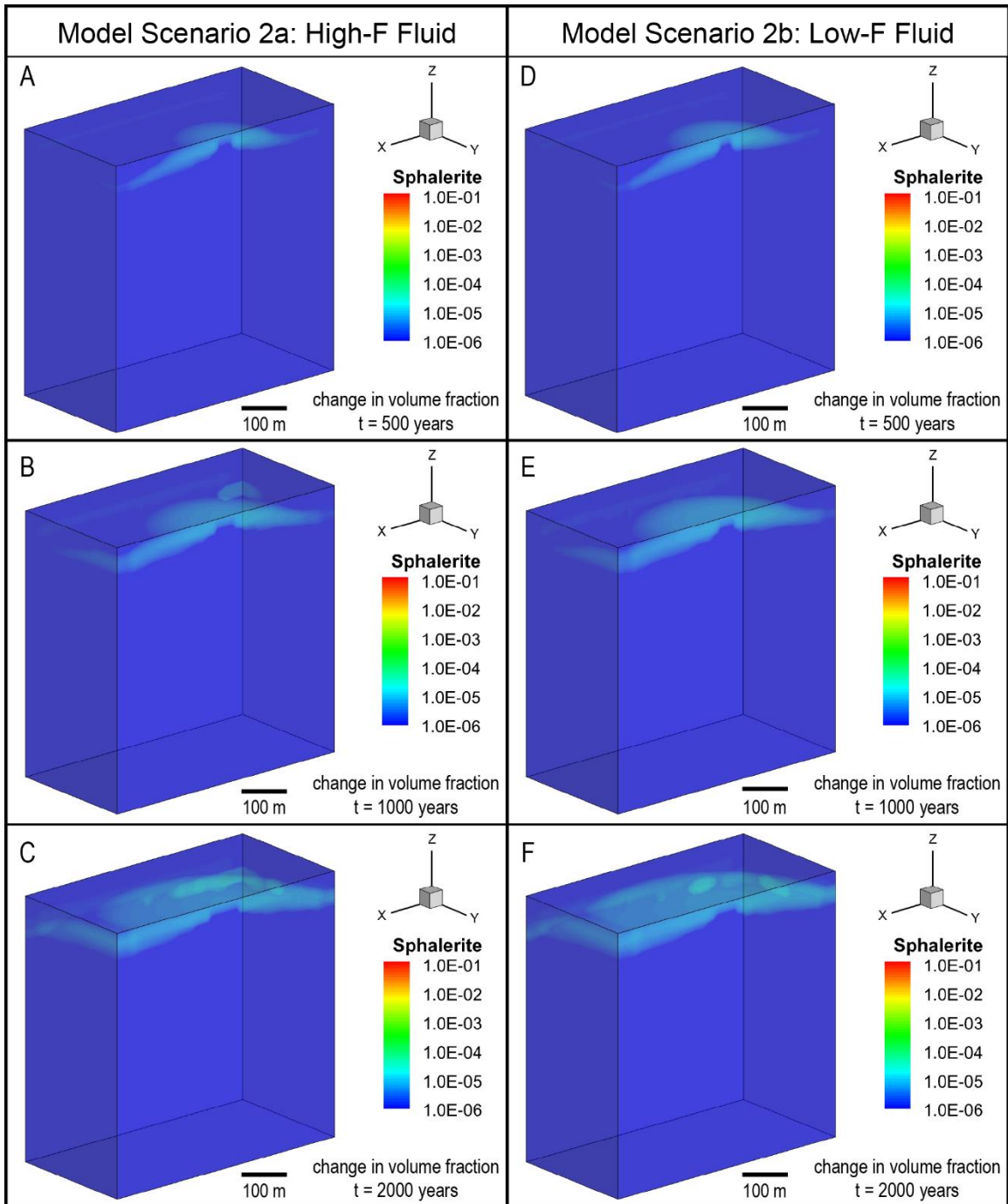
Figure 3-15. Simulated change in sphalerite volume fraction for Model Scenario 2a after (A) 500 years, (B) 1000 years, and (C) 2000 years, and for Model Scenario 2b l after (D) 500 years, (E) 1000 years, and (F) 2000 years.

fractions reached in Model Scenario 2 are several orders of magnitude lower than those reached in Model Scenario 1. The apparent inefficiency of fluid mixing as a sulfide mineral precipitation mechanism in Model Scenario 2 as compared with Model Scenario

1 is likely, at least in part, an artifact of the structure of the numerical model. Model Scenario 1 provides a constant flux of reduced sulfide into the model domain through the fault fluid; however, Model Scenario 2 has no mechanism to replenish sulfide as it is removed by sulfide mineral precipitation. Therefore, the high-sulfide fluid acts as an initial sulfide package that is consumed over time placing an artificial upper limit on total sulfide mineral precipitation. Sulfide mineral concentrations would likely be higher with addition of a sulfide source in the upper portion of the model domain.

3.6 Discussion

3.5.1 Uncertainties and limitations

The models were designed to test general concepts of ore formation without considering detailed geologic heterogeneities in structure, sedimentary facies, mineral composition, porosity, or permeability. Therefore, the results of the models are correspondingly general, producing highly averaged outcomes for the model scenarios posed. Further, the values of most of the model parameters are not well known, creating additional generality and uncertainty in the models. In particular, the permeabilities of the rock units at the time of ore formation are unknown and those used in the models were at the low end of the range of typical values for limestone (Ingebritsen and Appold, 2012) in order to promote model stability. Thus, the actual field permeabilities could have been orders of magnitude higher. Additionally, the regional hydraulic head gradient at the time of ore formation may have differed by an order of magnitude from the model value of 0.01 and the fluid pressure at the base of the fault may have differed significantly from the model value of 75% of lithostatic pressure. Because fluid velocity is directly proportional to permeability and hydraulic head or pressure gradient, the fluid

flow rates calculated in the models could be orders of magnitude different from the actual flow rates at the time of ore formation. Significant uncertainties also exist in ore fluid composition. Although the major element (Na, Ca, K, Mg, Cl), F, Zn, and Ba concentrations in Illinois-Kentucky ore fluids have been reported (Pelch et al., 2015; Kenderes and Appold, 2017; Smith-Schmitz and Appold, 2018), concentrations of other key ore constituents, Pb and S, have not yet been determined, adding to uncertainties in model predictions of the amounts of sulfide mineral precipitation.

3.5.2 Comparison of model results to field observations

Despite the uncertainties in the model input parameters and the highly averaged nature of the results, the models provide some important insights into the origin of the Illinois-Kentucky MVT deposits. In particular, the models show the importance of high F concentrations in the fault fluid to ore formation, as the models that had high F concentrations in the fault fluid (Models 1a and 2a) produced results that fit field observations more closely than models that had low F concentrations (Models 1b and 2b). These findings support the long-standing genetic hypothesis for the Illinois-Kentucky district of mixing between resident sedimentary brine and a deeply sourced magmatic F-rich fluid rising along faults (Hall and Friedman, 1963; Heyl et al., 1966; Grogan and Bradbury, 1968; Hall and Heyl, 1968; Plumlee et al., 1995; Denny et al., 2015), and corroborate the studies by Kenderes and Appold (2017) and the present author (Chapter 2 of this dissertation) that reported high F concentrations in fluid inclusions from Illinois-Kentucky.

For example, the low pH associated with high F concentration in Model Scenarios 1a and 2a caused intense calcite dissolution (greater than 50% of calcite dissolved)

localized in the Ste. Genevieve Limestone where it intersects the fault. This is in general

agreement with field observations of significant calcite dissolution having occurred

during fluorite mineralization (e.g. Becke, 1962; Grogan and Bradbury, 1968; Denny et

al., 2013). Field observations also show the degree of calcite dissolution to vary widely

with location in the Illinois-Kentucky deposits. However, high-grade fluorite

mineralization is observed to correlate strongly with intense calcite dissolution, which

can reach 100% within the ore bodies. Likewise, in the high F models, the areas of

greatest fluorite precipitation correlate with the areas of greatest calcite dissolution. This

further agrees with the observation that most fluorite mineralization in Illinois-Kentucky

occurs as direct replacement of either early ore-stage calcite, of host rock limestone along

bedding planes, or of limestone host rock immediately adjacent to faults and fractures

(Grogan and Bradbury, 1968).

Another similarity between the high-F models and field observations is calcite dissolution significantly in excess of fluorite precipitation, as indicated by increase in porosity (Fig. 3-10C). In the Illinois-Kentucky deposits, dissolution features associated with ore bodies (Fig. 3-16) such as the thinning of limestone beds, softening of impure limestone beds,

Figure 3-16. Slumping due to limestone dissolution associated with a fluorite ore body at the Hastie Quarry. Adits mark the approximate lateral extent of the ore body. Photograph credit: Martin Appold

crystal-lined cavities, and fluorite cemented breccia indicate that ore stage limestone dissolution exceeded replacement by fluorite (Becke, 1962; Grogan and Bradbury, 1968; Denny et al., 2013). Limestone loss due to dissolution may account for as much as 75% of the thinning associated with high-grade ore bodies, where volume loss due to replacement of limestone with fluorite accounts for the remaining 25% (Brecke et al., 1962). The calcite dissolution pattern predicted by the high-F models most strongly resembles breccia pipes observed in the field, where intense calcite dissolution in pipe like structures leads to up to 10 m of collapse in the overlying strata (Brecke et al., 1962). In contrast to the high-F models, the low-F models predict only very minor calcite dissolution (less than 1%) after 2000 years.

Further support for the role of F-rich fluids in the formation of the Illinois-Kentucky deposits comes from model ore formation rates, particularly, the rate of increase of fluorite grade. On average, fluorite grades range between 30 and 40% (Denny et al., 2013). However, in some large ore bodies, average fluorite grades reach 50 to 60% and locally within smaller parts of the deposits up to 95%. Figure 3-16 shows how the grade of fluorite changes as a function of time in the high-F and low-F models in a grid cell located adjacent to the fault in the Ste. Genevieve Limestone (Fig. 3-4). Both high-F models (1a and 2a) predicted fluorite to reach a grade of 30 wt% in the Ste. Genevieve Limestone adjacent to the fault after 1600 years and 72% after 2000 years. In contrast, in both low-F models (2a and 2b), fluorite reaches a grade of only about 3×10^{-6} wt% after 2000 years, meaning that at that rate of accumulation 20 billion years would be needed to reach the district average fluorite ore grade of 30 wt%. Due to the uncertainties in model parameters described above, the absolute times required to produce ore grade fluorite is

corresponding uncertain. However, the results of the models show that a fluid containing the high F concentrations reported by Kenderes and Appold (2017) is several orders of magnitude more efficient at producing ore grade fluorite bodies than a fluid having the much lower F concentrations typical of sedimentary brines. The greater efficiency of fluorite ore formation in the high-F models is attributable to both higher rates of fluorite precipitation and to dissolution of calcite due to the low pH of the fluid. At lower fluorite grades up to 20 wt%, the predicted grade was primarily controlled by the amount of fluorite precipitated. However, at higher grades, dissolution of calcite contributed more to the grade than the total precipitated fluorite.
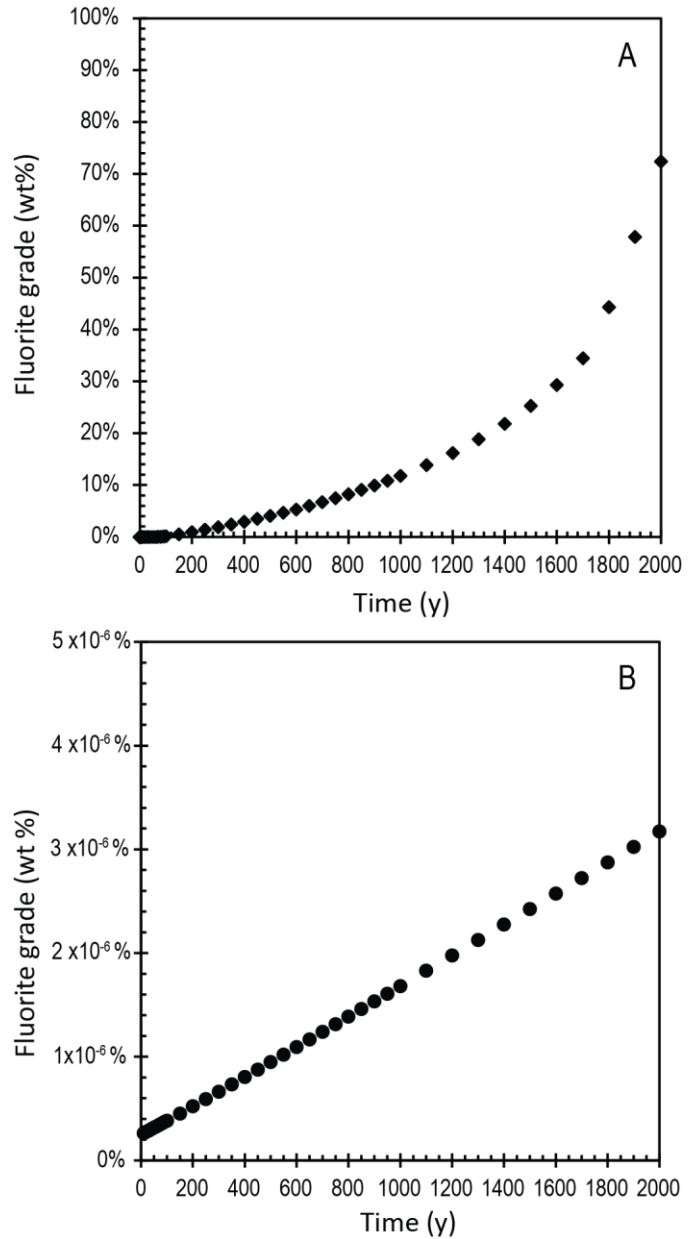
Figure 3-17. Fluorite grade as a function of time in a grid cell in the Ste. Genevieve Limestone immediately adjacent to the fault (see yellow highlighted cell in Figure 3-4) as predicted in (A) and the high-F model scenarios (1a and 2a), and (B) the low-F model scenarios (1b and 2b).

The 2000 year duration of the model simulations presented in this study are relatively brief and probably represent an individual pulse of fluid flow ascending a fault in the district, where many such pulses likely occurred episodically, based on the multiple fluorite growth stages evident in the district's paragenetic sequence. Individual fluorite ore bodies in the Illinois-Kentucky district range in size from 2 to 470 kilotonnes (kt). The present models suggest that an individual, 2000 year long pulse of fluid could have deposited 2.3 kt of fluorite. Thus, the smallest ore bodies in the Illinois-Kentucky district could have been formed by a single pulse of high F fluid ascending a major fault and the largest ore bodies could have been formed by around 200 such pulses. The duration of ore formation in the Illinois-Kentucky district is not yet known. However, Ingebritsen et al. (2006) estimate that most magmatic hydrothermal fluid systems have lifespans of order 10^4 to 10^6 years. Thus, if the magmatic hydrothermal system that provided F-rich fluid to the Illinois-Kentucky district had a lifespan near the upper end of this 10^4 to 10^6 year range, then this could have been long enough to allow enough fluid pulses to form even the largest ore deposits in the district.

3.7 Conclusions

The results of the present study support the hypothesis that the fluorite-dominant MVT deposits in the Illinois-Kentucky district were formed from F-rich fluids that ascended along faults. In addition, the study reached the following, more specific, conclusions:

1. The models predict that an acidic, F-rich fluid can ascend a silicified fault that crosscuts several layers limestone without being neutralized as long as the fluid remains within the fault. Small amounts of the F-rich fluid are predicted to

diffuse outward from the fault as the fluid ascends. However, most of the fluid will exit the fault where it intersects a high permeability aquifer.

2. The models predict that the high-F fluid is rapidly neutralized by reaction with calcite upon exiting the fault into the limestone aquifer. The neutralization of the high-F fluid results in locally intense limestone dissolution at the intersection of the fault with the limestone aquifer.

3. The high-F models predict high-grade fluorite precipitation that is limited to within a few meters of the fault and reaches up to 0.2 volume fraction change in the permeable layers and up to 0.05 in the underlying limestone layers after a pulse of 2000 years.

4. The models indicate that an acidic, high-F ore fluid enhances fluorite grade both through higher rates of fluorite precipitation and through higher rates of calcite dissolution.

5. The models indicate that a low-F ore fluid with a pH of 4, more typical of MVT ore forming fluids, does not produce a fluorite dominant ore assemblage like that observed in Illinois-Kentucky. In addition, the low-F ore fluid models are inefficient for fluorite ore formation, requiring billions of years to reach typical Illinois-Kentucky district ore grades.

6. For models in which Pb, Zn, and sulfide are transported in a single fluid, the results indicate that the high-F ore fluid has the potential to enhance sulfide mineral precipitation efficiency by several orders of magnitude over that of more typical MVT ore fluid. Models in which sulfide mineral precipitation occurs due to the mixing of a metal-poor, sulfide-rich fluid with a metal-rich, sulfide-poor

fluid do not predict a similar increase in efficiency for the high-F vs. the low-F ore fluid models. The relative inefficiency of the two brine models vs. the single resident brine models with respect to sulfide mineralization is likely an artifact of the numerical model structure.

The results from the models highlight the importance of an F-rich, acidic fluid in forming fluorite-dominant ore bodies in the Illinois-Kentucky district. The results from the high-F models are in better agreement with field observations than the low-F models, i.e. the spatial distribution of fluorite ore, the association of limestone dissolution features with fluorite mineralization, and the greater abundance of fluorite mineralization compared to other MVT ore minerals. In addition, the high-F models predict rates of ore formation that are orders of magnitude greater than those predicted by the low-F models. Thus, the models support the F-rich, acidic ore fluid genetic hypothesis for ore formation in the Illinois Kentucky MVT district.

3.8 References

Appold, M. S., 2021. Applications of fluid inclusions to studies of sediment-hosted base metal ore deposits: case studies from the central U.S.A. and Brazil. In *Mineral. Assoc. Can. Short Course*, **49**, 47–72.

Bastin E. S., Behre C. H., Fowler G. M., Giles A. W., Kay G. M., Landes K. K., Lyden J. P., McFarlan A. C., McKnight E. T., Moore R. C., Ridge J. D., Robinson L. C., Tarr W. A., Tolman C. and Weidman S. eds., 1939. Contributions to a knowledge of the lead and zinc deposits of the Mississippi Valley region. *Spec. Pap. - Geol. Soc. Am.*, **156**.

Baxter J. W. and Bradbury J. C., 1989. The Illinois-Kentucky fluorspar mining district. In *Precambrian and Paleozoic Geology and Ore Deposits in the Midcontinent Region: Rosiclare, Illinois to Ironton and Viburnum, Missouri: June 30–July 8, 1989* (eds. J. W. Baxter, E. B. Kisvarsanyi, R. D. Hagni, J. C. Bradbury, P. E. Gerdemann, and J. M. Gregg). 3–36.

Baxter J. W., Bradbury J. C., Hester N. C., Clare R. and County H., 1973. A geologic excursion to fluorspar mines in Hardin and Pope counties, Illinois eds. J. W. Baxter, J. C. Bradbury, and N. C. Hester. *Guideb. Ser. - Illinois State Geol. Surv.* **11**, 1–30.

Bradbury J. C. and Baxter J. W., 1992. Intrusive breccias at Hicks Dome, Hardin County, Illinois. *Circ. - Illinois State Geol. Surv.* **550**.

Brannon J. C., Leach D. L., Goldhaber M. B., Taylor C. D. and Livingston E., 1997. Radiometric dating of ore-stage calcite from Knight Vein, IL-KY-fluorspar district, yields 195 Ma for both U-Pb and Th-Pb systems. *Abstr. with Programs - Geol. Soc. Am.* **29**, 209.

Brecke E. A., 1962. Ore Genesis of the Cave-in-Rock Fluorspar District, Hardin County, Illinois. *Econ. Geol.* **57**, 499–535.

Brown J. S., Emery J. A. and Meyer P. A., 1954. Explosion pipe in test well on Hicks Dome, Hardin County, Illinois. *Econ. Geol.* **49**, 891–902.

Denny F. B., 2005. The Cottage Grove dike and mafic igneous intrusions in southeastern Illinois and their relation to regional tectonics and economic resources. Southern Illinois University.

Denny F. B., Devera J. A., and Kittler A., 2013. *Bedrock geology of Saline Mines Quadrangle, Gallatin and Hardin Counties, Illinois* (eds. F. B. Denny, J. A. Devera, and A. Kittler). Illinois Geol. Quadrang. Map, 1–10.

Denny F. B., Guillemette R. N. and Lefticariu L., 2015. Rare earth mineral concentrations within fluorite in the Illinois-Kentucky Fluorite District and

igneous intrusives at Hicks Dome crypto-explosive complex, southern Illinois and northwestern Kentucky (USA). *Circ. - Illinois State Geol. Surv.* **587**, 16.

Domenico, P. A., and Schwartz, F. W., 1998. *Physical and chemical hydrogeology* (506 p.). New York: Wiley.

Fifarek R. H., Denny F. B., Snee L. W. and Miggins D. P., 2001. Permian igneous activity in southeastern Illinois and western Kentucky; implications for tectonism and economic resources. *Abstr. with Programs - Geol. Soc. Am.* **33**, 420.

Fuhrmann G. D., 1994. Regional fluid inclusion study of the Illinois-Kentucky fluorspar district. Iowa State University of Science and Technology.

Goldstein A., 1997. The Illinois-Kentucky fluorite district ed. A. Goldstein. *Mineral. Rec.* **28**, 3- 49.

Grogan R. M. and Bradbury J. C., 1968. Fluorite-zinc-lead deposits of the Illinois-Kentucky mining district. In *Ore deposits of the United States, 1933-1967*. 370–399.

Hall W. E. and Friedman I., 1963. Composition of fluid inclusions, Cave-in-Rock fluorite district, Illinois, and Upper Mississippi Valley zinc-lead district. *Econ. Geol.* **58**, 886–911

Hall, W. E., and Heyl, A. V., 1968. Distribution of minor elements in ore and host rock, Illinois-Kentucky fluorite district and Upper Mississippi Valley zinc-lead district. *Econ. Geol.* **63**, 655-670.

Hanor, J. S., 1996. Controls on the solubilization of lead and zinc in basinal brines. *Carbonate-hosted Lead–Zinc Deposits, SEG Special Publication: USA*, **4**, 483-500.

Heyl, A. V., Delevaux, M. H., Zartman, R. E., and Brock, M. R., 1966. Isotopic study of galenas from the upper Mississippi Valley, the Illinois-Kentucky, and some Appalachian Valley mineral districts. *Econ. Geol.* **61**, 933-961.

Ingebritsen, S. E., and Appold, M. S., 2012. The physical hydrogeology of ore deposits. *Econ. Geol.* **107**, 559-584.

Ingebritsen, S.E., Sanford, W.E. and Neuzil, C.E., 2006, *Groundwater in geologic processes*. Cambridge University Press, 536 p.

Kenderes, S. M., and Appold, M. S., 2017. Fluorine concentrations of ore fluids in the Illinois-Kentucky district: Evidence from SEM-EDS analysis of fluid inclusion decrepitates. *Geochim. Cosmochim. Acta*, **210**, 132-151.

Moorehead A., 2013. Igneous intrustions at Hicks Dome, southern Illinois, and their relationship to fluorine-base metal-rare earth element mineralization. Southern Illinois University.

Nelson, W. J., 1995. Bedrock geology of the Paducah 1 X 2 quadrangle, Illinois, Kentucky, and Missouri. *Bulletin no. 102*. Nelson W. J. and Lumm D. K., 1984. Structural geology of southeastern Illinois and vicinity. *Contract. Rep. - Illinois. Geol. Surv. Div.*, **127**.

Nelson, W.J., Lumm, D.K., 1984. *Structural Geology of Southeastern Illinois and Vicinity: Illinois. Geol. Surv.* ISGS Contract Grant Report 1984-2, 127 p.

Pelch, M. A., Appold, M. S., Emsbo, P., and Bodnar, R. J., 2015. Constraints from fluid inclusion compositions on the origin of Mississippi Valley-type mineralization in the Illinois-Kentucky district. *Econ. Geol.* **110**, 787-808.

Plumlee G. S., Goldhaber M. B. and Rowan E. L., 1995. The potential role of magmatic gases in the genesis of Illinois-Kentucky fluorspar deposits; implications from chemical reaction path modeling. *Econ. Geol.* **90**, 999–1011.

Potter C. J., Goldhaber M. B., Heigold P. C. and Taylor C. D., 1992. Regional seismic reflection line, southern Illinois Basin, provides new data on Cambrian rift geometry, Hicks Dome genesis, and the Fluorspar area fault complex. *Abstr. with Programs - Geol. Soc. Am.* **24**, 279.

Reynolds R. L., Goldhaber M. B. and Snee L. W., 1997. Paleomagnetic and 40Ar/39Ar results from the Grant intrusive breccia and comparison to the Permian Downeys Bluff sill evidence for Permian igneous activity at Hicks Dome, Southern Illinois Basin. *US Geol. Surv. Bull.* **n 2094 G**.

Richardson C. K. and Pinckney D. M., 1984. The chemical and thermal evolution of the fluids in the Cave-in-Rock fluorspar district, Illinois: Mineralogy, paragenesis, and fluid inclusions. *Econ. Geol.* **79**, 1833–1856.

Ruiz P. J., Richardson C. K. and Patchett P. J., 1988. Strontium 630 isotope geochemistry of fluorite, calcite, and barite of the Cave-in-Rock fluorite district, Illinois. *Econ. Geol.* **83**, 203–210.

Smith-Schmitz, S. E., and Appold, M. S., 2018. Prediction of ore fluid metal concentrations from solid solution concentrations in ore-stage calcite: Application to the Illinois-Kentucky and Central Tennessee Mississippi Valley-type districts. *Geochim. Cosmochim. Acta*, **225**, 210-227.

Snee L. W. and Hayes T. S., 1992. 40Ar/39Ar geochronology of intrusive rocks and Mississippi valley-type mineralization and alteration from the Illinois-Kentucky fluorspar district. In *Open-File Report - U. S. Geological Survey* (eds. M. B. Goldhaber and J. J. Eidel). 59 - 60.

Spry P. G. and Fuhrmann G. D., 1994. Additional fluid inclusion data for the Illinois-Kentucky fluorspar district; evidence for the lack of a regional thermal gradient. *Econ. Geol.* **89**, 288–306.

Spry P. G., Koellner M. S., Richardson C. K. and Jones H. D., 1990. Thermochemical changes in the ore fluid during deposition at the Denton Mine, Cave-in-Rock fluorspar district, Illinois. *Econ. Geol.* **85**, 172–181.

Sverjensky D. A., 1984. Oil field brines as ore-forming solutions. *Econ. Geol.* **79**, 23–37.

Symons D. T. A., 1994. Paleomagnetism and the late Jurassic genesis of the Illinois-Kentucky fluorspar deposits. *Econ. Geol.* **89**, 438–449.

Trace, R. D., and Amos, D. H., 1984. *Stratigraphy and structure of the western Kentucky fluorspar district* (No. 1151-D).

Xu, T., Spycher, N., Sonnenthal, E., Zhang, G., Zheng, L., and Pruess, K., 2011. TOUGHREACT Version 2.0: A simulator for subsurface reactive transport under non-isothermal multiphase flow conditions. *Comp. Geosci.*, **37**, 763-774.

Yancey R. J., 1995. Geology of the Illinois-Kentucky fluorspar district ed. K. C. Misra. *Carbonate-hosted lead-zinc-fluorite-barite Depos. North Am.* **22**, 160–172.

Zartman R. E., Brock M. R., Heyl A. V. and Thomas H. H., 1967. K-Ar and Rb-Sr ages of some alkalic intrusive rocks from central and eastern United States. *Am. J. Sci.* **265**, 848–870.

Chapter 4: Experimental Determination of Partition Coefficients for Zn between Dolomite and Aqueous Solution

4.1 Abstract

The concentration of Zn in ore-forming fluids is a fundamental question in the study of sediment hosted Zn-Pb deposit formation. Numerous studies have been undertaken with the goal of directly measuring Zn in fluid inclusions. However the results of many of these studies have been equivocal. Uncertainty exists as to whether elevated Zn signals in fluid inclusions arise from true aqueous solute or from minute accidental metal sulfide mineral inclusions entrained in the fluid inclusion at the time of mineral precipitation. Element partitioning theory provides an alternate means of determining ore fluid Zn concentrations from solid solution Zn concentrations in a coeval mineral. Dolomite is commonly an ore-stage mineral in sediment hosted Zn-Pb deposits and is known readilyto rincorporate Zn into its crystalline lattice, where Zn primarily substitutes for Mg. Therefore, dolomite has great potential to be used to determine aqueous Zn concentrations using element partitioning theory. This potential cannot be realized due to a lack of experimental partition coefficients (D) for the partitioning of Zn between dolomite and aqueous solution.

The present study was undertaken with the goal of determining experimental partition coefficients for the partitioning of Zn between aqueous solution and dolomite under typical sediment hosted Zn-Pb ore formation conditions. To this end, a series of dolomite precipitation experiments was performed at temperatures of 200, 150, and 125° C, pressures of 10 MPa and the saturation pressure of the aqueous solution, and Zn concentrations of 10, 100, and 1000 ppm. Powder X-ray diffraction (PXRD) of the

mineral precipitates indicates that the primary product of all of the experiments is dolomite, however peak broadening in the data from the 125° C and the 10 day, 150° C experiments indicates that those dolomite precipitates are not as fully ordered as the precipitates from the other experiments. Laser ablation-inductively coupled plasma-mass spectrometry (LA-ICP-MS) was used to measure the elemental compositions of the precipitates and the composition of the coeval fluids were measured using inductively coupled plasma-atomic emission spectroscopy (ICP-AES) or inductively coupled plasma – mass spectrometry (ICP-MS). The measured Zn/Mg ratios in the precipitates and in the fluids were used to calculate D values. An equilibrium D value of 75±10 was determined for 200° C. The D values from the 150 and 125° C experiments were not determined to have reached equilibrium, however the trend in D values from these experiments clearly indicates that they are lower than the 200° C D value.

4.2 Introduction

Sediment hosted Zn-Pb deposits represent the most abundant Zn and Pb resources worldwide, both in terms of metal production and in terms of total reserves (Leach et al., 2005). The role of sedimentary brines in forming these deposits has been widely recognized (e.g. Sverjenski, 1984; Kesler et al., 1996, Leach et al., 2010). A fundamental question regarding the formation of these deposits is the concentrations of Zn and Pb in the ore forming fluids, as these concentrations have significant implications for the mechanism and efficacy of ore formation. A long-standing hypothesis is that the formation of large, sediment-hosted base metal deposits was driven in part by ore fluids that were anomalously metal rich relative to typical sedimentary brines (e.g. Wilkinson et

al., 2009; Pelch et al., 2015; Smith-Schmitz and Appold, 2018), which typically have Zn and Pb concentrations on the order of tenths to 10s of ppm (Hanor, 1996; Yardley, 2005).

However, significant uncertainty remains with respect to the metal compositions of sediment hosted Zn-Pb ore fluids and if they were enriched in metals relative to typical sedimentary brines (Wilkinson et al. 2009; Pelch et al., 2015; Smith-Schmitz and Appold, 2018). A number of studies have been undertaken with the goal of determining the Zn concentrations of sediment hosted Zn-Pb ore fluids. Many of these studies have focused on directly measuring the Zn concentrations in fluid inclusions hosted in ore-stage minerals from the Mississippi Valley-type (MVT) subclass of sediment hosted Zn-Pb deposits (Czamanske et al., 1963; Pinckney and Haffty, 1970; Appold et al., 2004; Wilkinson et al., 2005; Stoffell et al., 2008; Wilkinson et al., 2009; Appold and Wenz, 2011; Wenz et al., 2012; Hammerli et al., 2013; and Pelch et al., 2015). Czamanske et al. (1963) and Pinckney and Haffty (1970) extracted fluids for analysis from fluorite and ore-stage quartz samples from the Illinois-Kentucky MVT district for analysis using bulk crush leachate methods. These studies reported Zn concentrations up to 10,900 ppm for the Illinois-Kentucky district. However, the use of bulk crush leachate to extract fluids for analysis is problematic, and the data collected via this method is suspect. First, the fluid extracted is a mixture of the contents of multiple fluid inclusions that may represent multiple generations of fluids including post ore fluids, making the metal concentrations measured in the leachate unreliable. Second, the process of crushing the minerals to extract the fluids can result in contamination of the fluids by minute sulfide mineral inclusions in the host mineral matrix. This type of contamination could result in excessively high base metal concentrations when the fluids are analyzed. Wilkinson et

al. (2005) used inductively coupled plasma-atomic emission spectroscopy (ICP-AES) to perform analysis of bulk fluid inclusion decrepitates hosted in quartz from quartz-carbonate-sulfide veins in the Irish Midlands Zn-Pb deposits to determine ore fluid Zn concentrations of 3 to 6 ppm. As with bulk crush leachate methods, the bulk analysis of fluid inclusion decrepitates is problematic as the extracted fluids may represent multiple fluid generations and is therefore unreliable.

More recently, research undertaken to determine Zn and Pb concentrations in MVT ore-forming fluids has focused on the use of laser ablation-inductively coupled plasma-mass spectrometry (LA-ICP-MS) to measure the metal contents of ore-stage fluid inclusions *in situ* (e.g. Appold et al., 2004; Stoffell et al.,2008; Wilkinson et al., 2009; Appold and Wenz, 2011; Wenz et al., 2012; Hammerli et al., 2013; and Pelch et al., 2015). These studies have reported Zn and Pb concentrations on the order of 1's to a few 10's of ppm for gangue mineral hosted fluid inclusions (i.e. those found in dolomite, calcite, or quartz), values typical of sedimentary brines. In contrast, Zn and Pb concentrations for fluorite and sphalerite hosted fluid inclusions, the main transparent ore minerals useable for LA-ICP-MS analyses, were reported to be more variable with concentrations up to 1000's of ppm, orders of magnitude greater than those typical for sedimentary brines. However, concentrations of Zn and Pb determined using fluid inclusion analysis can be ambiguous (Pelch et al., 2015; Smith-Schmitz and Appold, 2018). Metals present in solid solution or in mineral inclusions in the host mineral matrix can cause interference, preventing reliable quantification of these metals in fluid inclusions using LA-ICP-MS. Uncertainty also exists as to whether elevated Zn and Pb signals in LA-ICP-MS represent true aqueous solutes or instead represent accidental

mineral inclusions (Roedder, 1984; Hammerli et al., 2013; Appold, 2021), i.e. fragments of earlier precipitated Zn or Pb bearing minerals entrained within the fluid inclusion at the time of the fluid inclusions' formation.

Determination of the ore fluid Zn concentrations via fluid inclusion analysis in another major subclass of sediment hosted Zn-Pb depsoits, sedimentary exhalative (SEDEX) deposits, has been hampered in part by the very fine texture of the ores (Leach et al., 2005; Emsbo et al., 2016; Manning and Emsbo, 2018). The few published fluid inclusion studies of SEDEX district have primarily reported microthermometry data (Gardner and Hutcheon, 1985; Ansdell et al., 1989; Bresser, 1992; Leach et al., 2004; Polito et al., 2006). Leach et al. (2004) also reported major element compositions for the Red Dog Zn-Pb-Ag district ore fluids measured using bulk leachate analysis of sphalerite-hosted fluid inclusions. Because ore fluid Zn concentrations have not been directly measured, estimates of the Zn concentrations in SEDEX ore fluids have been limited to numerical modeling of hydrothermal fluids and their efficacy for ore formation, which suggests a minimum of about 10 ppm Zn (Emsbo et al., 2016; Manning and Emsbo, 2018).

Element partitioning theory provides an alternate method that can be used to calculate the metal concentration in the ore fluid from the metals' trace solid solution concentrations in ore-stage minerals (e.g. Holland, 1956; van Hinsberg et al., 2010). Use of element partitioning theory requires knowledge of either a thermodynamic distribution coefficient (K_D) or an empirical partition coefficient (D), and knowledge of the concentration of a major element in the mineral and the coeval fluid. Values of K_D and D have been published for the partitioning of Zn, Pb, and Fe between water and calcite

110

(McIntire, 1963; Tsusue and Holland, 1966; Morse and Bender, 1990; Rimstidt et al., 1998). Smith-Schmitz and Appold (2018) evaluated these K_D and D values and used them to determine Zn and Fe concentrations of no more than 10s of ppm in the ore fluid that formed the Illinois-Kentucky and Central Tennessee MVT districts. These concentrations are typical of sedimentary brines (e.g. Hanor, 1996; Yardley, 2005). Carbonate gangue mineralization is characteristic of the MVT and other sediment-hosted base metal deposits. However, in many sediment-hosted Zn-Pb districts, calcite does not overlap with sulfide mineralization, limiting the usefulness of calcite for determining ore-stage metal concentrations in the mineralizing fluids. Dolomite, like calcite, is known to incorporate Zn and Pb into its crystal lattice and is commonly ore-stage in MVT deposits (e.g. Hagni and Grawe, 1964; Jolly and Heyl, 1964; McCormick et al., 1971; Sverjensky, 1981) and, to a lesser extent, in SEDEX deposits (Embro et al., 2016), making dolomite potentially more useful for determining Zn and Pb concentrations in mineralizing fluids.

A theoretical partition coefficient (K_D) of 6.85 for the partitioning of Zn between aqueous solution and dolomite at 75° C was estimated by Wogelius et al. (1992). However, the accuracy of this value is unclear as the thermodynamic data for minrecordite ($CaZn(CO_3)_2$ with the dolomite structure) has not been published. In addition, a thorough search of the literature did not yield any experimental partition coefficients (D) for the partitioning of Zn between dolomite and aqueous solution that could provide a check on the validity of the estimated K_D value. Thus, the potential for using element partitioning theory as a means of determining ore fluid Zn concentrations from Zn measured in dolomite cannot be realized.

This study, therefore, was undertaken with the goal of determining a suite of D values for the partioning of Zn between aqueous solution and dolomite at temperatures (125, 150, and 200° C), pressures (10 MPa and the saturation pressure of water), and salinities (18 weight percent total dissolved solids) typical of sediment hosted Zn-Pb deposit formation. To this end, dolomite was precipitated directly from aqueous solution under these conditions. The Zn/Mg ratios measured in the dolomite precipitates and the fluids from which they were precipitated were then used to calculate D values.

4.3 Methodology

4.3.1 Element Partitioning

Zinc in dolomite primarily substitutes for Mg in the M_1 site as is evidenced by the inverse proportionality of Zn and Mg measured in naturally occurring high Zn dolomites (e.g. Garavelli et al., 1982; Chang et al., 1996; Boni et al., 2011). The strong preference of Zn for substituting for Mg in the M_1 site in ordered dolomite over substituting for Ca in the M_2 site is likely due to the similarity in ionic radii of Zn^{2+} and Mg^{2+} (Zn^{2+} = 0.74 Å, Mg^{2+} = 0.72 Å, Δ = 0.02 Å; Shannon, 1976), as opposed to the much greater difference between Zn^{2+} and Ca^{2+} (Ca^{2+} = 1.0 Å, Δ = 0.26 Å). This is part of a larger pattern of enhanced substitution between similarly sized ions Mg^{2+}, Zn^{2+}, Mn^{2+}, and Fe^{2+} in carbonates that has been discussed in detail by Reeder(2018). In addition, solid solution between Zn and Mg in $Ca(Zn,Mg)(CO_3)_2$ with the dolomite structure is extensive and has been calculated as being stable up to an atomic Zn content of 90% (Rosenberg and Foit, 1979). Therefore, it is reasonable to treat all Zn in solid solution in dolomite as substituting for Mg.

The distribution coefficient for Zn between aqueous solution and dolomite can then be derived as follows. Dolomite precipitation primarily occurs according to the following reaction

$$Ca^{2+}_{(aq)} + Mg^{2+}_{(aq)} + 2CO^{2-}_{3(aq)} \rightleftharpoons CaMg(CO_3)_{2(dol)} \qquad (4\text{-}1)$$
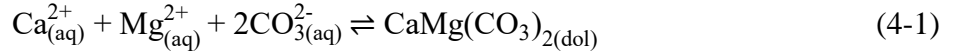
Base metals like Zn may be incorporated into solid solution in dolomite according to reactions like

$$Ca^{2+}_{(aq)} + Zn^{2+}_{(aq)} + 2CO^{2-}_{3(aq)} \rightleftharpoons CaZn(CO_3)_{2(dol)} \qquad (4\text{-}2)$$
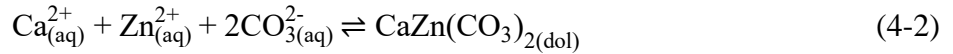
Reactions (2) and (3) can be combined, leading to

$$Zn^{2+}_{(aq)} + CaMg(CO_3)_{2(dol)} \rightleftharpoons Mg^{2+}_{(aq)} + CaZn(CO_3)_{2(dol)} \qquad (4\text{-}3)$$
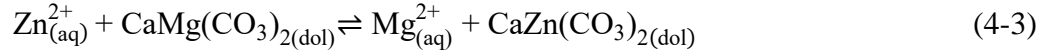
From reaction (4) the following mass action expression can be written

$$D = \frac{m^{Mg^{2+}} X^{CaZn(CO_3)_2}_{dol}}{m^{Zn^{2+}} X^{CaMg(CO_3)_2}_{dol}} \qquad (4\text{-}4)$$

where m^i represents molal concentration of the metal in aqueous solution and X^i represents mole fraction of the metal in dolomite.

The mass action expression (4-4) was used to calculate D values in this study from the molal concentrations of Zn^{2+} and Mg^{2+} measured in dolomite precipitates and in the aqueous solutions from which the dolomite was precipitated. Speciation calculations of the fluids were completed using Geochemist Workbench® (Bethke, 2004) in order to determine aqueous Zn^{2+} and Mg^{2+} from the bulk Zn and Mg concentrations measured in the fluids. Zinc and magnesium in the dolomite were assumed to behave ideally based on the nearly complete solid solution between Zn and Mg in dolomite and the relatively low concentrations of Zn in solid solution in the precipitated dolomites.

4.3.2 Dolomite precipitation

The method of dolomite precipitation used in this study was modified from the method used by Rodriguez-Blanco et al. (2015), who showed that at temperatures above 100° C the crystallization of ordered dolomite is facilitated by precipitating fluids that are highly supersaturated with respect to dolomite as indicated by the dolomite saturation index (SI)

$$SI = \log \frac{a^{Zn^{2+}} a^{Mg^{2+}} \left(a^{CO_3^{2-}}\right)^2}{K_{sp}} \qquad (4\text{-}5)$$

with *a* representing the activity of the Ca^{2+}, Mg^{2+}, and CO_3^{2-} ions in the solution and *Ksp* representing the solubility product of dolomite (Robie et al. 1978).

The dolomite precipitation experiments were carried out by mixing two precursor solutions, a metal (Ca, Mg, and Zn) bearing solution and a separate carbonate bearing solution, in a reaction vessel to produce model ore fluid solutions (Table 4-1) that were supersaturated with respect to dolomite. The solutions were prepared using MilliQ ultra high purity water with electrical resistivity of 18 MΩ*cm, ACS reagent grade $CaCl_2*2H_2O$, $MgCl_2*6H_2O$, KCl, $Zn(CH_3COO)_2*2(H_2O)$, $NaCO_3$, and NaCl. The model ore fluid solutions had initial Na, K, Ca, and Cl concentrations based on the average major element composition of MVT ore fluids in the U.S. mid-continent as reported by Wenz et al. (2012), and Zn concentrations of approximately 10, 100, and 1000 ppm. Early experiments produced significant quantities of calcite precipitates that were highly intergrown with dolomite precipitates. Therefore initial model solution Mg concentrations were adjusted to maximize the precipitation of dolomite while minimizing the co-precipitation of undesired carbonate minerals.

Table 4-1. Experimental conditions and initial compositions of fluid in dolomite precipitation experiments.

Experiment ID	Time	T	P	pH[#]	SI	Ca	Mg	Zn	K	Na	Cl	CO$_3^{2-*}$
	days	°C	MPa			ppm	ppm	ppm	ppm	ppm	ppm	ppm
Dolex 26A-HP	10	200	10.4	4.4	1.4	18,000	9,500	1,100	2,800	44,000	96,000	16,000
Dolex 26B-HP	21	200	9.6	4.4	1.4	18,000	9,500	1,200	2,800	44,000	97,000	16,000
Dolex 26C-HP	39	200	9.8	4.4	1.4	18,000	9,500	1,100	2,800	44,000	96,000	16,000
Dolex 28A-HP	10	200	10.3	4.4	1.4	18,000	9,600	120	2,800	44,000	96,000	16,000
Dolex 28B-HP	23	200	9.9	4.4	1.4	18,000	9,600	120	2,800	44,000	96,000	16,000
Dolex 28C-HP	40	200	9.9	4.4	1.4	18,000	9,600	120	2,800	44,000	96,000	16,000
Dolex 29A-HP	10	200	10.0	4.4	1.4	18,000	9,500	18	2,700	44,000	95,000	16,000
Dolex 29B-HP	21	200	10.3	4.4	1.4	18,000	9,500	18	2,700	44,000	95,000	16,000
Dolex 29B-HP	39	200	9.8	4.4	1.4	18,000	9,500	18	2,700	44,000	95,000	16,000
Dolex 30A-HP	9	150	10.1	4.3	1.2	18,000	9,600	1,100	2,800	44,000	96,000	16,000
Dolex 30B-HP	21	150	9.9	4.3	1.2	18,000	9,600	1,100	2,800	44,000	96,000	16,000
Dolex 30C-HP	41	150	9.8	4.3	1.2	18,000	9,600	1,100	2,800	44,000	96,000	16,000
Dolex 31A-HP	10	150	10.3	4.3	1.2	18,000	9,600	120	2,800	44,000	95,000	16,000
Dolex 31B-HP	21	150	10.4	4.3	1.2	18,000	9,600	120	2,800	44,000	95,000	16,000
Dolex 31C-HP	42	150	10.4	4.3	1.2	18,000	9,600	120	2,800	44,000	95,000	16,000
Dolex 32A-HP	10	150	9.8	4.3	1.2	18,000	9,500	14	2,700	44,000	95,000	16,000
Dolex 32B-HP	21	150	10.0	4.3	1.2	18,000	9,500	14	2,700	44,000	95,000	16,000
Dolex 32C-HP	40	150	10.2	4.3	1.2	18,000	9,500	14	2,700	44,000	95,000	16,000

Experiment ID	Time	T	P	pH[#]	SI	Ca	Mg	Zn	K	Na	Cl	CO$_3{}^{2-*}$
	days	°C	MPa			ppm	ppm	ppm	ppm	ppm	ppm	ppm
Dolex 35A-HP	10	125	10.5	4.3	1.1	18,000	9,600	1,200	2,800	44,000	96,000	16,000
Dolex 35B-HP	21	125	9.8	4.3	1.1	18,000	9,600	1,200	2,800	44,000	96,000	16,000
Dolex 35C-HP	41	125	10.3	4.3	1.1	18,000	9,600	1,200	2,800	44,000	95,000	16,000
Dolex 35D-HP	80	125	10.4	4.3	1.1	18,000	9,600	1,200	2,800	44,000	95,000	16,000
Dolex 36A-HP	10	125	10.3	4.3	1.1	18,000	9,600	120	2,800	44,000	95,000	16,000
Dolex 36B-HP	22	125	10.1	4.3	1.1	18,000	9,600	120	2,800	44,000	95,000	16,000
Dolex 36C-HP	42	125	9.9	4.3	1.1	18,000	9,600	120	2,800	44,000	95,000	16,000
Dolex 36C-PSAT	40	125	0.23	4.5^	1.1	18,000	9,800	130	2,800	46,000	96,000	16,000
Dolex 36D-PSAT	81	125	0.23	4.5^	1.1	18,000	9,800	130	2,800	46,000	96,000	16,000

[#]pH values were calculated from the partial pressure of CO_2 unless otherwise indicated

^pH values estimated from the pH of the final fluid, initial pH adjusted by the addition of HCl

The majority of experiments were carried out in a 100 mL Hastelloy C high-pressure reaction vessel at a pressure of about 10 MPa achieved by the introduction of a 9:1 Ar-CO_2 gas mixture to the reaction vessel. Additional experiments were carried out using a 23 mL polytetrafluoroethylene-lined reaction vessel at the saturation pressure (P_{sat}) of the solution in order to determine the effect of pressure on the *D* values. The pH of the solutions in the high pressure experiments (P_{10MPa}) were largely controlled by the partial pressure of CO_2 introduced to the system and were calculated to be 4.3 to 4.4. The pH of the solutions in the P_{sat} experiments were adjusted by the addition of HCl in order to approximate more closely the calculated pH values of the P_{10MPa} experiments. Precipitation experiments were carried out at 125, 150, and 200° C with the goal of determining how *D* varies as a function of temperature. Suites of experiments for a given combination of temperature, pressure, and Zn concentration were conducted for approximately 10, 20, and 40 day intervals in order to determine the proximity of the reaction to equilibrium. Additional 80 day experiments were completed for the 125° C experimental suites due to the slower kinetics of ordered dolomite crystallization at lower temperatures.

Following the experiments, the final fluids were filtered and collected in 50 mL vials for analysis. The final fluids were then set aside to cool. The precipitates were collected and washed with 500 mL of MilliQ de-ionized water to remove any soluble salts that may have precipitated during drying. The collected precipitates were then placed in a weigh boat covered with filter paper in which they were allowed to dry at room temperature for 24 hours before being sealed and stored in glass vials for subsequent characterization and analysis.

Prior to preparation for fluid analysis, droplets of the final fluids collected at the end of each experiment were examined microscopically to determine if any precipitates had formed following cooling. Droplets of 12.1 molar HCl were added to vials with final fluids containing precipitates until all precipitated material re-dissolved. The vials were then sealed and shaken to ensure homogeneous distribution of elements in the fluids. Two mL aliquots of each of the final fluids were prepared for analysis by the addition of 25 mL of MilliQ de-ionized water producing fluids containing less than 2 weight percent NaCl equivalent for analysis that were sealed in 50 mL centrifuge vials.

4.3.3 Analytical methods

4.3.3.1 Powder X-ray Diffraction

The experimental precipitates were characterized using powder X-ray diffraction (PXRD) performed on a Rigaku Miniflex diffractometer at the Department of Geosciences at the University of Missouri-Kansas City (UMKC). The diffractometer was calibrated using a silver standard. The PXRD patterns were collected using Cu $k\alpha_1$($\lambda_{k\alpha1}$ = 1.5406 Å) radiation with a Ni filter in the range of $2\theta = 20°$ to $55°$ with a step size of $0.05°$ and a counting time of 3 seconds per step. The diffraction patterns were processed using the Jade 8+ software (MDI Inc, Livermore, CA).

4.3.3.2 LA-ICP-MS

Polished epoxy grain mounts of the dolomite precipitates were prepared for LA-ICP-MS analysis to determine the trace metal compositions of the precipitates. The LA-ICP-MS analyses were completed at the Trace Element and Radiogenic Isotope lab (TRAIL) at the University of Arkansas using a ESI NWR 193 nm excimer laser coupled with a Thermo Scientific iCapQ quadrupole mass spectrometer. The NIST 610 and NIST

612 glass standards were used for instrument calibration with analyses of the standards

performed at regular intervals throughout each analytical session to correct for instrument

drift. Samples were ablated using a laser output energy of 150 mJ and a 20 μm laser spot

diameter. Helium gas with flow rate of 0.80 L/min was used to transport ablated material

from the ablation cell. Raw LA-ICP-MS data were converted to atomic ratios using the

AMS software (Mutchler et al., 2008) with ^{44}Ca as the internal standard.

4.3.3.3 Fluid analyses

The reactant fluids were analyzed for Ca, Na, Mg, K, Ni, Fe, Co, and Zn using ICP-AES and inductively coupled plasma – mass spectrometry (ICP-MS). The ICP-AES analyses were completed at the Agricultural Experiment Station at the University of Missouri – Columbia following the methods described by Horwitz and Latimer (2005). The ICP-MS analyses were completed at TRAIL using the Thermo Scientific iCapQ.

4.4 Results

Between 1 and 1.5 grams of fine-grained white precipitates were recovered from each of the P_{10MPa} experiments and about 0.25 grams were recovered from each of the P_{sat} experiments. Examination of the
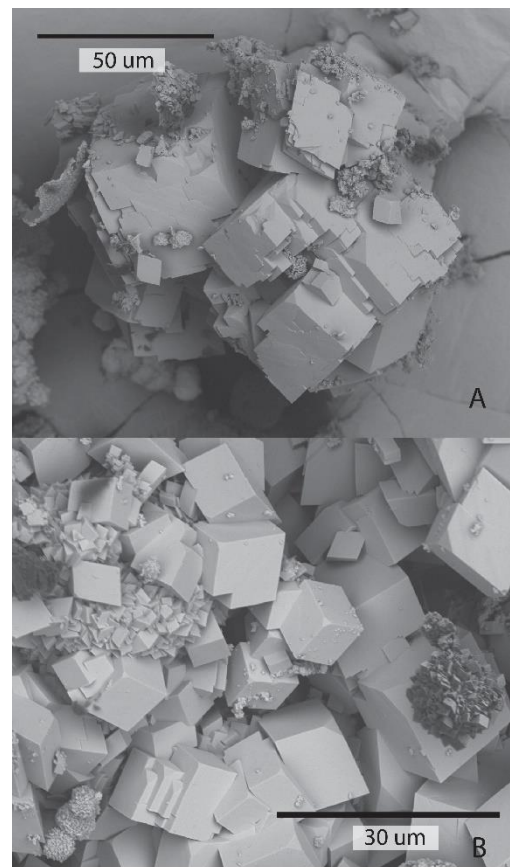
Figure 4-1. Backscattered electron images of experimental precipitates from dolomite precipitation experiments showing the fine grained, crystalline clusters typical of precipitates produced in this study.

precipitates under a microscope showed them to be primarily composed of clusters of intergrown rhombohedral crystals with individual crystals up to about 50 μm in diameter and clusters of up to a few 100 μm (Fig. 4-1). The texture of the precipitates is constant between the experiments. The precipitates from the P_{10MPa} experiments contain minor quantities of a fine-grained flaky metallic material produced by corrosion of the Hastelloy C reaction vessel.

4.4.1 PXRD

Representative PXRD analyses of the dolomite precipitation experiments are shown in Figure 4-2. The PXRD results of the 200° C (Fig. 4-2A,B,C) experiments have well defined dolomite peaks with the high intensity d_{104} reflections centered at $2\theta =$ 30.90° to 30.95°, indicating that the precipitates primarily consist of crystallographic dolomite. The presence of much lower intensity peaks from the m_{104} and m_{113} reflections indicate that a minor amount of magnesite was also produced during these experiments. This magnesite was quantified as between 1 and 6% of the precipitates from the 200° C experiments, with dolomite comprising the remainder.

The PXRD results from the 10 day experiments at 150° C (Fig. 4-2E) exhibit peak broadening. This broadening is shown in the d_{104} reflection in Figure 4-2E which has a full width – half max of 0.41° vs. the full width-half max of 0.28° for the d_{104} reflection in Figure 4-2A. The peak broadening in 10 day, 150° C experiments is also observable in decreased differentiation between the d_{018} and d_{116} reflections at approximately $2\theta = 50.4°$ and $2\theta = 51°$. Peak broadening in dolomite XRD can occur due to disordering of the dolomite, Ca concentrations in excess of strict stoichiometry, or a combination of the two, both of which increase Ca concentrations in the M_1 site and cause expansion of cell
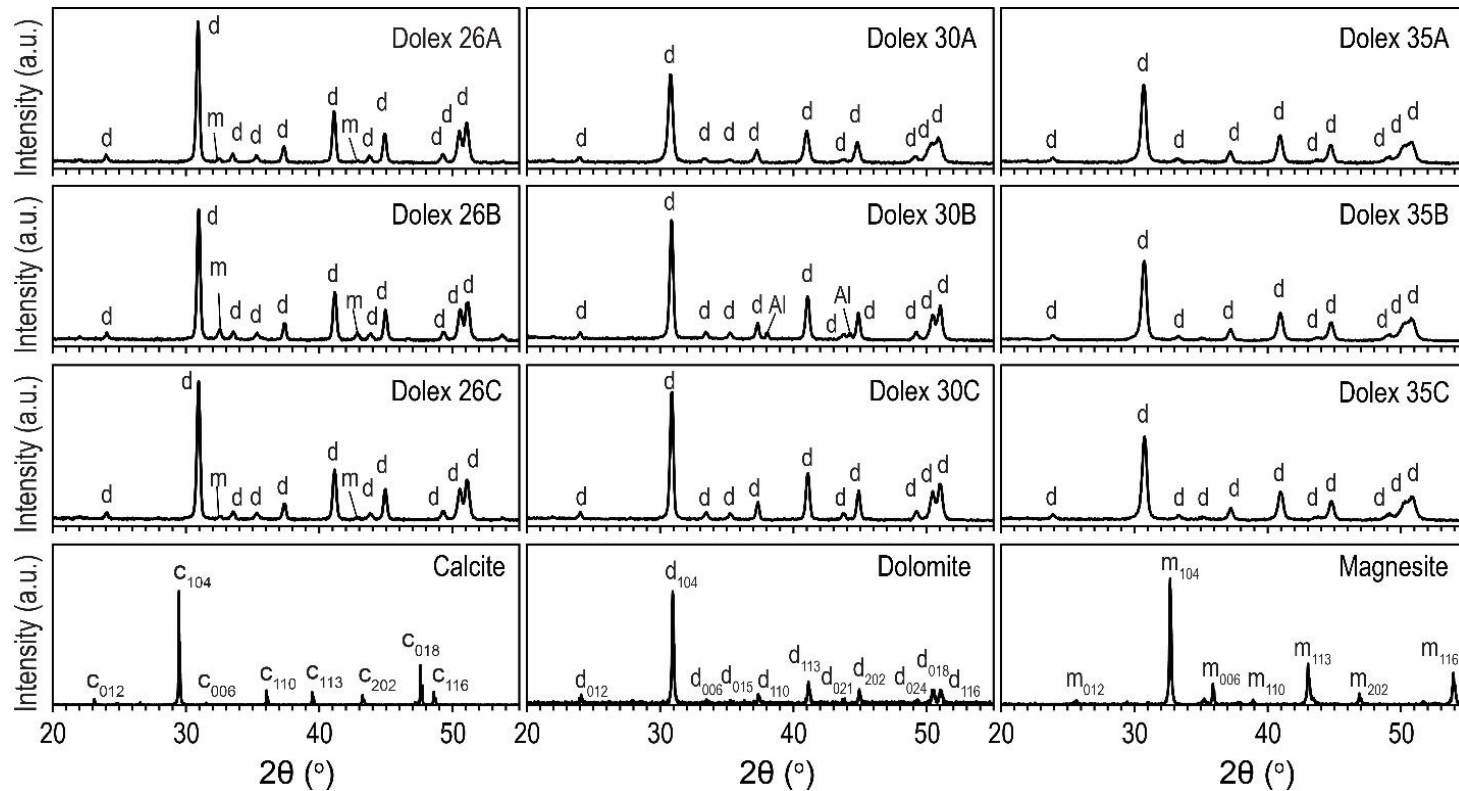
Figure 4-2. Representative PXRD spectra of precipitates from 10 (A), 20 (B), and 40 (C) day, 200° C experiments, 10 (E), 20 (F), and 40 (G) day 150° C experiments, and 10 (I), 20 (J), and 40 (K) day 125 °C experiments. (D), (H), and (J) are XRD spectra of calcite (ID: R040070.1), dolomite, (ID: R050370.1), and magnesite (R040070.1) respectively included for reference from the RRUFF online database (https://rruff.info/; Lafuente et al.,2015). The mineral reflections are labeled with c (calcite), d (dolomite), and m magnesite in both the reference XRD and in the PXRD of the experimental precipitates. Experiment Dolex 30B also has minor aluminum peaks, labeled Al, from the aluminum platform used during the analysis. The intensity is displayed as arbitrary units.

dimensions (Reeder, 2018). Therefore the peak broadening suggests that, on average, the

dolomite precipitates from the 10 day, 150° C experiments are less well ordered and

possibly more Ca-rich than dolomite precipitates from the 200° C experiments. The d_{104}

reflections are also shifted to a lower 2θ (30.78° to 30.82°), another indicator of the

presence of excess Ca in the dolomite matrix (Reeder, 2018). The PXRD results from the

20 and 40 day, 150° C experiments (Fig.4- 2F,G) both exhibit well defined dolomite

peaks with narrow d_{104} reflections, indicating that the precipitates are more well-ordered

crystallographic dolomite, however the d_{104} reflections are shifted to lower 2θ (30.87° to

30.89°), indicating that the dolomite precipitates are slightly Ca enriched.

As for the 10 day, 150° C experiment, the PXRD spectra for precipitates from the

125° C, 10, 20, and 40 day P_{10MPa} experiments (Fig. 4-2I,J,K) all exhibit peak broadening

and peak shift toward lower 2θ (d_{104} reflections centered at 30.70° to 30.75°). This

broadening declines as a function of time as shown by the increase in differentiation

between the d_{018} and d_{116} reflections after 40 days and a narrowing of the d_{104} reflection

with a decline in full width-half maximum of 0.45° after 10 days (Fig. 4-2I) to 0.42° after

40 days (Fig. 4-2K). As for the 10 day, 150° C experiments, the PXRD spectra suggest

that the dolomite precipitates from the 125° C experiments are less well ordered and that

the P_{10MPa} precipitates are more Ca-rich on average than those from the higher

temperature experiments. However, dolomite appears to become more ordered and

stoichiometric with increasing experimental time.

4.4.2 LA-ICP-MS

The dolomite precipitates were analyzed for elements known to be present in the

initial experimental fluids, Na, Mg, K, Ca, and Zn and components of the Hastelloy C

Table 4-2. Summary of LA-ICP-MS analyses of dolomite precipitates.

Experiment ID		Na ppm	Mg ppm	K ppm	Ca ppm	Ti ppm	V ppm	Cr ppm	Fe ppm	Co ppm	Ni ppm	Zn ppm	Ca/Mg atomic
Dolex 26A-HP	average	120	126,000	22	223,000	3.0	2.1	70	400	6	1,100	180	0.94
n = 7	st. dev.	20	5,000		7,000		0.8	30	200	2	500	40	0.06
				(n=1)		(n=1)	(n=2)						
Dolex 26B-HP	average	150	131,000	24	216,000	-	-	50	280	3.2	1,500	150	1.00
n = 11	st. dev.	60	3,000		5,000	-	-	20	80	0.7	300	50	0.05
				(n=1)									
Dolex 26C-HP	average	150	130,000	-	219,000	-	1.3	37	300	5.2	1,000	140	0.98
n = 9	st. dev.	30	3,000	-	4,000	-		8	60	0.8	200	20	0.04
							(n=1)	(n=8)					
Dolex 28A-HP	average	130	130,000	50	218,000	-	7	30	230	5	2,400	28	0.98
n = 7	st. dev.	40	6,000	17	7,000	-	4	10	60	2	1,600	8	0.07
				(n=2)			(n=2)					(n=2)	
Dolex 28B-HP	average	90	127,000	-	222,000	3.2	2.4	30	310	3.3	1,500	15	0.94
n = 10	st. dev.	40	4,000	-	6,000			10	50	0.5	300	3	0.06
		(n=9)				(n=1)	(n=1)	(n=7)				(n = 8)	
Dolex 28C-HP	average	130	128,000	65	221,000	-	2.8	20	300	3	1,500	14	0.97
n = 9	st. dev.	40	4,000	6	5,000	-	0.5	10	100	1	200	2	0.05
				(n=2)			(n=2)	(n=5)				(n=7)	
Dolex 29A-HP	average	110	130,000	-	220,000	2	1.2	30	410	7	2,400	28	0.99
n = 6	st. dev.	50	3,000	-	10,000		0.7	10	90	1	400	6	0.07
						(n=1)	(n=3)	(n=5)				(n=3)	
Dolex 29B-HP	average	120	124,000	-	217,000	-	2	60	600	10	2,700	-	0.95
n = 5	st. dev.	30	5,000	-	10,000	-	1	40	200	2	400	-	0.08
		(n=4)					(n=3)	(n=3)					
Dolex 29C-HP	average	120	128,000	-	217,000	-	1.3	70	500	8	2,200	5.2	0.98
n = 6	st. dev.	10	7,000	-	5,000	-	0.4	30	100	4	300		0.07
							(n=2)	(n=5)		(n=5)		(n=1)	

Experiment ID		Na ppm	Mg ppm	K ppm	Ca ppm	Ti ppm	V ppm	Cr ppm	Fe ppm	Co ppm	Ni ppm	Zn ppm	Ca/Mg atomic
Dolex 30A-HP	average	150	120,000	30	232,000	8.6	1.1	30	180	3.2	600	600	0.86
n = 10	st. dev.	50	3,000	20	5,000			20	50	0.9	80	100	0.04
				(n=4)		(n=1)	(n=1)						
Dolex 30B-HP	average	160	124,000	20	228,000	5.0	1.4	30	220	5	500	320	0.90
n = 11	st. dev.	40	3,000	2	4,000	1.7	0.6	10	20	1	90	90	0.04
				(n=3)		(n=4)	(n=2)						
Dolex 30C-HP	average	170	124,000	30	227,000	-	0.8	30	200	6	800	260	0.90
n = 16	st. dev.	60	3,000	10	4,000	-	0.2	20	30	3	200	40	0.03
				(n=4)			(n=5)						
Dolex 31A-HP	average	180	123,000	24	227,000	-	-	26	190	4	1,300	100	0.89
n =7	st. dev.	40	900	4	2,000	-	-	3	40	2	300	10	0.01
				(n=2)				(n=5)					
Dolex 31B-HP	average	210	122,000	40	230,000	-	-	28	180	4	800	34	0.87
n = 10	st. dev.	60	4,000	20	4,000	-	-	10	40	1	300	8	0.04
				(n=4)				(n=8)					
Dolex 31C-HP	average	120	131,000	-	220,000	-	-	27	190	5	1,500	30	0.98
n = 7	st. dev.	30	3,000	-	4,000	-	-		80	1	500	5	0.03
								(n=1)					
Dolex 32A-HP	average	170	118,000	-	237,000	7.1	-	43	200	3.6	530	24	0.82
n = 7	st. dev.	30	2,000	-	4,000		-	16	70	0.8	70	2	0.02
						(n=1)						(n = 2)	
Dolex 32B-HP	average	140	122,000	-	230,000	-	-	42	180	4	600	-	0.88
n = 7	st. dev.	10	4,000	-	6,000	-	-	11	30	1	100	-	0.05
								(n=5)		(n=6)			
Dolex 32C-HP	average	200	124,000	-	226,000	-	0.7	53	230	7	1,300	-	0.91
n = 9	st. dev.	60	7,000	-	10,000	-		18	50	3	600	-	0.09
		(n=8)					(n=1)	(n=5)		(n=8)			
Dolex 35A-HP	average	130	120,000	28	233,000	1.6	0.4	36	270	5.4	500	1,300	0.85
n = 12	st. dev.	70	6,000	3	8,000			14	90	0.9	100	700	0.07
				(n=4)		(n=1)	(n=1)	(n=5)					

Experiment ID		Na ppm	Mg ppm	K ppm	Ca ppm	Ti ppm	V ppm	Cr ppm	Fe ppm	Co ppm	Ni ppm	Zn ppm	Ca/Mg atomic
Dolex 35B-HP	average	190	120,000	21	232,000	8.7	-	26	140	3.1	700	950	0.86
n = 7	st. dev.	50	5,000	3	8,000	0.3	-	11	70	0.5	200	120	0.04
				(n=4)		(n=2)							
Dolex 35C-HP	average	170	124,000	30	228,000	-	0.8	36	220	3.0	330	740	0.90
n = 12	st. dev.	40	4,000	4	6,000	-	0.3	13	60	0.6	40	90	0.05
				(n=3)			(n=7)						
Dolex 35D-HP	average	170	126,000	25	226,000	5.8	-	34	300	6	500	600	0.92
n = 12	st. dev.	40	4,000		6,000	0.5	-	15	100	4	200	100	0.05
				(n=1)		(n=2)		(n=8)		(n=9)			
Dolex 36A-HP	average	140	120,000	-	240,000	-	-	26	170	11	800	150	0.80
n = 7	st. dev.	70	10,000	-	10,000	-	-	11	20	2	200	40	0.10
								(n=5)					
Dolex 36B-HP	average	230	117,000	-	236,000	-	1.0	57	160	10	900	130	0.82
n = 8	st. dev.	60	4,000	-	6,000	-		41	50	1	100	30	0.05
							(n=1)	(n=5)					
Dolex 36C-HP	average	220	125,000	20	226,000	-	-	17	140	8	900	89	0.91
n = 8	st. dev.	40	3,000	7	4,000	-	-	5	50	2	200	9	0.04
				(n=2)				(n=5)		(n=7)			
Dolex 36C-P$_{SAT}$	average	120	132,000	-	216,000	-	-	-	-	-	4	100	1.01
n = 6	st. dev.	20	3,000	-	4,000	-	-	-	-	-	1	20	0.04
											(n=5)		
Dolex 36D-P$_{SAT}$	average	140	132,000	-	217,000	-	-	-	170	-	5	90	1.00
n = 7	st. dev.	30	2,000	-	3,000	-	-	-		-	1	10	0.03
								(n=1)		(n=6)			

* n = total number of analyses

(n =) the number of analyses that yielded measured concentrations of the indicated element above the limit of detection (LOD) if less than the total number of analyses

- Element was not detected

reaction vessel, Ti, V, Cr, Fe, Co, and Ni, using LA-ICP-MS (Table 4-2). The LA-ICP-MS spectra of the dolomite precipitates from a P_{10MPa} experiment (Fig. 4-3A) show Zn, Fe, Ni, and Co peaks that covary with the Ca and Mg peaks, indicating that these metals are in solid solution in the dolomite matrix. Chromium also appears to be in solid solution in the dolomite matrix in amounts on the order of 10's of ppm, however very strong Cr peaks in the spectra appeared to be associated with either strong Na and Cl peaks or anomalous highs in the other metals, suggesting that they may not represent true solid solution in the dolomite matrix.

Contamination of the dolomite precipitates poses a potential problem for accurate quantification of dolomite solid solution Zn concentrations. Therefore, separate analyses of the epoxy matrix and the metallic corrosion material were performed. Of the elements targeted in the analyses, only Na is present in measurable quantities in the epoxy. Thus, the epoxy matrix is unlikely to be a source of contamination for the measured dolomite Zn concentrations. Analyses of the metallic corrosion material (Fig. 4-3B, box) indicate that the major components, Fe, Co, Cr, and Ni, collectively make up more than 95 wt% of the corrosion material in variable proportions. Vanadium comprises 0.5 to 1 wt% of the corrosion material but did not appear to be present in significant quantities in the dolomite matrix. The corrosion product also contains up to 2.5 wt% Zn, and thus contamination by the material was a concern when evaluating the dolomite precipitate analyses. To avoid this issue, LA-ICP-MS spectra were carefully examined for anomalous spikes in Fe, Co, Cr, and/or Ni, especially those coincident with peaks in the V spectra. Regions of the spectra containing these anomalies were not used for

quantification. Spectral regions with large spikes in Na and K were assumed to arise from soluble salt residue on the surface of dolomite precipitates, and thus were also excluded from quantification.

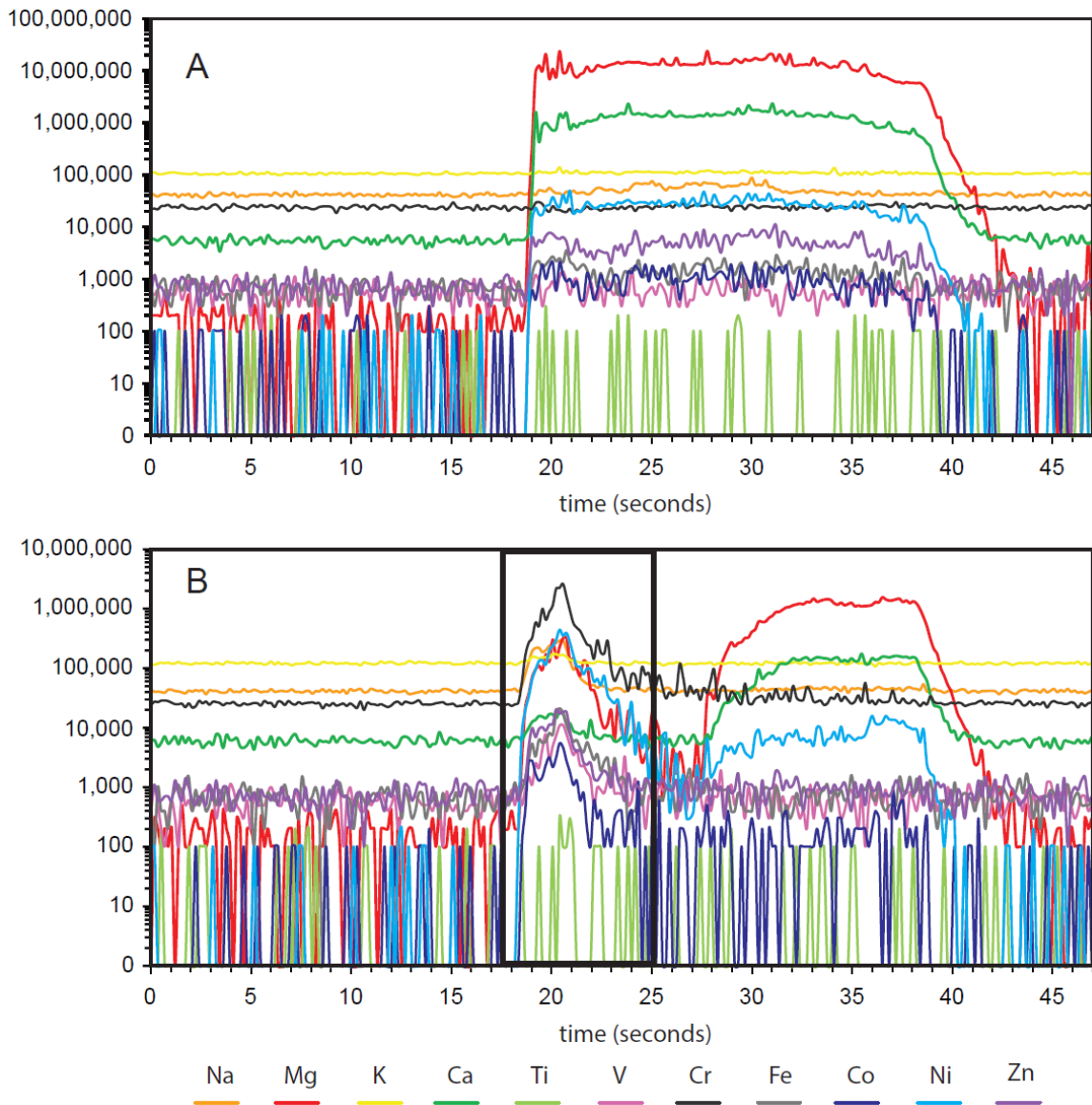**Figure 4-3.** LA-ICP-MS spectra of (A) dolomite precipitate containing measureable Zn and (B) metallic corrosion material (box 17.5 to 25s)

As the purpose of these experiments was to determine D's for the partitioning of Zn between aqueous solution and dolomite, it is important that the concentrations of Zn and Mg used for the calculations be derived from true dolomite precipitates. The PXRD

data indicate that a minor amount of magnesite was produced during the 200° C experiments, an observation borne out by atomic Mg/Ca ratios as high as 4.5 in some LA-ICP-MS analyses of precipitates from 200° C experiments, indicating that the precipitates analyzed consist of magnesite or a mixture of magnesite and dolomite. Therefore, atomic Mg/Ca ratios calculated from each analysis were used to filter data and only analyses having atomic Mg/Ca ratios between of 0.72 to 1.1, the range of values reported for natural dolomites (Chang et al., 1996), were included in the final suite of analyses used to calculate D values.

The dolomite precipitates from the 200° C experiments were close to stoichiometric, with atomic Mg/Ca ratios ranging from 0.86 to 1.1 with average values between 0.94 and 1.0. The LA-ICP-MS data from the 150° C experiments indicate that the dolomite precipitates were more Ca-rich with atomic Mg/Ca ratios from 0.78 to 1.1 and average values from 0.82 to 0.97, in agreement with the PXRD data. The dolomite precipitates from the 125° C, P_{10MPa} experiments are more Ca-rich than those from the higher temperature experiments, having average atomic Mg/Ca ratios from 0.82 to 0.91 and a range of 0.73 to 1.1, supporting the PXRD data. The dolomite precipitates from the 125° C P_{sat} experiments are more stoichiometric with atomic Mg/Ca ratios from 0.92 to 1.1 and average values of 1.0.

Most of the precipitates from the 1000 ppm (Dolex 26, 30, 35) and 100 ppm (Dolex 28, 31, 36) Zn experiments contained measurable Zn concentrations. The average Zn concentrations measured in the dolomite precipitates are highest in the 10 day experiments for any given temperature, declining with increased experimental time. In the 150 and 200° C experiments, the Zn concentration in the dolomite appears to stabilize

between the 20 and 40 day experiments whereas in the 125° C experiments the average

Zn concentration continue to decline between the 40 and 80 day experiments. The

continued decline in average Zn concentrations in the dolomite precipitates is most

apparent in the Dolex 35 suite, which decline by about 20% between each time step. The

Zn concentrations measured in the dolomite precipitates from experiments with the same

initial Zn concentrations increase with decreasing experimental temperature, for example,

after 40 days dolomite precipitated from the 1000 ppm fluid contain on average 140 ppm

Zn at 200° C, 260 ppm Zn at 150° C, and 740 ppm Zn at 125° C. Most of the precipitates

from the 10 ppm Zn experiments (Dolex 29, 32) had Zn concentrations below the limit of

detection (LOD, ~5 to 20 ppm Zn) and therefore the results from these experiments were

not used to calculate D values.

Most of the dolomite precipitates from P_{10MPa} experiments contained measurable

concentrations of Ni, Fe, Co, and Cr leached from the reaction vessel. Average Ni

concentrations in the precipitates ranged from a few 100 to a few 1000 ppm and appear to

increase with increasing temperature such that precipitates with the highest average Zn

concentrations, greater than 2000 ppm, were produced in the 200° C experiments. Iron

concentrations were on the order of 100's of ppm and were also higher on average in the

200° C experiments. Cobalt concentrations were on the order of 1's of ppm and did not

appear to vary with temperature.

4.3.3 Fluid compositions

Table 4-3 shows the compositions of the fluids collected at the end of each

experiment. The final fluids indicate a decline of about 25% in Ca and Mg

concentrations due to precipitation of dolomite. Zinc concentrations did not decline

Table 4-3. Compositions of the final fluids.

Experiment ID	Ca	Na	Mg	K	Ni	Fe	Co	Zn
	ppm	ppm	ppm	ppm	ppm	ppm	ppm	ppm
Dolex 26A-HP	13,000	44,000	7,100	2,700	67	6	1.4	1,100
Dolex 26B-HP	15,000	44,000	7,100	2,800	49	13	1.2	1,200
Dolex 26C-HP	13,000	44,000	7,000	2,600	40	32	1.5	1,100
Dolex 28A-HP	14,000	44,000	7,000	2,700	83	< 4	1.5	120
Dolex 28B-HP	13,000	44,000	7,100	2,700	97	4	1.7	130
Dolex 28C-HP	13,000	44,000	7,000	2,800	58	27	1.0	120
Dolex 29A-HP	14,000	44,000	7,100	2,700	68	19	0.9	17
Dolex 29B-HP	13,000	44,000	7,100	2,800	74	25	1.2	18
Dolex 29B-HP	13,000	44,000	7,000	2,800	82	29	1.1	17
Dolex 30A-HP	13,000	44,000	7,200	3,000	43	< 4	< 0.2	1,100
Dolex 30B-HP	13,000	44,000	7,200	2,800	12	< 4	< 0.2	1,000
Dolex 30C-HP	12,000	44,000	7,000	2,800	87	< 4	0.40	1,000
Dolex 31A-HP	13,000	44,000	7,400	2,800	52	< 4	< 0.2	110
Dolex 31B-HP	13,000	44,000	6,900	2,700	26	< 4	< 0.2	110
Dolex 31C-HP	13,000	44,000	7,200	2,900	95	< 4	0.28	110
Dolex 32A-HP	13,000	44,000	7,100	2,900	21	< 4	< 0.2	13
Dolex 32B-HP	13,000	44,000	7,400	2,800	40	< 4	< 0.2	14
Dolex 32C-HP	13,000	44,000	7,200	2,700	125	< 4	0.35	13
Dolex 35A-HP	13,000	44,000	8,000	3,000	6	< 4	< 0.2	1,200
Dolex 35B-HP	13,000	44,000	7,900	2,700	15	< 4	< 0.2	1,200
Dolex 35C-HP	13,000	44,000	7,900	2,900	14	< 4	< 0.2	1,200
Dolex 35D-HP[*]	13,000	44,000	7,900	2,800	13	3.6	0. 35	1,200
Dolex 36A-HP[*]	13,000	44,000	8,000	2,900	21	2.0	0.48	110
Dolex 36B-HP[*]	13,000	44,000	7,900	2,800	19	1.8	0.45	110
Dolex 36C-HP[*]	13,000	44,000	7,900	2,800	22	1.7	0. 37	110
Dolex 36C-P_{SAT}[*]	13,000	44,000	8,000	2,800	< 0.02	0.09	< 0. 02	130
Dolex 36D-P_{SAT}[*]	12,000	44,000	8,000	2,800	< 0.02	0.12	< 0. 02	130

*Fluid composition obtained from ICP-MS analysis

significantly between the initial and final fluids. All fluids from P_{10MPa} contained

measurable concentrations of Ni, on the order of 10's of ppm, leached from the reaction

vessel. The final fluids from the 200° C experiments also contained measurable

concentrations of leached Fe (1's to 10's of ppm, with the exception of experiment 28A)

and Co (tenths to 10's of ppm).

4.3.4 Calculated D values

Table 4-4. Experimental distribution coefficient (*D*) values for the partitioning of Zn
between dolomite and aqueous solution.

200 °C			150 °C			125 °C		
Experiment ID		*D*	**Experiment ID**		*D*	**Experiment ID**		*D*
Dolex 26A-HP	average	99	Dolex 30A-HP	average	10	Dolex 35A-HP	average	11 / 5
	st. dev.	20		st. dev.	20		st. dev.	62
Dolex 26B-HP	average	75	Dolex 30B-HP	average	54	Dolex 35B-HP	average	82
	st. dev.	21		st. dev.	15		st. dev.	11
Dolex 26C-HP	average	75	Dolex 30C-HP	average	43	Dolex 35C-HP	average	61
	st. dev.	9		st. dev.	7		st. dev.	9
Dolex 28A-HP	average	15 / 0	Dolex 31A-HP	average	16 / 6	Dolex 35D-HP	average	47
	st. dev.	39		st. dev.	20		st. dev.	8
Dolex 28B-HP	average	85	Dolex 31B-HP	average	56	Dolex 36A-HP	average	12 / 9
	st. dev.	11		st. dev.	12		st. dev.	37
Dolex 28C-HP	average	79	Dolex 31C-HP	average	47	Dolex 36B-HP	average	10 / 9
	st. dev.	12		st. dev.	7		st. dev.	25
						Dolex 36C-HP	average	72
							st. dev.	7
						Dolex 36C-P_{SAT}	average	68
							st. dev.	13
						Dolex 36D-P_{SAT}	average	54
							st. dev.	6

The D values calculated using equation (4-5) from the Zn and Mg concentrations measured using LA-ICP-MS and the aqueous concentrations of Mg^{2+} and Zn^{2+} derived from speciation of the final fluid Zn and Mg concentrations are summarized in Table 4-4.

Figure 4-4 shows the D values calculated from the 200° C experiments. The median D (D_{med}) determined from the 10 day, 1000 ppm Zn experiment is 100 and the average D (D_{av}) was 99. The D_{med} of 161 and D_{av} of 150 determined from the 10 day,100 ppm experiment are significantly higher. The D values determined from the 20 day experiments are lower than those from the 10 day experiments, D_{med} = 80 and D_{av} = 75 for the 1000 ppm Zn experiment and D_{med} = 84 and D_{av} = 85 for the 100 ppm Zn experiment. The 40 day D_{med} of 78 and D_{av} of 75 for the 1000 ppm
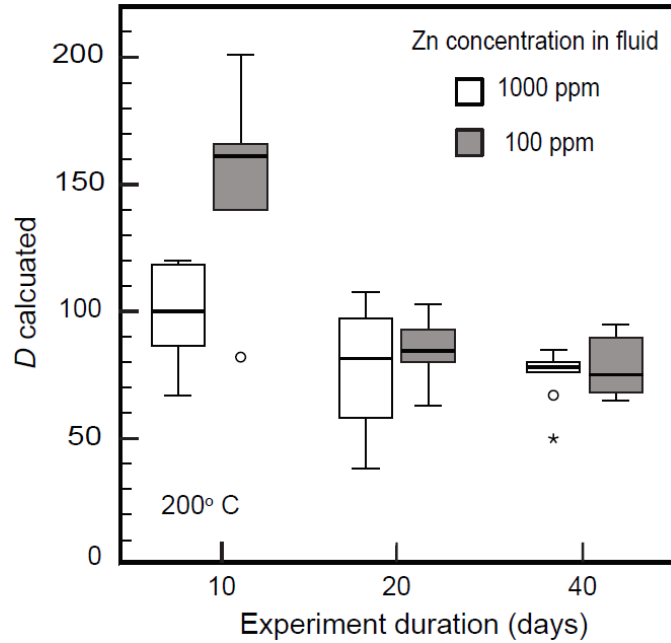

Figure 4-4. Box plot of 200° C experimental distribution coefficients (D's) from this study calculated from 10, 20, and 40 day experimental data. In this and succeeding box plots, the upper and lower portions of the boxes are defined by 75th and 25th percentile of D's (interquartile range). The bold horizontal line within each box represents the median D. The horizontal lines terminating each whisker represent the highest and lowest values that lie within a factor of 1.5 beyond the interquartile range. Outliers that exceed the interquartile range by a factor greater than 1.5 of are indicated by circles (a factor of 1.5 to 3 in excess) or stars (a factor of more than 3).

Zn experiment are consistent with the 20 day D values. The D values determined for the

40 day, 100 ppm experiment, D_{med} of 75 and D_{av} of 78, are slightly lower than the 20 day, 100 ppm D's and are consistent with the 40 day D values from the 1000 ppm experiment.

As in the 200° C experiments, the D values determined from the 150° C (Fig. 4-5) start high with a large gap between the 10 day, 100 ppm D's ($D_{med.} = 175$, $D_{av} = 166$) and the 1000 ppm D's ($D_{med.} = 106$, $D_{av} = 101$ for 1000 ppm Zn). The 20 day D values are significantly lower than the 10 day D values and the gap between 100 ppm Zn D values
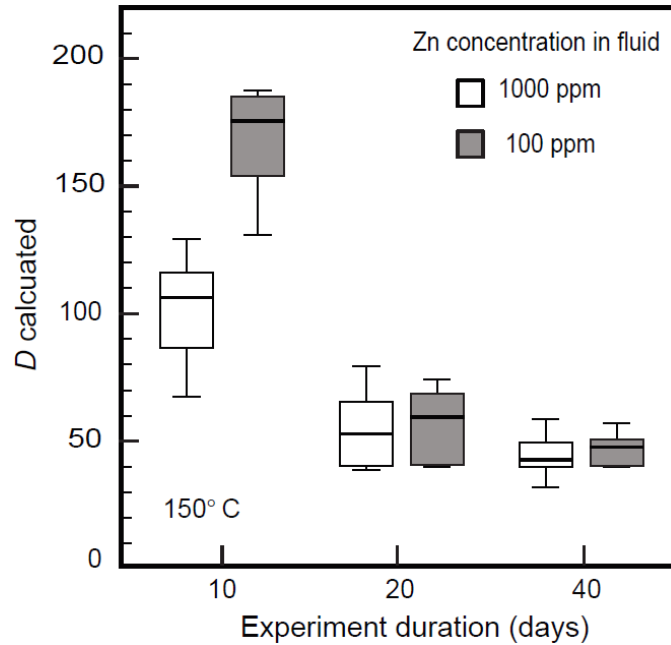

Figure 4-5. Box plot of 150 °C D values from this study for 10, 20, and 40 day experiments.

($D_{med.} = 59$, $D_{av} = 56$ Zn) and 1000 pm D values ($D_{med.} = 53$, $D_{av} = 54$) is negligable. A small decline in D occurs between the 20 day and 40 day experiments ($D_{med.} = 41$, $D_{av} = 43$ for 1000 ppm Zn; $D_{med.} = 48$, $D_{av} = 47$ for 100 ppm Zn). The average D for the 150° C experiments after 20 and 40 days is 30-40% lower than predicted from the 200° C experiments.

Figure 4-6 shows the D results from the 125° C experiments. The 125° C D values decline time, similar to the 150° C and 200° C D values. The 1000 ppm Zn experiments gave D_{av} values of 109, 82, 61, 48, and D_{med} values of 69, 83, 60, and 49 for 10, 20, 40, and 80 days, respectively. The 10, 20, 40, and 80 day, 100 ppm Zn experiments gave D_{av} values of 129, 109, 71 (combined 10 MPa and P_{sat}), 55, and D_{med}

values of 116, 109, 72, and 54.

The 125° C, 100 ppm, 40 day
experiments were performed at
both 10 MPa and P_{sat} in order to
determine how sensitive D is to
pressure at 125 °C, the temperature
at which P_{sat} is furthest from 10
MPa. The range in D from the
P_{10MPa} experiment fall entirely
within the range of values from the
P_{sat} experiment and D_{av} values from
the two experiments are within 5%
of each other, less than the standard
deviations for the experimental D
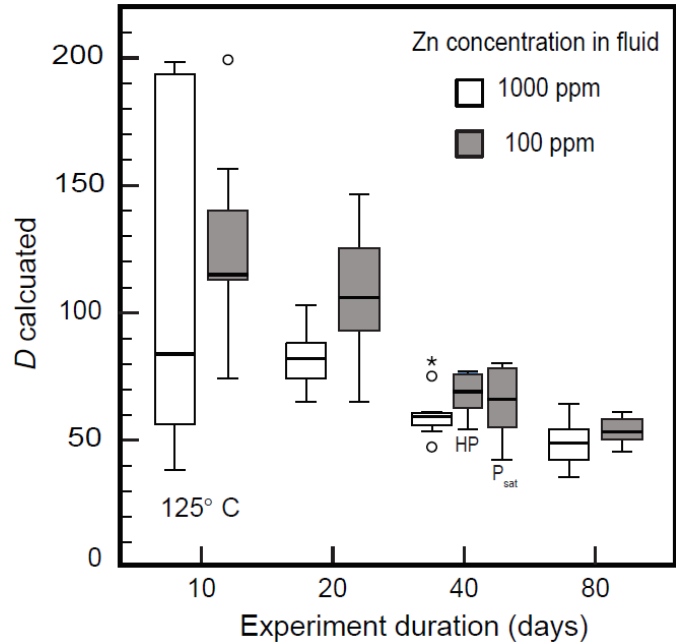values. Thus, the D does not exhibit a significant pressure dependence.

Figure 4-6. Box plot of 125° C *D* values from this study for 10, 20, 40, and 80 day experiments. *D* values from the 40 day, 100 ppm experiments performed at 10 MPa and the saturation pressure of water vapor are indicated by HP and P_{sat} beneath the respective boxes.

4.4 Discussion

4.4.1 Proximity of experiments to equilibrium

One on the key considerations concerning the accuracy of the D values
determined in the study is the proximity of the reactions to equilibrium. In order to
assess this, the results from otherwise identical experiments with the exception of
different experimental durations and Zn concentrations are compared. Ideally, the D
from experiments performed at the same temperature will be constant over multiple time
intervals and Zn concentrations. The 10 day, 200° C D values are significantly higher

than those from the longer experiments and do not agree well with the 100 ppm and 1000 ppm experiments. This indicates that the 10 day, 200° C experiments did not reach equilibrium. The D values from the 200° C, 1000 ppm Zn experiments are consistent between 20 and 40 days with a decrease in variation in D with increasing time. The slight elevation of the 200° C, 100 ppm Zn D_{av} values are likely due to the proximity of the Zn concentrations in the dolomite precipitates to the LOD's. Analyses with Zn concentrations below the limit of detection were not included in the calculation of D. Therefore, the true 100 ppm Zn D_{av} values are likely closer to the 1000 ppm Zn D_{av} values. In addition, the ranges of 100 ppm Zn D values from the 20 and 40 day experiments overlap those from the 1000 ppm Zn ranges. Therefore, the 200° C D_{av} of 75±10 from Dolex 26C is likely accurate.

As for the 200° C experiments, the D values from the 10 day, 150° C experiments at different Zn concentrations are in poor agreement with one another and are significantly higher than those from longer duration experiments and thus do not represent the equilibrium D. The 1000 ppm and 100 ppm D values from the 20 day experiments are in good agreement with one another, as are the 1000 ppm and 100 ppm D values from the 20 day experiments. The D_{av} values decline between the 20 and 40 day experiments. The decline in D is much more rapid between 10 and 20 days (Dolex 30 ~ - 4.7 per day) than between 20 and 40 days (Dolex 30 ~ - 0.49 per day). The evolving rate of decline suggest that the D values are approaching the equilibrium D value exponentially. The ranges of D values from the 40 day experiments fall nearly entirely within the ranges of D values rom the 20 day experiments. This suggests that the 40 day experiments are close to, if not at, equilibrium and that the equilibrium D at 150° C is

close to the values determined from the 40 day experiments. However, an additional experiment with a longer duration is needed to confirm this.

The high variability in D and wide gaps between D_{av} and D_{med} calculated for each of the 10 day, 125° C experiments clearly indicate that these dolomite precipitates formed far from equilibrium. The 20, 40, and 80 day D values follow a pattern similar to those from the 200 and 150° C experiments where D declines with increasing experimental time and a significant gap exists between the D values from the 100 ppm Zn experiments and the D values from the equivalent 1000 ppm Zn experiments at short time intervals that closes as experimental time increases and the experiments approach equilibrium. The gap between the D values for the 100 ppm Zn and 1000 ppm Zn experiments at a given time also decreases with increased experimental time, though a small gap remains after 80 days of experimental time. These observations suggest that the 125° C, 80 day dolomite precipitates are further from equilibrium than the 150° C, 40 day dolomite precipitates, and that the equilibrium 125° C D values is lower than determined after 80 days. The trend in the decline of D in the 125° C experiments also suggests that the equilibrium 125° C D value is lower than that at 150° C.

4.5 Conclusions

The dolomite precipitation experiments in this study were carried out with the goal of determining experimental distribution coefficients for the partitioning of Zn between dolomite and aqueous solution as a function of temperature. The experiments performed at a temperature of 200° C appear to have reached equilibrium between 10 and 20 days as indicated by the reproducibility of D values for experiments performed at two different time intervals and for experiments having experimental fluids with different Zn

concentrations. Thus, it is likely that the predicted equilibrium D value of 75±10 is accurate for the partitioning of Zn between aqueous solution and solid solution in dolomite. The D values calculated for the 20 and 40 day, 150° C experiments did not fully agree and thus it is unclear whether or not these experiments reached equilibrium. However, overlap in D values between the two experimental times, the agreement between the D values from the different aqueous Zn concentration experiments at a given time, and the decline in the rate of change in D suggest that the 150° C experiments are close to reaching equilibrium after 40 days, if it has not actually been reached. An additional, longer experiment will need to be performed to verify if this is the case. The D values from the 125° C experiments have not reached equilibrium after 40 days, and may not have reached it after 80 days. The 125° C exhibit the same pattern of D values decreasing with increasing experimental duration and a slower rate of change in D with increased experimental duration, however the data are insufficient to estimate the proximity to equilibrium for the 80 day, 125° C experiments. The experiments performed at P_{10MPa} and P_{sat}, and 125° C, the temperature at which the two pressures are most divergent, indicate that the D values are not significantly pressure dependent over this pressure range. Although only the 200° C D has been shown to have reached equilibrium, the data thus far clearly show that the equilibrium 150 and 125° C D values are lower than the 200° C D. Further experiments to constrain D at lower temperatures will be significantly hampered by the extremely slow reaction kinetics for dolomite at lower temperatures. However, further experiments at higher temperatures may help further delineate the trend in D as a function of temperature.

4.7 References

Ansdell, K. M., Nesbitt, B. E., and Longstaffe, F. J., 1989. A fluid inclusion and stable-isotope study of the Tom Ba-Pb-Zn deposit, Yukon Territory, Canada. *Economic Geology*, **84**, 841-856.

Appold, M. S., Numelin, T. J., Shepherd, T. J., and Chenery, S. R., 2004. Limits on the metal content of fluid inclusions in gangue minerals from the Viburnum Trend, southeast Missouri, determined by laser ablation ICP-Ms. *Econ. Geol.*, **99**, 185-198.

Appold, M. S., and Wenz, Z. J., 2011. Composition of ore fluid inclusions from the Viburnum Trend, Southeast Missouri district, United States: Implications for transport and precipitation mechanisms. *Econ. Geol.*, **106**, 55-78.

Bethke, C. M., 2004. The Geochemist's Workbench® Release 5: GWB Reference Manual. *University of Illinois, Urbana, IL.*

Boni, M., Mondillo, N., and Balassone, G., 2011. Zincian dolomite: A peculiar dedolomitization case?. *Geol.*, **39**, 183-186.

Bresser, H. A., 1992. *Origin of base metal vein mineralisation in the Lawn Hill mineral field, North-Western Queensland* (Doctoral dissertation, James Cook University of North Queensland).

Chang, L. L. Y., Howie, R. A., and Zussman, J., 1996. Rock-Forming Minerals, Volume 5B, Non-Silicates. *Sulphates, Carbonates, Phosphates and Halides. Second Edition. The Geological Society, London*, 383.

Czamanske, G. K., Roedder, E., and Burns, F. C., 1963. Neutron activation analysis of fluid inclusions for copper, manganese, and zinc. *Science*, **140**, 401-403.

Emsbo, P., Seal, R. R., Breit, G. N., Diehl, S. F., and Shah, A. K., 2016. *Sedimentary exhalative (sedex) zinc-lead-silver deposit model* (No. 2010-5070-N). *US Geol. Surv..*

Garavelli, C.G., Vurro, F., and Fioravanti, G.C., 1982, Minrecordite, a new mineral from Tsumeb: *Mineral. Rec.* **13**, 131–136.

Goldstein A., 1997. The Illinois-Kentucky fluorite district ed. A. Goldstein. *Mineral. Rec.* **28**, 3- 49.

Gardner, H. D., and Hutcheon, I., 1985. Geochemistry, mineralogy, and geology of the Jason Pb-Zn deposits, Macmillan Pass, Yukon, Canada. *Econ. Geol.*, **80**, 1257-1276.

Hagni, R.D. and Grawe, O.R., 1964.Mineral paragenesis in the Tri-State District, Missouri, Kansas, Oklahoma. *Econ. Geol*, **59**, 449-457.

Hammerli, J., Rusk, B., Spandler, C., Emsbo, P., and Oliver, N. H., 2013. In situ quantification of Br and Cl in minerals and fluid inclusions by LA-ICP-MS: A powerful tool to identify fluid sources. *Chem. Geol.*, **337**, 75-87.

Hanor, J. S., 1996. Controls on the solubilization of lead and zinc in basinal brines. *Carbonate-hosted Lead–Zinc Deposits, SEG Special Publication: USA*, **4**, 483-500.

Holland, H. D., The chemical composition of vein minerals, and the nature of ore-forming fluids. Economic Geology, 1956, v. 51, p. 781-797.

Horwitz, W., and Latimer, G. W., 2005. Official methods of analysis of AOAC 18. *AOAC International, Gaithersburg, Md*.

Jolly, J.L. and Heyl, A.V., Mineral paragenesis and zoning in the central Kentucky mineral district. Economic Geology, 1964, v. 59, p.596-624.

Kesler, S. E., Martini, A. M., Appold, M. S., and Walter, L. M., 1996. Na-Cl-Br systematics of fluid inclusions from Mississippi Valley-type deposits, Appalachian Basin: Constraints on solute origin and migration paths. *Geochim. Cosmochim. Acta*, **60**, 225-233.

Lafuente, B., Downs, R. T., Yang, H., and Stone, N., 2015. 1. The power of databases: The RRUFF project. In *Highlights in mineralogical crystallography* (pp. 1-30). De Gruyter.

Leach, D. L., Marsh, E., Emsbo, P., Rombach, C. S., Kelley, K. D., and Anthony, M., 2004. Nature of hydrothermal fluids at the shale-hosted red dog Zn-Pb-Ag deposits, Brooks Range, Alaska. *Econ. Geol.* **99**, 1449-1480.

Leach, D. L., Bradley, D. C., Huston, D., Pisarevsky, S. A., Taylor, R. D., and Gardoll, S. J., 2010. Sediment-hosted lead-zinc deposits in Earth history. *Econ. Geol.*, **105**, 593-625.

Manning, A. H., and Emsbo, P., 2018. Testing the potential role of brine reflux in the formation of sedimentary exhalative (sedex) ore deposits. *Ore Geol. Rev.*, ***102***, 862-874.

McCormick, J.E., Evans, L.L., Palmer, R.A. and Rasnick, F.D., 1971. Environment of the zinc deposits of the Mascot-Jefferson City District, Tennessee. *Econ. Geol.* **66**, p.757-763.

McIntire, W. L., Trace element partition coefficients—a review of theory and applications to geology. *Geochim. Cosmochim. Acta*, 1963, v. 27, p. 1209-1264.

Morse, J. W., and Bender, M. L., 1990. Partition coefficients in calcite: examination of factors influencing the validity of experimental results and their application to natural systems. Chem. Geol. **82**, 265-277.

Mutchler, S.R., Fedele, L. and Bodnar, R.J., 2008. Analysis Management System (AMS) for reduction of laser ablation ICPMS data. In *Laser-Ablation-ICPMS in the Earth sciences: Current practices and outstanding issues* (Vol. 40, pp. 318-327). Mineralogical Association of Canada Quebec

Pelch, M. A., Appold, M. S., Emsbo, P., and Bodnar, R. J., 2015. Constraints from fluid inclusion compositions on the origin of Mississippi Valley-type mineralization in the Illinois-Kentucky district. *Econ. Geol.* **110**, 787-808.

Pinckney, D. M., and Haffty, J., 1970. Content of zinc and copper in some fluid inclusions from the Cave-in-Rock district, southern Illinois. *Econ. Geol.*, **65**, 451-458.

Shannon, R. D., 1976. Revised effective ionic radii and systematic studies of interatomic distances in halides and chalcogenides. *Acta crystallographica section A: crystal physics, diffraction, theoretical and general crystallography*, **32**, 751-767.

Polito, P. A., Kyser, T. K., and Jackson, M. J., 2006. The role of sandstone diagenesis and aquifer evolution in the formation of uranium and zinc-lead deposits, southern McArthur Basin, Northern Territory, Australia. *Econ. Geol.*, **101**, 1189-1209.

Rodriguez-Blanco, J. D., Shaw, S., and Benning, L. G., 2015. A route for the direct crystallization of dolomite. American Mineralogist, **100**, 1172-1181.

Roedder, E., 1984. Interpretation and Utilization of Inclusion Measurements. In: Ribbe P. H. (ed.), *Fluid inclusions*, *Rev. Mineral.*, **12**, 221-250.

Robie, R. A., and RA, R., 1978. Thermodynamic properties of minerals and related substances at 298.15° K and 1 bar (105 pascals) pressure and at higher temperatures.

Rimstidt, J. D., Balog, A., and Webb, J., 1998. Distribution of trace elements between carbonate minerals and aqueous solutions. *Geochim. Cosmochim. Acta* 62, 1851-1863.

Rosenberg, P. E., and Foit Jr, F. F., 1979. The stability of transition metal dolomites in carbonate systems: a discussion. *Geochim. Cosmochim. Acta*, **43**, 951-955.

Smith-Schmitz, S. E., and Appold, M. S., 2018. Prediction of ore fluid metal concentrations from solid solution concentrations in ore-stage calcite: Application to the Illinois-Kentucky and Central Tennessee Mississippi Valley-type districts. *Geochim. Cosmochim. Acta*, **225**, 210-227.

Sverjensky, D. A., 1981. The origin of a Mississippi Valley-type deposit in the Viburnum Trend, southeast Missouri. *Econ. Geol.*, **76**, 1848-1872.

van Hinsberg, V. J., Migdisov, A. A., and Williams-Jones, A. E., 2010. Reading the mineral record of fluid composition form element partitioning. *Geol.,* **38**, 847-850.

Wogelius, R. A., Fraser, D. G., Feltham, D. J., and Whiteman, M. I., 1992. Trace element zoning in dolomite: proton microprobe data and thermodynamic constraints on fluid compositions. *Geochim. Cosmochim. Acta*, **56**, 319-334

. Wenz, Z. J., Appold, M. S., Shelton, K. L., and Tesfaye, S., 2012. Geochemistry of Mississippi Valley–type mineralizing fluids of the Ozark Plateau: A regional synthesis. *Am. J. Sci.* **312**, 22-80.

Wilkinson, J. J., Eyre, S. L., and Boyce, A. J., 2005a. Ore-forming processes in Irish-type carbonate-hosted Zn-Pb deposits: Evidence from mineralogy, chemistry, and isotopic composition of sulfides at the Lisheen mine. *Econ. Geol.*, **100**, 63-86.

Wilkinson, J. J., Weiss, D. J., Mason, T. F. D., and Coles, B. J., 2005b. Zinc isotope variation in hydrothermal systems: preliminary evidence from the Irish Midlands ore field. *Econ. Geol.*, **100**, 583-590.

Wilkinson, J. J., Stoffell, B., Wilkinson, C. C., Jeffries, T. E., and Appold, M. S., 2009. Anomalously metal-rich fluids form hydrothermal ore deposits. *Science*, **323**, 764-767

Yardley, B.W., 2005. 100th Anniversary Special Paper: metal concentrations in crustal fluids and their relationship to ore formation. *Econ. Geol.* **100**, 613-632.

Vite

Sarah Smith was born in Denver, Colorado, the 4th of 8 children, 3 years before Mt. St. Helen's made national news. She soon developed a love for breaking rocks because they were shinier on the inside. When she was 5 her family moved to Wright, Wyoming in the Powder River Basin where she roamed the open ranch lands with her siblings, hunting for fossils and adopting tumble weeds. Field trips to the nearby Black Thunder coal mine with its massive coal seams and equally massive mining equipment were her first introduction to mining. During her years in Wyoming her family took frequent trips to enjoy the geologic wonders of the Black Hills, Devil's Tower, the Bighorns, and the Tetons. For unknown reasons, Yellowstone and the Badlands did not make the cut. Her years in Wyoming developed in Sarah a love of the outdoors and geology that has persisted throughout her life. Her family moved to Moberly, Missouri the year that Yellowstone burned. In high school, Sarah chose to take geology and astronomy instead of physics and has never regretted that choice.

Upon graduating from high school, Sarah attended the University of Missouri where she acquired a degree in anthropology with a minor in geology and children before becoming a stay-at-home parent. After some years at home, Sarah decided to return to school as a chemistry major. She soon found that she loved her coursework, especially inorganic and physical chemistry. She completed her undergraduate research in geology working on the viscosity of pyroxene glasses, thus reigniting her love of the field. After graduating with a B.S. in chemistry, Sarah jettisoned her original plan of going into pharmacy for a graduate degree in geology. Initially uncertain of her path, Sarah began work with Dr. Appold and was introduced to the joys of economic geology, hydrologic modeling, and fluid inclusion analysis. Following completion of her M.S., Sarah chose to stay on for her Ph.D. during which she had the opportunity to hone her analytical chemistry, experimental geochemistry, and numerical modeling skills, and became mildly obsessive about dolomite.